

# 1 **Hydrodynamic and biochemical impacts on the development of** 2 **hypoxia in the Louisiana–Texas shelf Part 1: roles of nutrient** 3 **limitation and plankton community**

4 Yanda Ou<sup>1,2</sup> and Z. George Xue<sup>1,2,3</sup>

5 <sup>1</sup>Department of Oceanography and Coastal Sciences, Louisiana State University, Baton Rouge, LA, 70803, USA.

6 <sup>2</sup>Center for Computation and Technology, Louisiana State University, Baton Rouge, LA, 70803, USA.

7 <sup>3</sup>Coastal Studies Institute, Louisiana State University, Baton Rouge, LA, 70803, USA

8 *Correspondence to:* Z. George Xue ([zxue@lsu.edu](mailto:zxue@lsu.edu))

9 **Abstract.** A three-dimensional coupled hydrodynamic–biogeochemical model with multiple nutrient and plankton functional  
10 groups was developed and adapted to the Gulf of Mexico to investigate the role of nutrients and the complexity of plankton  
11 community in dissolved oxygen (DO) dynamics. A 15-year hindcast was achieved covering the period of 2006–2020.  
12 Extensive model validation against *in situ* data demonstrates that the model was capable of reproducing vertical distributions  
13 of DO, spatial distributions of bottom DO concentration, as well as their interannual variations. The study demonstrates that  
14 bottom DO dynamics and hypoxia evolution are significantly influenced by both physical processes and local biochemistry,  
15 with sedimentary oxygen consumption and vertical diffusion identified as key contributors. Summer hydrodynamics play a  
16 critical role in nutrient distribution and limitation: a notable expansion of Si limitation was simulated when coastal currents  
17 shifted eastward or northward. This effect, especially pronounced on the western part of the Louisiana-Texas shelf, underscores  
18 the importance of nutrient limitation in shaping DO dynamics. The model identifies a bi-peak primary production pattern in  
19 spring and early summer, aligned with satellite chlorophyll *a* variations, attributed to the complexity of the plankton community  
20 and interactions among different plankton groups. Our findings emphasize the necessity of integrating sophisticated plankton  
21 community dynamics into biogeochemical models to understand primary production variability and its impact on bottom  
22 hypoxia.

## 23 **1 Introduction**

24 The Louisiana–Texas (LaTex) shelf in the northern Gulf of Mexico (nGoM) has one of the most notorious recurring hypoxia  
25 in the world (bottom dissolved oxygen (DO) < 2 mg L<sup>-1</sup>, Rabalais et al., 2002; Rabalais et al., 2007a; Justić and Wang, 2014).  
26 Historical observations show that hypoxia usually emerges in mid-May and persists through mid-September (Rabalais et al.,  
27 1999, 2002). The hypoxic zone can cover as big as 23,000 km<sup>2</sup> and has a volume of up to 140 km<sup>3</sup> (Rabalais and Turner,  
28 2019; Rabalais and Baustian, 2020). Although nitrogen (N) is the ultimate limiting nutrient, phosphorus (P) load reduction  
29 also leads to a significant reduction of the hypoxia area (Fennel and Laurent, 2018). Transient P limitation on the shelf (Laurent

30 et al., 2012; Sylvan et al., 2007) was deemed to be associated with the delayed onset and reduction of the hypoxia area.  
31 Sensitivity experiments of hypoxia area reduction to different nutrient reduction strategies suggested that to meet the hypoxic  
32 area reduction goal ( $< 5,000 \text{ km}^2$  in a 5-year running average) set by the Hypoxia Task Force (2008), a dual nutrient strategy  
33 with a reduction of 48 % of total N and inorganic P would be the most effective way (Fennel and Laurent, 2018).

34

35 Coastal eutrophication in the LaTex shelf leads to a high rate of microbial respiration and depletion of DO (Rabalais et al.,  
36 2007b). Incubation studies in the LaTex shelf suggested that sediment oxygen consumption (SOC) accounted for  $20 \pm 4$  %  
37 (Murrell and Lehrter, 2011) to  $25 \pm 5.3$  % (McCarthy et al., 2013) of below-pycnocline respiration, nearly 7-fold greater than  
38 the corresponding percentage in waters overlying sediments ( $3.7 \pm 0.8$  %, about 20 cm above sediments in McCarthy et al.,  
39 2013). The numerical study by Fennel et al. (2013) calculated the corresponding SOC fraction, which reached 60 % when  
40 applying the water respiration rates of Murrell and Lehrter (2011) and sediment respiration rates of Rowe et al. (2002). Another  
41 numerical study (Yu et al., 2015) also pointed out that on the LaTex shelf, oxygen consumption at the bottom water layer was  
42 more associated with SOC rather than water column respiration. According to in-situ data and statistical analysis, SOC can be  
43 estimated using the bottom temperature and DO concentration (e.g., Hetland and DiMarco, 2008). Nevertheless, many  
44 numerical studies treated SOC only associated with the abundance of organic matter in the sediment (e.g., Justić and Wang,  
45 2014; Fennel et al., 2006; 2011). An instantaneous remineralization parameterization by Fennel et al. (2006, 2011) estimated  
46 SOC as a function of sediment detritus and phytoplankton. Using this scheme, Große et al. (2019) found that the simulated  
47 SOC was supported by Mississippi N supply ( $51 \pm 9$  %), Atchafalaya N supply ( $33 \pm 9$  %), and open-boundary N supply ( $16 \pm 2$   
48 %). However, the instantaneous remineralization parameterization tends to overestimate SOC at the peak of phytoplankton  
49 blooms while underestimate SOC after the blooms. In a realistic environment, there should be a lag between the blooms and  
50 the peak SOC (Fennel et al., 2013). Developments of coupled sediment–water models emphasized the importance of  
51 biogeochemical processes in sediments on the SOC dynamics and evolution of bottom hypoxia in the shelf (Moriarty et al.,  
52 2018; Laurent et al., 2016). However, coupled sediment–water models are computationally more expensive than a simplified  
53 parameterization of SOC. Especially for long-term simulations and time-sensitive forecasts, it is crucial to balance the model's  
54 efficiency with its complexity.

55

56 In addition to SOC and excess nutrient supply from the rivers, water column stratification also plays an important role in  
57 regulating the variability of bottom DO concentration in the LaTex shelf. Strong stratification prohibits DO ventilation and  
58 thus reduces DO supply to the bottom water layer (Hetland and DiMarco, 2008; Bianchi et al., 2010; Fennel et al., 2011, 2013,  
59 2016; Justić and Wang, 2014; Wang and Justić, 2009; Feng et al., 2014; Yu et al., 2015; Laurent et al., 2018). On the shelf,  
60 the Mississippi and the Atchafalaya plume introduce buoyancy, leading to a stable water column and weak DO ventilation  
61 processes (Mattern et al., 2013; Fennel and Testa, 2019). Due to the different distances from major river mouths, the influence  
62 of freshwater-induced buoyancy varies along the shelf. Moreover, the transport and deposition processes of organic matter are  
63 affected by the coastal along-shore current systems, resulting in a SOC gradient across the shelf. For instance, Hetland and

64 DiMarco (2008) pointed out that in the west of Terrebonne Bay, where stratification is usually weak, bottom hypoxia is mainly  
65 controlled by bottom respiration.

66

67 The phytoplankton blooms on the LaTex shelf mainly result from cyanobacteria and diatoms (Wawrik and Paul, 2004;  
68 Schaeffer et al., 2012; Chakraborty et al., 2017). In the Mississippi River plume, diatoms were found as the most diverse algal  
69 class accounting for over 42 % of all unique genotypes observed (Wawrik and Paul, 2004). Cruises data in the nGoM indicated  
70 that diatoms accounted for ~50 to ~65 % (inner-shelf) and ~33 to ~64 % (mid-shelf) of chlorophyll *a* in winter and spring, and  
71 ~30 % to ~46 % (inner-shelf) during summer and fall, respectively (Chakraborty and Lohrenz, 2015). A field survey  
72 documented that the biovolume contribution of diatoms to the total phytoplankton could be as high as 80 % and 70 % during  
73 the upwelling seasons in 2013 and 2014, respectively (Anglès et al., 2019). While a lot of existing studies indicated N and P  
74 were more limited than silicon (Si) on the shelf (e.g., for cruises in 2004 in Quigg et al., 2011; for cruises in 2012 in Zhao and  
75 Quigg, 2014; for cruises in 1984, 1994, 2005, 2010, and 2011 in Turner and Rabalais, 2013), Si limitation has also been reported  
76 in both plume and shelf water. A bioassay study on sampled collected in spring and summer 2004 showed signs of co-limitation  
77 of N, P, and Si at multiple sites (Quigg et al., 2011). Based on cruises studies in the plume of the Mississippi River in 1992  
78 and 1993, strong Si limitation in spring was found due to the increasing N:Si ratio in the Mississippi River water (Nelson and  
79 Dortch, 1996). Cruise measurements in 1987 and 1988 also suggested the likelihood of Si limitation, which sometimes  
80 overwhelmed the N limitation (Dortch and Whitledge, 1992).

81

82 Numerical studies for hypoxia in the LaTex shelf were developed mostly incorporating nutrient flows of N and P only (e.g.,  
83 Fennel et al., 2006, 2011, 2013; Laurent et al., 2012; Laurent and Fennel, 2014; Fennel and Laurent, 2018; Justić et al., 2003;  
84 Justić et al., 2007; Justić and Wang, 2014; Große et al., 2019; Moriarty et al., 2018). In addition, many existing models utilized  
85 an over-simplified lower trophic level model (one phytoplankton + one zooplankton function group or only one phytoplankton  
86 group). The recycling of nutrients in water columns and the associated biogeochemical processes, which may be important to  
87 hypoxia evolution (e.g., in the Chesapeake Bay by Testa and Kemp, 2012), could be over-simplified. Moreover, we noticed  
88 that there was a bi-peak primary production pattern observed by satellite and modeled by Gomez et al. (2018) (see comparisons  
89 of modeled and satellite-derived chlorophyll *a* concentration in that work). Their biogeochemical model incorporated a more  
90 complex community (two phytoplankton + three zooplankton function groups) than other over-simplified models where the  
91 bi-peak pattern was hardly captured (e.g., Fennel et al., 2011). The temporal variation of shelf primary production can further  
92 induce corresponding changes in DO concentration and in the bottom hypoxia. In this study, we aimed to investigate the  
93 possible Si limitation and to assess the impacts of the complexity of the plankton community on DO dynamics and bottom  
94 hypoxia development. We adapted and modified a coupled physical-biogeochemical model covering the entire Gulf of Mexico  
95 (GoM) by introducing the oxygen and P cycles to the North Pacific Ecosystem Model for Understanding Regional  
96 Oceanography (NEMURO, Kishi et al. 2007). The model has two phytoplankton and three zooplankton functional groups for  
97 a more comprehensive representation of the plankton community. We also modified the instantaneous remineralization

98 parameterization by adding a conceptual sedimentary organic pool (represented by a sedimentary particulate organic N pool,  
99 PON<sub>sed</sub>; Fig. 1) to allow the accumulation of organic matter in the sediment. The influence of the community is represented in  
100 the biogeochemical processes in water columns and sediments and will eventually be reflected in the bottom DO variability.

## 101 **2 Methods**

### 102 **2.1 Coupled hydrodynamic–biogeochemical model**

103 We adapted the three-dimensional, free-surface, topography-following community model, the Regional Ocean Model System  
104 (ROMS, version 3.7), on the platform of Coupled Ocean–Atmosphere–Wave–Sediment Transport (COAWST) modeling  
105 system (Warner et al., 2010) to the GoM (Gulf–COAWST). ROMS solves finite difference approximations of Reynolds  
106 Averaged Navier–Stokes equations by applying hydrostatic and Boussinesq approximations with a split explicit time-stepping  
107 algorithm (Haidvogel et al., 2000; Shchepetkin and McWilliams, 2005, 2009). The biogeochemical model applied is primarily  
108 based on the NEMURO developed by Kishi et al. (2007). NEMURO is a concentration-based, lower-trophic-level ecosystem  
109 model developed and parameterized for the North Pacific. The original NEMURO model has 11 concentration-based state  
110 variables, including nitrate (NO<sub>3</sub>), ammonium (NH<sub>4</sub>), small and large phytoplankton biomass (PS and PL), microzooplankton,  
111 mesozooplankton, and predatory zooplankton biomass (ZS, ZL, and ZP), particulate and dissolved organic N (PON and DON),  
112 particulate silica (Opal), and silicic acid (Si(OH)<sub>4</sub>). NEMURO is known for its capability to distinguish ZS, ZL, and ZP and to  
113 provide a detailed analysis of the dynamics of different functional groups. It was widely used in studies of plankton biomass  
114 on regional scales (Fiechter and Moore 2009; Gomez et al., 2018; Shropshire et al., 2020). The embedded Si cycle permits the  
115 inclusion of a diatom group (i.e., PL), one of the dominant phytoplankton groups in the LaTex shelf.

### 116 **2.2 Model modification**

117 In a recent effort, Shropshire et al. (2020) adapted and modified NEMURO to the GoM with five structural changes. (1) The  
118 grazing pathway of ZL on PS was removed since, in the GoM, the PS group is predominated by cyanobacteria and  
119 picoeukaryotes, which are too small for direct feeding by most mesozooplankton (i.e., ZL). (2) Linear function of mortality  
120 was applied for PS, PL, ZS, and ZL, while quadratic mortality was used for ZP, accounting for predation pressure of unmodeled  
121 predators, like planktivorous fish. (3) The ammonium inhibition term in the nitrate limitation function was no longer considered  
122 exponentially but followed the parameterization by Parker (1993). (4) Light limitation on photosynthesis was replaced with  
123 Platt et al.'s (1980) functional form, which was also implemented in the newer version of NEMURO. (5) Constant C: Chl ratio  
124 was replaced with a variable C: Chl model according to the formulation by Li et al. (2010).

125

126 Neither the modified (Shropshire et al., 2020) nor the original (Kishi et al., 2007) NEMURO model considered P and oxygen  
127 cycles. In this study, we introduced a P cycle into NEMURO, including three concentration-based state variables: phosphate  
128 (PO<sub>4</sub>), particulate organic P (POP), and dissolved organic P (DOP). The P limitation on phytoplankton growth was introduced



129 using the Michaelis–Menten formula. In the NEMURO model, N serves as the common “currency” when measuring the  
 130 plankton concentration ( $\text{mmol N m}^{-3}$ ). In the river-dominated LaTex shelf, rivers supply inorganic and organic nutrients. In  
 131 our model, riverine  $\text{PO}_4$  (Fig. C1c), DOP, and POP were prescribed based on water quality measurements at river gages. When  
 132 no measurement was available, the  $\text{PO}_4$ , DOP, and POP were approximated using total nitrate+nitrite ( $\text{NO}_3+\text{NO}_2$ ), dissolved  
 133 organic N (DON), and particulate organic N (PON) measurements, respectively, via the Redfield ratio of P: N=1: 16. We  
 134 neglected the POP settling process but preserved these pools by introducing the stoichiometric ratio between P and N instead.  
 135 In other words, the sinking process of POP is implicitly included by building linkages between PON and POP concentrations,  
 136 as the sinking of PON is considered in the model. Governing equations for P state variables are given according to Eqs. 1–3.  
 137 Please also refer to the appendices for more details on expressions of modified terms (Appendix A), state variables (Appendix  
 138 Table B1), source and sink terms (Appendix Table B2), and values of parameters (Appendix Table B4).

$$\begin{aligned}
 140 \quad \frac{d(\text{PO}_4)}{dt} &= (\text{ResPSn} + \text{ResPLn}) \cdot \text{RPO4N} \\
 141 \quad &+ (\text{DecP2N} + \text{DecD2N}) \cdot \text{RPO4N} \\
 142 \quad &+ (\text{ExcZSn} + \text{ExcZLn} + \text{ExcZPn}) \cdot \text{RPO4N} \\
 139 \quad &- (\text{GppPSn} + \text{GppPLn}) \cdot \text{RPO4N}, \tag{1}
 \end{aligned}$$

$$\begin{aligned}
 144 \quad \frac{d(\text{DOP})}{dt} &= (\text{DecP2D} - \text{DecD2N}) \cdot \text{RPO4N} \\
 143 \quad &+ (\text{ExcPSn} + \text{ExcPLn}) \cdot \text{RPO4N}, \tag{2}
 \end{aligned}$$

$$\begin{aligned}
 145 \quad \frac{d(\text{POP})}{dt} &= (\text{MorPSn} + \text{MorPLn} + \text{MorZSn} + \text{MorZLn} + \text{MorZPn}) \cdot \text{RPO4N} \\
 146 \quad &+ (\text{EgeZSn} + \text{EgeZLn} + \text{EgeZPn}) \cdot \text{RPO4N} \\
 147 \quad &- (\text{DecP2N} + \text{DecP2D}) \cdot \text{RPO4N}, \tag{3}
 \end{aligned}$$

148

149 We further adapted the oxygen cycle developed by Fennel et al. (2006, 2013) to NEMURO for hypoxia simulations. However,  
 150 our model's biogeochemical processes are slightly different due to the different plankton functional groups considered. Sources  
 151 for oxygen are contributed by the photosynthesis of two phytoplankton functional groups. In comparison, the sinks are  
 152 attributed to respirations of two phytoplankton functional groups, metabolism of three zooplankton functional groups, light-  
 153 dependent nitrification (Olson, 1981; Fennel et al., 2006), aerobic decomposition of particulate and dissolved organic matter  
 154 (measured as PON, and DON, respectively), and SOC. Oxygen air–sea flux was estimated following parameterizations by  
 155 Wanninkhof's (1992). The biogeochemical dynamics of oxygen were adopted as follows (Eq. 4; also see detailed descriptions  
 156 of variables and parameters in Appendix A–B):

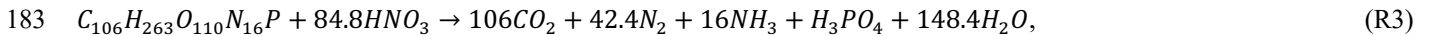
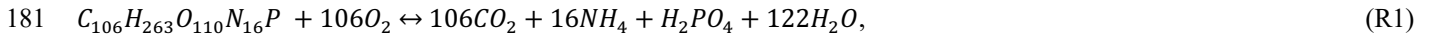
$$\begin{aligned}
 157 \quad \frac{d(\text{Oxyg})}{dt} &= (r\text{OxNO}_3 \cdot \text{GppNPS} + r\text{OxNH}_4 \cdot \text{GppAPS}) \\
 158 \quad &+ (r\text{OxNO}_3 \cdot \text{GppNPL} + r\text{OxNH}_4 \cdot \text{GppAPL}) \\
 159 \quad &- \text{ResPSn} \cdot [\text{RnewS} \cdot r\text{OxNO}_3 + (1 - \text{RnewS}) \cdot r\text{OxNH}_4]
 \end{aligned}$$

$$\begin{aligned}
161 \quad & -ResPLn \cdot [RnewL \cdot rOxNO_3 + (1 - RnewL) \cdot rOxNH_4] \\
162 \quad & -rOxNH_4 \cdot (ExcZSn + ExcZLn + ExcZPn) \\
163 \quad & -2 \cdot Nit \cdot LgtlimN \cdot \hat{r} \\
164 \quad & -rOxNH_4 \cdot (DecD2N + DecP2N) \cdot \hat{r} \\
165 \quad & -SOC \cdot THK_{bot}, \tag{4}
\end{aligned}$$

166 A  $PON_{sed}$  pool due to vertical sinking processes of PON was introduced for parameterization of SOC. The SOC scheme (Fennel  
167 et al., 2006) is known as the instantaneous consumption of DO. As soon as the PON falls into the sediment bed, PON will be  
168 decomposed instantaneously. This scheme tends to overestimate SOC at the peak of blooms and to underestimate SOC after  
169 blooms since the lag in SOC demand is neglected (Fennel et al., 2013). We considered such temporal delays in SOC by  
170 introducing a  $PON_{sed}$  pool. A portion of the PON ends with  $PON_{sed}$ , while the rest is buried ( $PON_{burial}$ ) and removed from the  
171 system. The parameterization is shown in the following. 1) Organic matter settling down at the conceptual sediment layer is  
172 remineralized at a temperature-dependent aerobic remineralization rate,  $K_{P2N}$ . 2) Sediment oxygen is consumed only in the  
173 oxidation of sedimentary organic matter (represented by  $PON_{sed}$ ) and the nitrification of ammonium to nitrate (Fennel et al.,  
174 2006). 3) Oxygen consumption at the conceptual sediment layer directly contributes to oxygen concentration decreases only  
175 at the bottom water column. 4) Sediment denitrification is linearly related to SOC according to observational-based estimates  
176 by Seitzinger and Giblin (1996), but the relationship was modified by Fennel et al. (2006) with a slightly smaller slope of  
177 denitrification on SOC rate, i.e.,

$$178 \quad denitrification \text{ (mmolN m}^{-2} \text{ day}^{-1}) = 0.105 \times SOC \text{ (mmolO}_2 \text{ m}^{-2} \text{ day}^{-1}), \tag{5}$$

179 5) Aerobic decomposition of  $PON_{sed}$ , sediment nitrification, and denitrification follow chemical equations according to  
180 (Fennel et al., 2006):



184 6) Nitrate produced in sediments (Eq. R2) is used for denitrification (Eq. R3). The linear assumption in 4) implicitly builds  
185 relationships among the reactions listed in assumption 5). Let's assume that the production rate of  $NH_4$  by aerobic  
186 decomposition (Eq. R1) of organic matter is  $M \text{ mmol m}^{-3} \text{ day}^{-1}$ , and that the fraction of denitrification-produced  $CO_2$  (Eq. R3)  
187 to the total  $CO_2$  production (Eqs. R1 and R3) is  $x$ . According to the linear assumption abovementioned, the consumption rate  
188 of  $NO_3$  during denitrification (Eq. R3) is proportional to the total consumption rate of  $O_2$  in the sediment (Eqs. R1 and R2),  
189 yielding  $\frac{84.8Mx}{16(1-x)} = 0.105 \times \left[ \frac{106M}{16} + \frac{84.8Mx}{8(1-x)} \right]$  and further  $x \approx 0.1425$ . The oxygen consumption rate (Eq. 6) and organic matter  
190 consumption rate (Eq. 7) due to the coupled aerobic decomposition, nitrification, and denitrification processes can be obtained  
191 by substituting the  $x$  value into the stoichiometric ratios according to Eqs. R1–R3.

$$192 \quad Oxyg_{consumption} = \frac{106M}{16} + \frac{84.8Mx}{8(1-x)} = 8.3865M, \tag{6}$$

193  $OM_{consumption} = \frac{M}{16} + \frac{Mx}{16(1-x)} = 0.0729M,$  (7)

194 Accordingly, the SOC and consumption rate of  $PON_{sed}$  are given, respectively as follows:

195  $SOC = Oxyg_{consumption} \cdot THK_{bot} = 8.3865M \cdot THK_{bot},$  (8)

196  $PON_{sed_{consumption}} = 16 \cdot OM_{consumption} \cdot THK_{bot} = 1.1662M \cdot THK_{bot},$  (9)

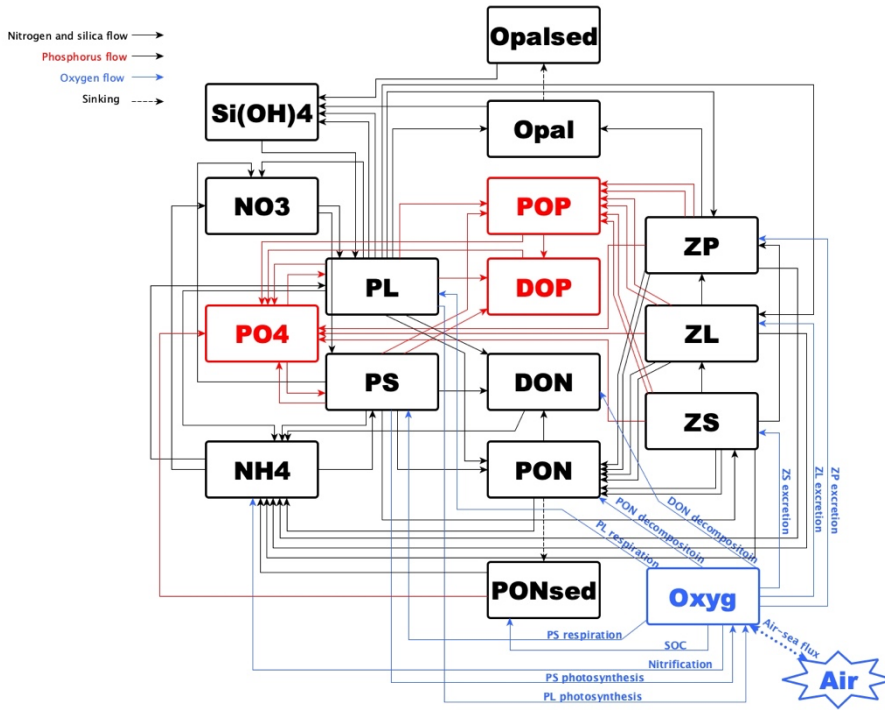
197 where,

198  $M = \frac{PON_{sed} \cdot VP2N_0 \cdot \exp(K_{P2N} \cdot TMP)}{THK_{bot}},$  (10)

199  $THK_{bot} = \text{thickness of bottom water column},$  (11)

200

201 We further added light inhibition to nitrification and aerobic decomposition. These parametrizations were applied following  
 202 descriptions by Fennel et al. (2006, 2013). For the oxygen-dependent term, an oxygen threshold is specified below which no  
 203 aerobic respiration or nitrification occurred. Detailed equations are listed in Appendix A. The structure of the newly modified  
 204 NEMURO model is shown in a schematic diagram in Fig. 1.



205

206 **Figure 1. Schematic diagram of the modified NEMURO model. Note that the P flow and the oxygen flow are two newly added flows**  
 207 **to the original NEMURO model.**

## 208 2.3 Model set-ups

209 The coupled model was applied to the GoM using Arakawa C-grid with a horizontal resolution of ~5 km (Fig. 2a). There are  
210 334 and 357 interior rho points in the east-west and north-south directions, respectively. The model includes 36 sigma layers  
211 vertically. The wetting and drying scheme (Warner et al., 2013) was implemented to provide a more accurate representation  
212 of shallow water. The computational time step (i.e., baroclinic time step) was set to 240 seconds, while the number of barotropic  
213 time steps between each baroclinic time step was set to 30. Model hindcast was carried out from 1 August 2006 to 26 August  
214 2020, with the first five months as a spin-up period. Model historical and averaged results were output at a daily interval, while  
215 the historical fields were output at UTC 00: 00 each day.

216

217 The physical model set-ups largely followed an earlier Gulf-COAWST application (Zang et al., 2018, 2019, 2020). Open  
218 boundaries were set at the south and east forced by daily water level, horizontal components of 3-D current velocity, horizontal  
219 components of depth-integrated current velocity, 3-D water salinity, and 3-D water temperature derived from the Hybrid  
220 Coordinate Ocean Model (HYCOM) global analysis products (Bleck and Boudra, 1981; Bleck, 2002) with data assimilated  
221 via the Navy Coupled Ocean Data Assimilation system (Cummings, 2005; Cummings and Smedstad, 2013; Fox et al., 2002;  
222 Helber et al., 2013). For lateral boundary conditions, we utilized Chapman implicit for free surface and water level (Chapman,  
223 1985), Flather for depth-integrated momentum (Flather, 1976), gradient for mixing total kinetic energy, and mixed radiation-  
224 nudging conditions for 3-D momentum, temperature, and salinity (Marchesiello et al., 2001). The nudging time steps for the  
225 mixed radiation-nudging condition were set to 1 day for inflows and 30 days for outflows. The boundary nudging technique  
226 was performed at the computational grids along the open boundary. The boundary condition types for passive biological and  
227 chemical tracers (i.e., PS, PL, ZS, ZL, ZP, NO<sub>3</sub>, NH<sub>4</sub>, PON, DON, Si(OH)<sub>4</sub>, opal, PO<sub>4</sub>, POP, DOP, and Oxyg) were all  
228 prescribed as radiation.

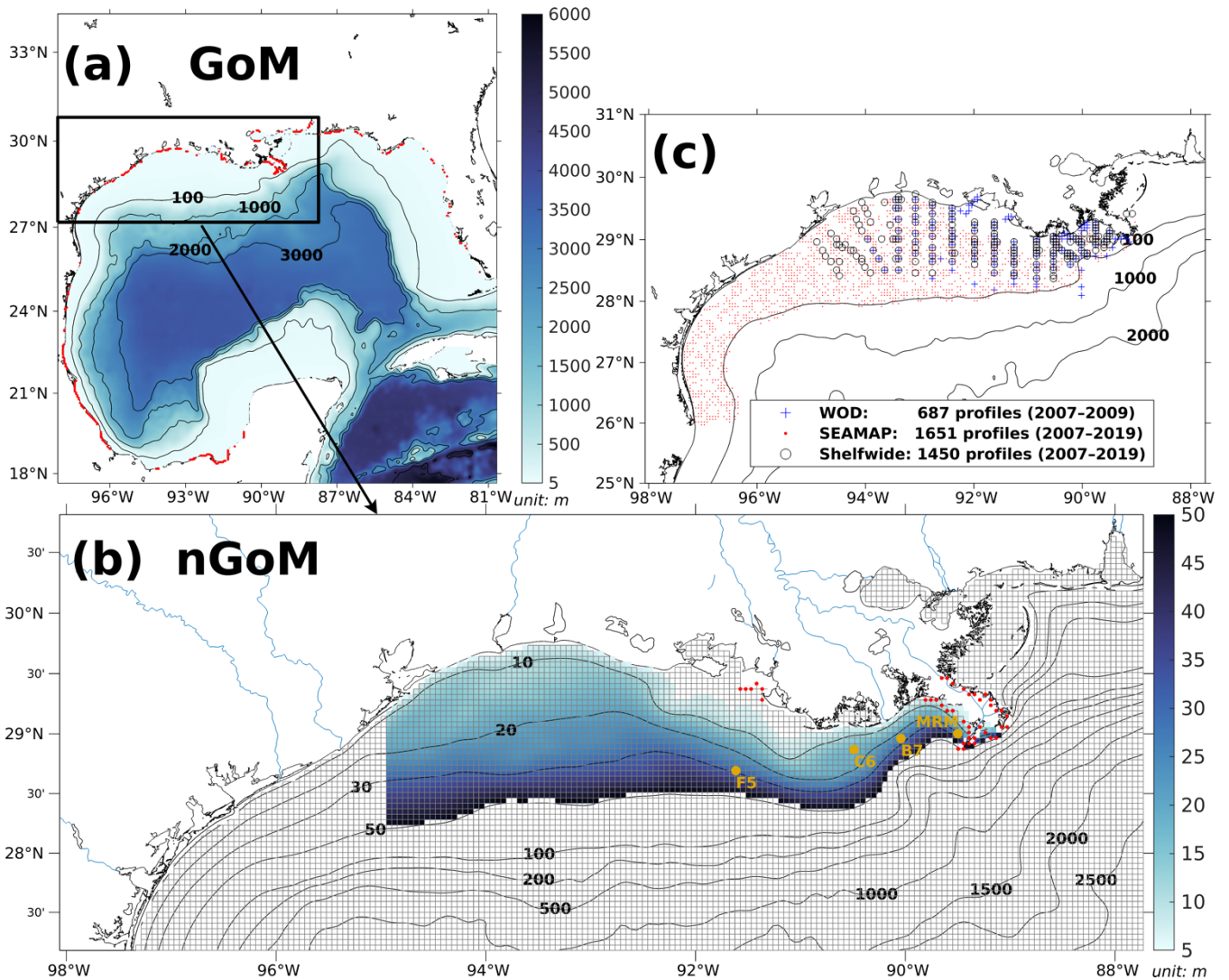
229

230 Initial conditions for water level, horizontal components of 3-D current velocity, horizontal components of depth-integrated  
231 current velocity, 3-D water salinity, and 3-D water temperature were provided by the same HYCOM products as well. Initial  
232 conditions for concentrations of NO<sub>3</sub>, PO<sub>4</sub>, and Si(OH)<sub>4</sub> were interpolated from measurements provided by the World Ocean  
233 Database (WOD, Boyer et al., 2018). Initial conditions for DO concentration were given by World Ocean Atlas (WOA, Garcia  
234 et al., 2018). At the sediment layer, PON<sub>sed</sub>, PON<sub>burial</sub>, opal<sub>sed</sub>, and opal<sub>burial</sub> were initialized as 0.1 mmol m<sup>-3</sup>. Other biological  
235 and chemical tracers were initialized as 0.1 mmol m<sup>-3</sup> due to the lack of observations.

236

237 Atmospheric forcings, including surface wind velocity at 10 m height above sea level, net longwave radiation flux, net  
238 shortwave radiation flux, precipitation rate, air temperature 2 m above sea level, sea surface air pressure, and relative humidity  
239 2 m above sea level, were derived from the National Centers for Environmental Prediction (NCEP) Climate Forecast System  
240 Reanalysis (CFRS) 6-hourly products (for years prior to 2011, Saha et al., 2010) and NCEP CFS Version 2 (CFSv2) 6-hourly

241 products (for years starting from 2011, Saha et al., 2011) with a horizontal resolution of ~35 km and ~22 km, respectively. In  
242 our model, 63 rivers were considered as horizontal point source forcings along the coastal GoM. They were split into 280  
243 points (red dots in Fig. 2a) sources transporting time-varying salinity (nearly zero), temperature, 3-D horizontal momentum  
244 (based on the magnitude of river discharges), nutrients ( $\text{NO}_3$ ,  $\text{NH}_4$ ,  $\text{PO}_4$ ,  $\text{Si}(\text{OH})_4$ , PON, DON, POP, and DOP; Fig. C1), and  
245 DO to the computational domain. Locations of river point sources of the Mississippi and the Atchafalaya Rivers were shown  
246 as red dots in Fig. 2b. For reconstructions of time series of river forcing terms, we composed measurements from various  
247 sources, including U.S. Geological Survey (USGS) National Water Information System (NWIS), National Oceanic and  
248 Atmospheric Administration (NOAA) Tides and Currents System (TCS), NOAA National Estuarine Research Reserve System  
249 (NERRS), and Mexico National Water Commission (CONAGUA, for rivers in Mexico's territory). Daily averaged river  
250 discharges were given based on measurements by USGS NWIS and CONAGUA. The magnitude of river discharges was  
251 multiplied by 1.4 to account for adjacent watershed areas and the lateral inflow of tributaries (Warner et al., 2005). River  
252 temperature and salinity time series were reconstructed from measurements by USGS NWIS, NOAA TCS, and NOAA  
253 NERRS. River nutrient concentrations were provided monthly by USGS NWIS and NOAA NERRS and were extended to  
254 daily time series with values in the corresponding months. Riverine DO concentration was set to be a constant ( $258 \text{ mmol m}^{-3}$ ),  
255 assuming that riverine DO was saturated at 25 °C under 1 atm. Besides, tidal forcings were introduced in the hydrodynamic  
256 model, taking into account the influences of tidal elevations and tidal currents. There were 13 tidal constituents considered in  
257 the model including M2, S2, N2, K2, K1, O1, P1, Q1, MF, MM, M4, MS4, and MN4.  
258



259  
 260 **Figure 2. (a) Bathymetry of the entire domain of the Gulf–COAWST, (b) zoom-in bathymetry plot of the northern Gulf of Mexico**  
 261 **(nGoM), and (c) locations of observed inorganic nutrient and DO profiles derived from WOD, SEAMAP, and NOAA’s shelf-wide**  
 262 **cruises. In (a), locations of river point sources are denoted by red dots. In (b), only bathymetry between 6 and 50 m is mapped with**  
 263 **colors; computational meshes are split by solid grey lines; main river channels are denoted by solid blue curves; locations of river**  
 264 **point sources of the Mississippi and the Atchafalaya Rivers are indicated by red dots; sampling locations for SOC and overlaying**  
 265 **water respiration measurements by McCarthy et al. (2013) are denoted by dark yellow dots.**

### 266 3 Biogeochemical model validations

#### 267 3.1 Available measurements

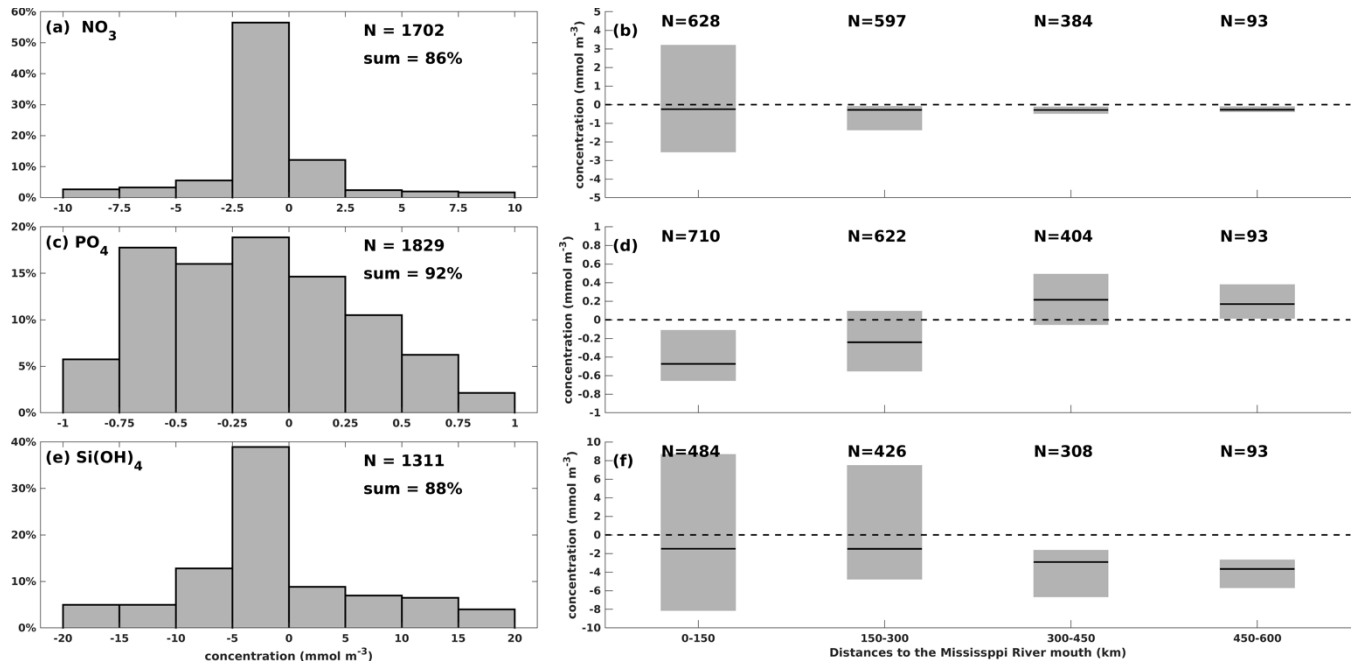
268 In this section, biogeochemical model validations were conducted for surface inorganic nutrient concentration (i.e.,  $\text{NO}_3$ ,  $\text{PO}_4$ ,  
 269 and  $\text{Si(OH)}_4$ ), types of limited nutrients, ratios of diatom/total phytoplankton, SOC, DO concentration profiles, spatial

270 distributions of bottom DO concentration and temporal variability of the hypoxic area against multiple field and lab data sets.  
271 Validation of the hydrodynamic model can be found in Zang et al. (2019).  
272  
273 Inorganic nutrient concentrations from WOD and NOAA's shelf-wide cruises were used for model validation. WOD  
274 measurements cover the period from 11 January 2007 to 5 July 2009, while the shelf-wide records cover the 2007-2019 period.  
275 The types of limited nutrients across the LaTex shelf were discussed based on multiple bioassay studies (Turner and Rabalais,  
276 2013; Quigg et al., 2011; Smith and Hitchcock, 1994; Sylvan et al., 2006, 2007; Zhao and Quigg, 2014; Nelson and Dortch,  
277 1996). The diatom percentage of total phytoplankton was derived from measurements by Chakraborty and Lohrenz (2015) and  
278 Schaeffer et al. (2012). The SOC measurements were provided by an incubation study (McCarthy et al., 2013). Available DO  
279 concentration profiles were obtained from the NOAA-supported mid-summer shelf-wide cruises and Summer Groundfish  
280 Survey in GoM supported by the Southeast Area Monitoring and Assessment Program (SEAMAP) conducted annually by the  
281 Gulf States Marine Fisheries Commission. The shelf-wide cruises provided 1450 measured profiles with 70401 available  
282 records from 2007 to 2019. There were at least 83 DO profiles for each summer (June–August, except 2016) from the shelf-  
283 wide cruise observations. The selected SEAMAP DO dataset covers a time range from 2007 to 2019 with measurements  
284 including 1651 profiles with 94200 sampled records. Locations of the selected profiles from different archives were shown in  
285 Fig. 2c. Summer measurements by the shelf-wide cruises were used to validate spatial patterns of bottom DO concentration  
286 and time series of summer hypoxic areas. Estimated hypoxic areas by the cruises are available from 2007 to 2020, with a range  
287 from 5,480 km<sup>2</sup> to 22,720 km<sup>2</sup>.

### 288 **3.2 Surface nutrient concentration**

289 One-to-one comparisons for surface nutrient concentration validation were seldom carried out in previous numerical studies,  
290 where spatial-averaged or temporal-averaged matrices were frequently validated. To provide a more detailed quantification of  
291 model performance in surface nutrients, we performed one-to-one differences between simulations and measurements at each  
292 sampling location on specific dates. Modeled results showed good agreements with the cruise measurements from both shelf-  
293 wide and WOD records (Fig. 3) in terms of magnitudes. There are 86% of surface NO<sub>3</sub> differences dropping within a range of  
294  $\pm 10$  mmol m<sup>-3</sup> with the most biases ranging from -2.5 to 0 mmol m<sup>-3</sup> (56%, Fig. 3a). It indicates a slight underestimation,  
295 which is mostly found in the mid and western shelf (>150 km from the Mississippi River mouth, Fig. 3b). Surface NO<sub>3</sub> biases  
296 exhibit a higher variance near the mouth than in other regions. There are 92% of surface PO<sub>4</sub> bias pairs dropping within  $\pm 1$   
297 mmol m<sup>-3</sup> (Fig. 3c), exhibiting a more even distribution pattern than the NO<sub>3</sub> differences. It results from the model  
298 underestimation in the mid and east shelf but overestimation in the west (Fig. 3d). There are 88% of surface Si(OH)<sub>4</sub> differences  
299 within a range of  $\pm 20$  mmol m<sup>-3</sup> with a slight underestimation (Fig. 3e). We found higher biases near the Mississippi (first to  
300 third quartiles within  $\pm 8$  mmol m<sup>-3</sup> at 0-150 km) and the Atchafalaya (-5 to 7 mmol m<sup>-3</sup> at 150-300 km) Rivers mouths (Fig.  
301 3f) than at the western shelf. Mean Mississippi and Atchafalaya riverine PO<sub>4</sub> concentrations were  $2.7 \pm 0.7$  mmol m<sup>-3</sup> and  $2.3$   
302  $\pm 0.7$  mmol m<sup>-3</sup>, respectively, and mean riverine Si(OH)<sub>4</sub> concentrations were  $118 \pm 23$  mmol m<sup>-3</sup> and  $116 \pm 21$  mmol m<sup>-3</sup>,

303 respectively. Thus, the nutrient concentration bias between simulations and observations is acceptable, considering the possible  
 304 transient influence from the riverine nutrient loads during a survey.



305

306 **Figure 3. Comparison of surface nutrient concentration between model hindcasts and cruise measurements (both shelf-wide and**  
 307 **WOD) for (a)–(b)  $\text{NO}_3$ , (c)–(d)  $\text{PO}_4$ , and (e)–(f)  $\text{Si(OH)}_4$ . The left bar graphs illustrate the distribution of concentration differences**  
 308 **by percentage within specific concentration ranges, while the right box charts show the first quartiles, third quartiles, and medians**  
 309 **of the concentration differences against the distance to the Mississippi River mouth.**

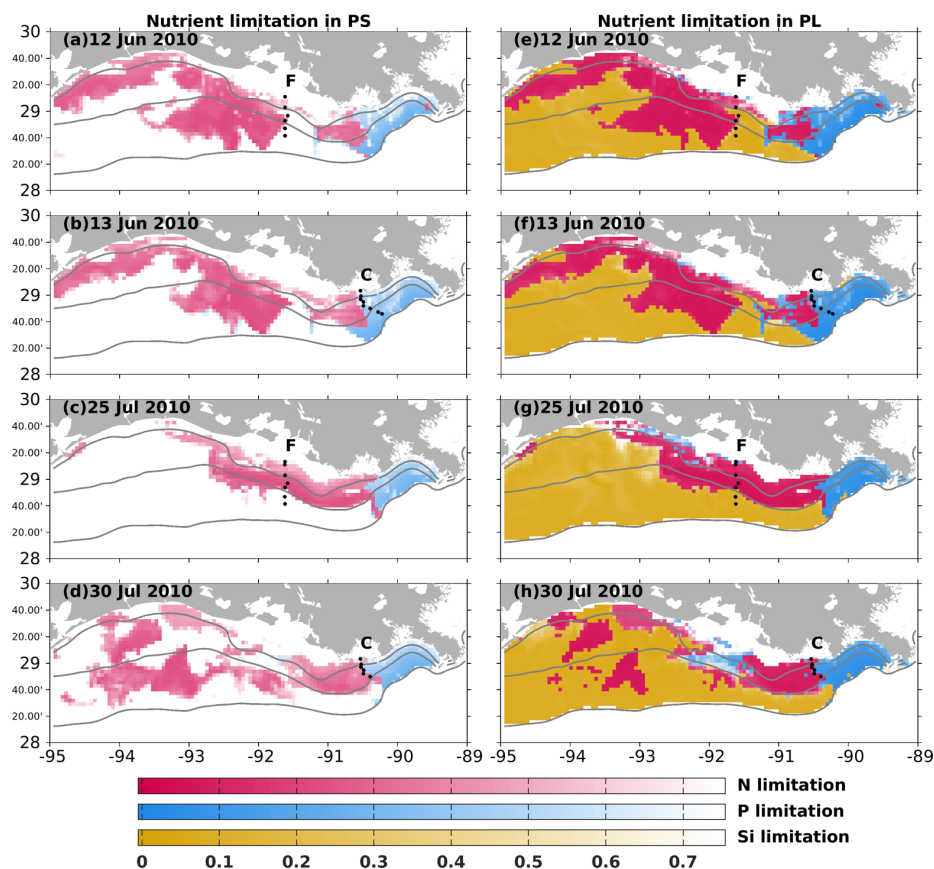
### 310 3.3 Nutrient limitation

311 Nutrient limitation could vary among different phytoplankton species with different efficiencies in nutrient uptakes. In our  
 312 model, the Si limitation was modeled only for the PL growth. Depth-averaged nutrient limitation coefficients (see Eqs. A9–  
 313 A10) over the surface 1 m were compared to bioassay studies. When a modeled coefficient is lower than 0.75, the water body  
 314 is defined to be limited by the corresponding nutrient for the corresponding phytoplankton group. A bioassay study by Turner  
 315 and Rabalais (2013) demonstrated that N limitation was more common than P limitation along transects C and F in June and  
 316 July 2010 (Fig. 4). All July samples were found to be N limited, while only some June samples along transect C were found  
 317 to be P limited with the rest to be N limited. The model mostly captured the dominated N limitation pattern along both transects.  
 318 As there was a lack of location information in this bioassay study, we could not pinpoint the location of the observed P  
 319 limitation in Fig. 4. However, our model indicated that the P limitation was more common around the Mississippi River mouth  
 320 for both phytoplankton groups. In June 2010, transect C, located at the boundary of the modeled N and P limitation, showcased  
 321 that the model could successfully capture the observed spatial pattern of nutrient limitation.

322



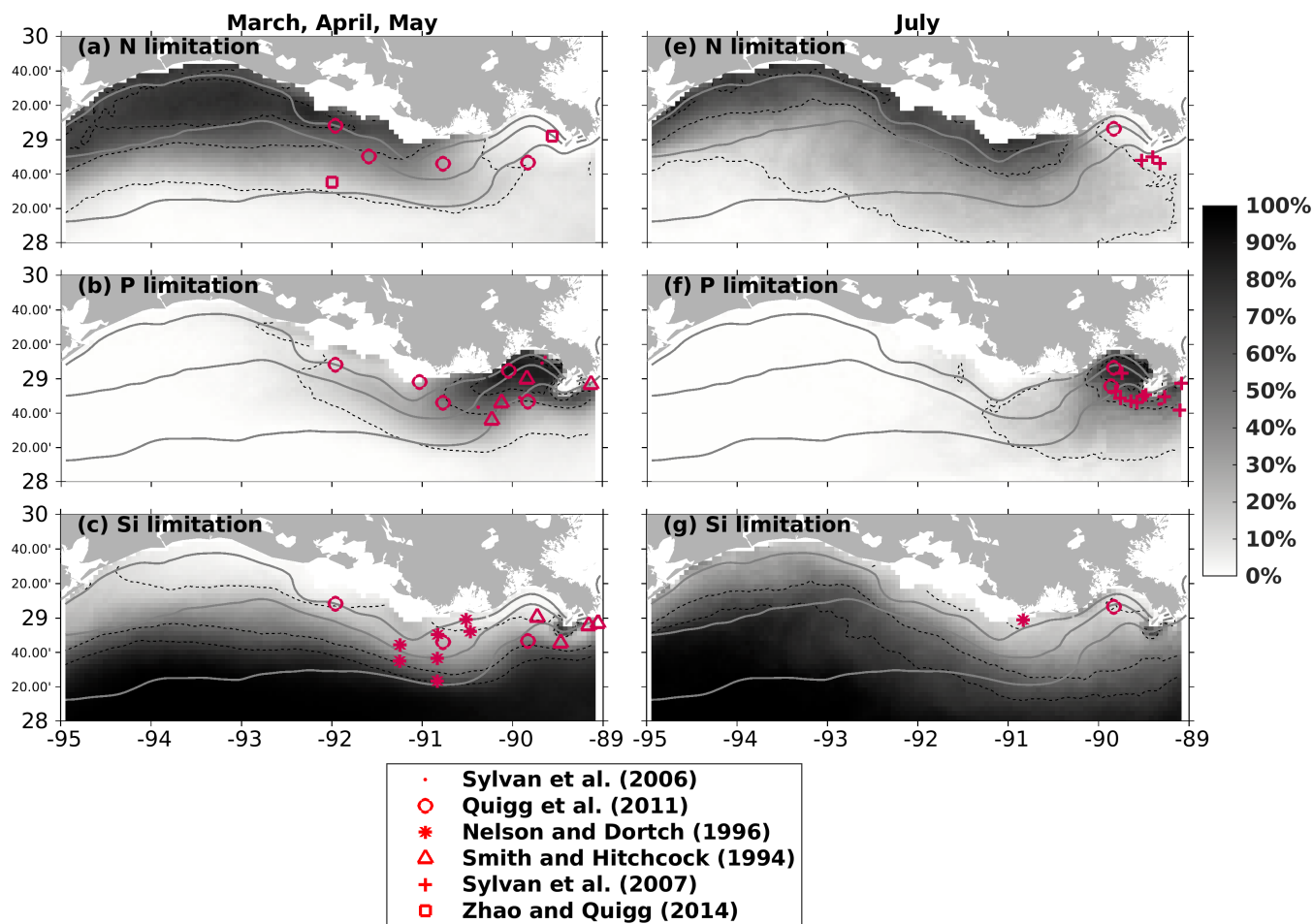
323 Dominated P limitation adjacent to the Mississippi River mouth was observed in other bioassay studies (e.g., Quigg et al.,  
324 2011; Smith and Hitchcock, 1994; Sylvan et al., 2006, 2007) and was also captured by the model indicated by high percentage  
325 occurrences over the simulation period (2007–2020) (Figs. 5b, 5e). N limitation was mostly found in the shallow parts of the  
326 middle and western shelf during spring (Fig. 5a) and became more widespread offshore and eastward in July (Fig. 5d). This  
327 pattern was also seen in earlier bioassay estimates (e.g., Quigg et al., 2011; Sylvan et al., 2007; Zhao and Quigg, 2014). The  
328 Si limitation occurrence performed a distinct offshore gradient in spring (Fig. 5c). Bioassay studies have illustrated that Si  
329 limitation occurred in the east shelf during spring (e.g., Quigg et al., 2011; Nelson and Dortch, 1996; Smith and Hitchcock,  
330 1994). The gradient tilted westward in July, indicating a potential oligotrophic water intrusion from deep waters when the  
331 circulation pattern changed during the summer months. However, there exists a knowledge gap regarding Si limitation over  
332 the western shelf region, where no known bioassay studies have been conducted. We gather some clues from Dortch and  
333 Whitlege's (1992) study of spring 1988 and summer 1987 in the Mississippi plume (mostly east of 90°W with depth >50 m),  
334 where they found that Si had a higher potential as a limiting nutrient than N in summer at high salinity waters. Salinity in the  
335 western shelf is usually high in July due to the changing predominant current system from westward to eastward or  
336 northeastward. The low-saline and Si-rich plume waters can be replaced by deep waters with higher salinity and lower Si. We  
337 expect a more Si-limited environment in the western shelf than in other parts during July, which, however, needs further  
338 support from additional bioassay studies.  
339



340

341 Figure 4. Comparisons of nutrient limitation patterns between model hindcast and a bioassay study (samples from 2010 mid-summer  
 342 shelf-wide cruises ) by Turner and Rabalais (2013) for June and July 2010. According to the bioassay study, in June, some samples  
 343 along transect C were limited by P, while all samples along transect F were limited by N; in July, all samples along both transects  
 344 were limited by N. Modeled nutrient limitation coefficients (for PS, left column; for PL, right column) are averaged over the surface  
 345 1 m. A lower coefficient indicates the corresponding nutrient is more limited.

346



347

348 **Figure 5. Modeled nutrient limitation occurrences (in percentages) overlaid with locations of observed limited nutrients by bioassay**  
 349 **studies in spring (left column) and July (right column). Modeled occurrences are obtained based on the entire simulation period**  
 350 **(2007–2020). Solid grey lines indicate bathymetry of 10, 20, and 50 m, while black dash lines represent the contour lines of 10%,**  
 351 **50%, and 70%.**

### 352 3.4 Diatom ratios

353 Cruise observations confirmed that diatom is one of the dominated phytoplankton groups in the LaTex shelf (Schaeffer et al.,  
 354 2012; Chakraborty and Lohrenz, 2015). When compared to the Schaeffer et al.'s (2012) measurements, vertical averages of PS  
 355 and PL concentration over the surface 0.5 m at the sampled points (black dots in Fig. C2) were extracted from the model  
 356 hindcast. Statistics of modeled diatom ratios were derived from the daily ratios at the selected locations over the cruise months  
 357 in 2008. When compared to Chakraborty and Lohrenz's (2015) measurements, we only calculated the modeled diatom ratios  
 358 at the surface, middle, and bottom layers. Statistics of modeled ratios were given based on the daily ratios at these layers over  
 359 the cruise regions (polygons shown in Fig. C2) and during cruise months in 2009 and 2010. The modeled ratios reasonably  
 360 reproduced the measured ones in magnitudes, monthly variability, and cross-shelf variability (Table 1). During the cruise  
 361 periods in 2008, the range of modeled diatom percentage (59% to 87%) matched well with the measurements (71% to 86%)

362 except for May 2008, when underestimations were found. In 2009, our model results agreed well with the measurements in  
 363 inner shelf waters but overestimated the measurements in the mid-shelf regions, especially in the summer and fall of 2009.  
 364 The measured percentages exhibited salient monthly variations with higher values in winter and spring and lower ones in  
 365 summer and fall. In the cross-shelf direction, the phytoplankton community shifted from a highly diatom-dominated one in the  
 366 inner shelf waters to a less diatom-dominated one in the mid-shelf waters, especially in summer. It should be noted that a high  
 367 uncertainty was found in the diatom ratio from both hindcast and measurements (comparable standard deviation against mean  
 368 values). Therefore, model-measurement biases are expected when comparing statistics derived from a whole month (model  
 369 hindcast) and a few days (cruise measurements). Then, the biases should be acceptable as the magnitudes of modeled and  
 370 measured statistics are closed.

371

372 **Table 1. Comparison of simulated (mean  $\pm$  1SD) and measured (mean  $\pm$  1SD in parentheses) diatom percentage of the total**  
 373 **phytoplankton. Note that the statistics for the simulated percentages were conducted based on concentration values over the cruise**  
 374 **months and over regions that cover the cruise sampling locations (Fig. C2). The measured percentages by Schaeffer et al. (2012) (for**  
 375 **measurements in 2008) were calculated based on biovolume values, while those by Chakraborty and Lohrenz (2015) (for**  
 376 **measurements in 2009 and 2010) were given by chlorophyll *a* attributed to different phytoplankton groups.**

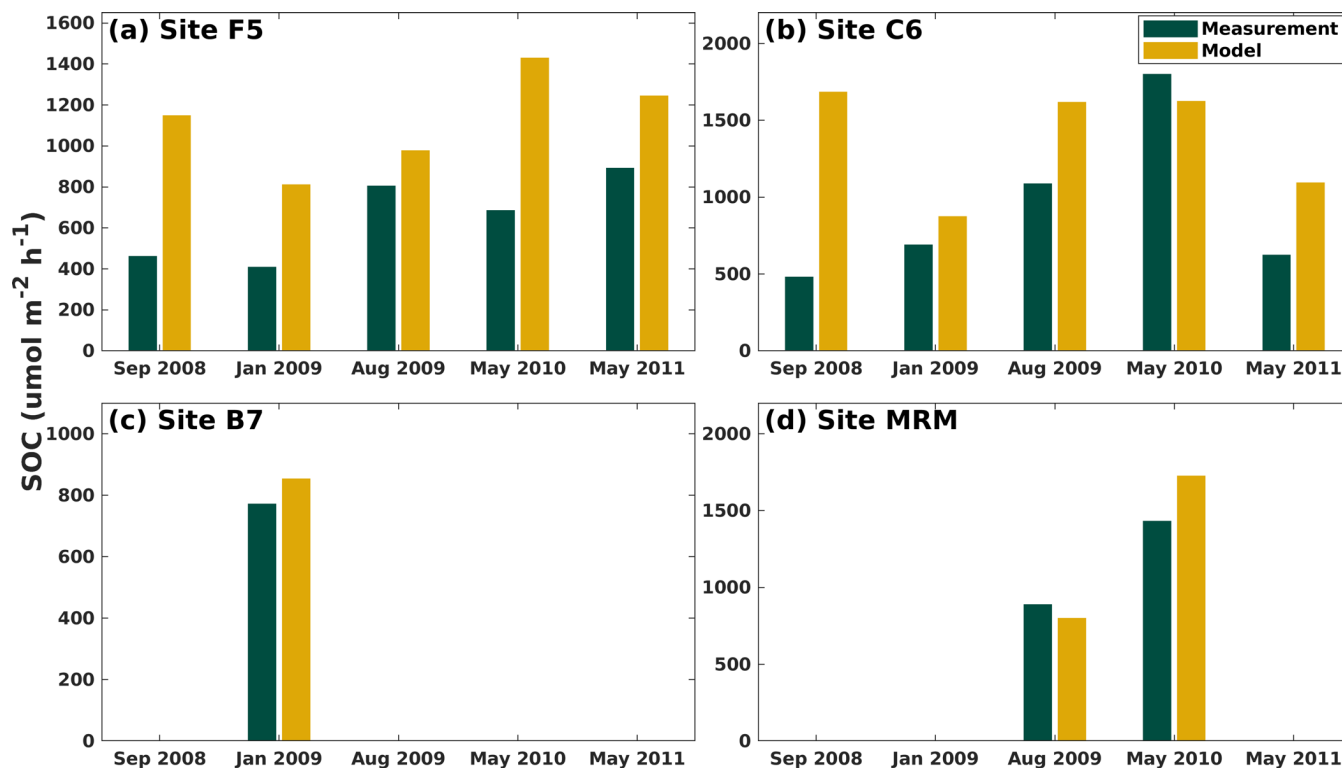
	Diatom/total phytoplankton $\times$ 100%	
	Inner shelf	Mid shelf
February 2008	68 $\pm$ 30 (71 $\pm$ 47)	
April 2008	71 $\pm$ 39 (71 $\pm$ 17)	
May 2008	59 $\pm$ 45 (80 $\pm$ 24)	
June 2008	87 $\pm$ 22(86 $\pm$ 10)	
January 2009	46 $\pm$ 36 (66 $\pm$ 21)	48 $\pm$ 13 (47 $\pm$ 14)
April 2009	46 $\pm$ 37 (59 $\pm$ 14)	46 $\pm$ 17 (33 $\pm$ 29)
July 2009	63 $\pm$ 31 (40 $\pm$ 13)	44 $\pm$ 26 (13 $\pm$ 16)
October–November 2009	53 $\pm$ 35 (46 $\pm$ 14)	41 $\pm$ 18(19 $\pm$ 17)
March 2010	47 $\pm$ 39 (50 $\pm$ 14)	50 $\pm$ 24 (64 $\pm$ 12)

377

### 378 3.5 SOC rates

379 Modeled SOC rates were compared against a laboratory incubation study by McCarthy et al. (2013) at five shelf sites (location  
 380 see the Fig. 1 in that paper) using sediment and water samples collected during six cruises (i.e., July 2008, September 2008,  
 381 January 2009, August 2009, May 2010, and May 2011). The modeled SOC was averaged over the cruise months for four shelf  
 382 sites (i.e., F5, C6, B7, and MRM; Fig. 2b). Our model could well capture the SOC magnitude. The model generally

383 overestimated the SOC at all sites except for May 2010 at site C6, and August 2009 at sites MRM (Fig. 6). The largest  
 384 overestimations were found in September 2008 when measurements were carried out shortly after Hurricanes Gustav and Ike.  
 385 These measurements tended to provide a low SOC but a high water-column respiration, possibly induced by the mixing  
 386 incurred by storms. Note that the model results shown in Fig. 6 were averaged over an entire month because no exact cruise  
 387 date information was reported in McCarthy et al. (2013).  
 388



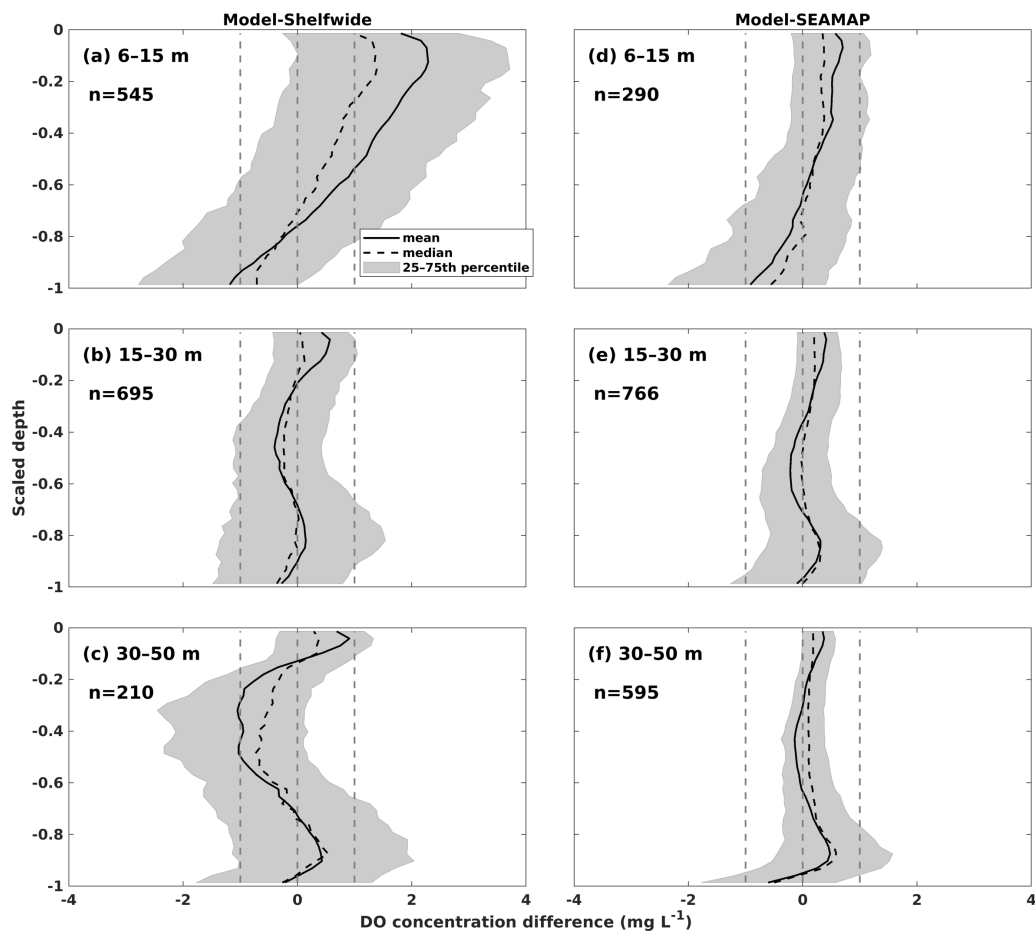
389  
 390 **Figure 6. Comparison of modeled and measured SOC (unit:  $\mu\text{mol m}^{-2} \text{h}^{-1}$ ) at four LaTex shelf sites (dark yellow dots in Fig. 2b).**  
 391 **Note that the measurements are provided by McCarthy et al.'s (2013) incubation study and the modeled SOC for each sampled site**  
 392 **is averaged over the specific months.**

### 393 3.6 DO profiles

394 Both the shelf-wide and SEAMAP cruise studies provide high-resolution measurements of DO profiles in the vertical direction,  
 395 with the observed layers ranging from surface to bottom. The number of observed layers is close to or even more than that of  
 396 the modeled layers. Therefore, the observed DO profiles were interpolated to the modeled layers using the nearest interpolation  
 397 method for the one-to-one comparisons between modeled and observed DO profiles. Mean, median, and 25-75 percentile  
 398 ranges of the model-observation differences were derived and compared against normalized depths ranging from -1 (bottom)  
 399 to 0 (surface) (Fig. 7). Most of the biases were within  $\pm 1 \text{ mg L}^{-1}$ , indicating a robust model performance in reproducing DO  
 400 profiles. We noticed the model tended to overestimate the shelf-wide observed DO by more than  $1 \text{ mg L}^{-1}$  but less than  $2 \text{ mg}$

401  $L^{-1}$  on average over the upper layers in shallow waters (Fig. 7a). When validating against the SEAMAP profiles, a wider range  
 402 of biases were also found at near-surface layers of the shallower water (Fig. 7d) than in deeper waters (Figs. 7e and 7f). On  
 403 the one hand, in shallow water, cruise measurements seldom resolved the vertical layers finer than the model where 36 layers  
 404 were designed, which introduced biases when interpolating the measured profiles to the modeled layers. On the other hand,  
 405 ROMS tends to overmix the water column in shallow water regardless of the vertical mixing parameterizations chosen  
 406 (Robertson and Hartlipp, 2017). Despite the slight overestimations of DO profiles, our model results performed better than  
 407 those of previous numerical studies. For example, DO concentration biases against profile measurements in Yu et al. (2015)  
 408 were mostly within  $2 \text{ mg L}^{-1}$ .

409



410

411 **Figure 7. Concentration difference statistics of DO profiles between model hindcasts and measurements by (a–c) NOAA’s shelf-wide**  
 412 **413 cruises and (d–f) SEAMAP. The statistics are derived from one-to-one differences between hindcasts and measurements at specific**  
 414 **415 of profiles within different depth ranges are shown in each panel.**

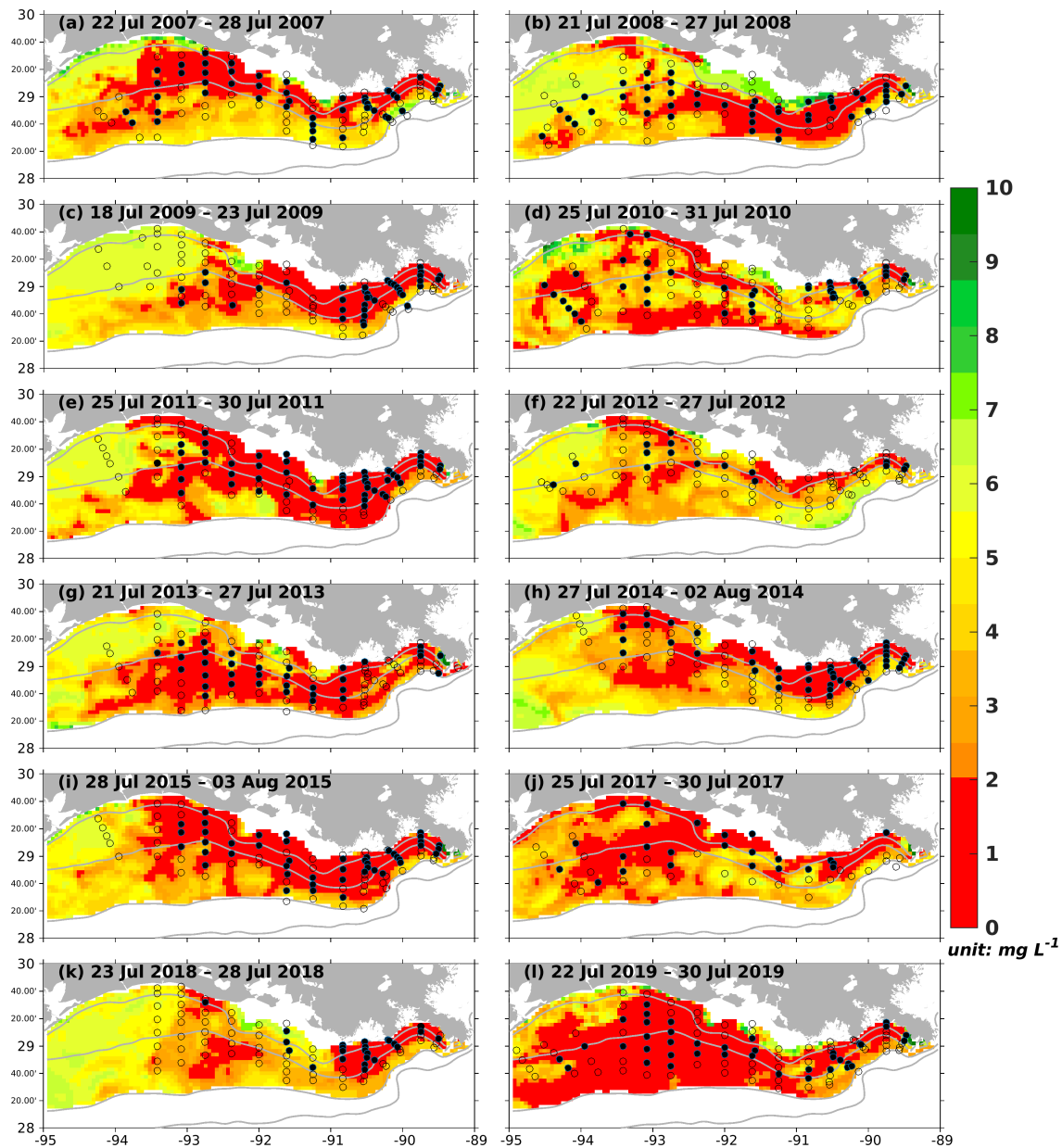
415

### 416 3.7 Spatial distributions of bottom DO and temporal variability of hypoxic area

417 As the annual NOAA shelf-wide cruises were conducted from the east shelf to the west in the summer, the model simulated  
418 bottom DO was resampled following the cruise periods. For example, if the westmost location of the cruise is 90°W on day 1,  
419 the simulated bottom DO concentration over the east of 90°W on that day is extracted. On the following day, if the westmost  
420 location of the cruise is 91°W, the simulation between 91°W and 90°W on day 2 is extracted, and so forth. All the extracted  
421 frames were blended to reconstruct the spatial distribution of simulated bottom DO concentration during the summer cruise  
422 period. Simulated results outside the LaTex shelf and over the deep (> 50 m) and shallow (< 6 m) water regions were excluded  
423 since observations were unavailable. Model results showed a good agreement with the observations in terms of interannual  
424 variability and spatial extent of bottom hypoxic waters (Fig. 8). The spatial distribution of the hypoxic regions varied over  
425 different summers. For example, the hypoxic area was small and was primarily restricted to nearshore (< 20 m) regions during  
426 the summers of 2007, 2009, 2012, 2014, and 2018. The size of the hypoxic zone was more prominent and extended offshore  
427 in 2008, 2011, 2013, and 2019. The spatial dispersion of hypoxic waters occurred mostly over the west of the LaTex shelf,  
428 where bathymetry gradients were gentle. Over the eastern shelf, the hypoxic water was mostly constrained within a narrow  
429 belt. These results suggested that the hypoxia development on the LaTex shelf was complex and generally followed the  
430 bathymetry and distances from the major river mouths.

431

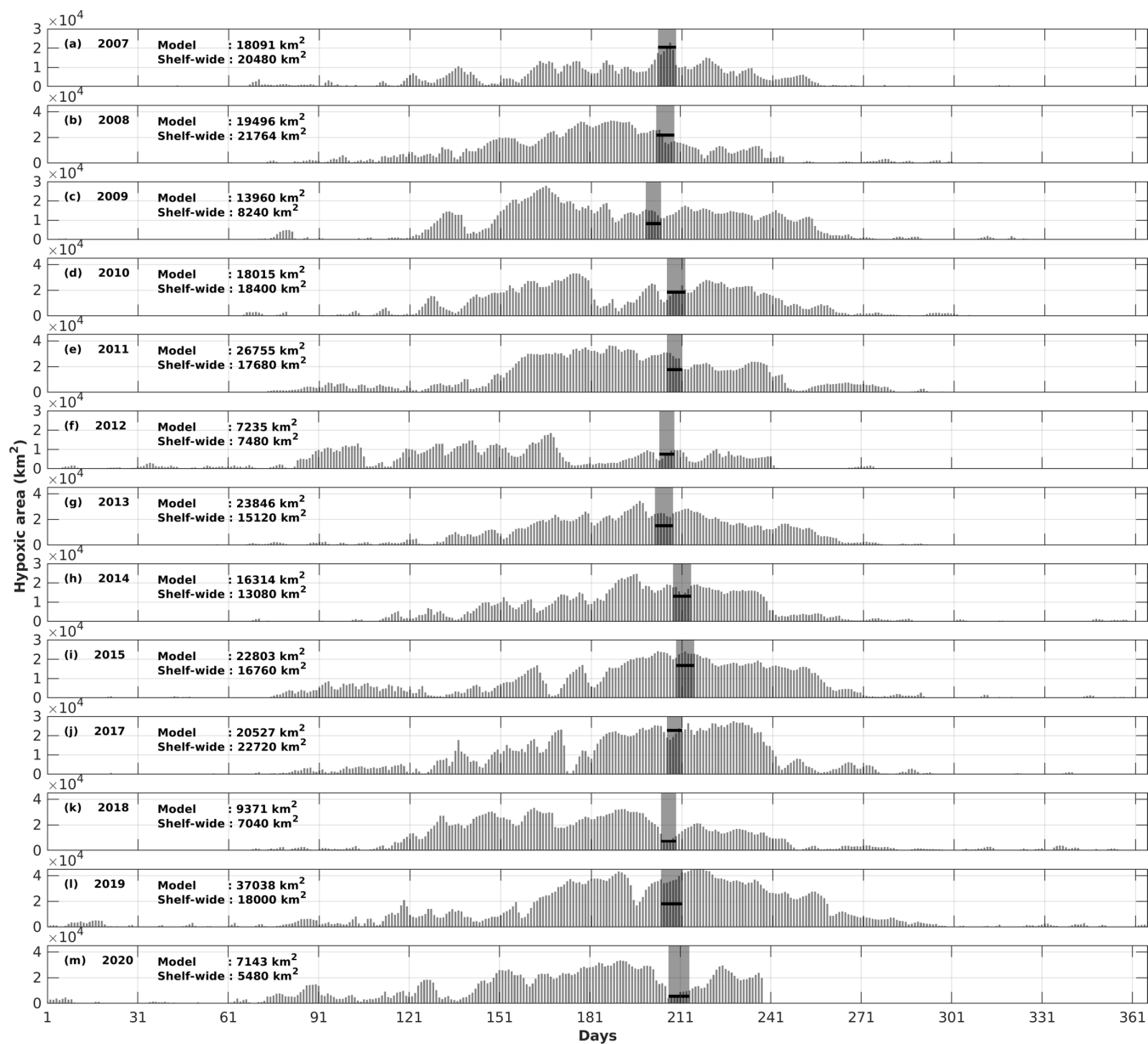
432 The daily time series of the size of the hypoxic zone was calculated over the LaTex shelf (6–50 m; Fig. 9). There was a good  
433 agreement between simulated hypoxia zone size and that captured by the shelf-wide cruises in terms of variability and  
434 magnitude. The overall correlation coefficient (CC) was 0.69 over the 99% significant level (Table 2). The 10-year running  
435 CCs ranged from 0.66 to 0.76, surpassing at least the 95% significance threshold. Underestimations were found in 2007, 2008,  
436 and 2017 with a root-mean-squared error (RMSE) of 1693 km<sup>2</sup>, while overestimates in other summers of interest with a  
437 RMSE=8084 km<sup>2</sup>. The model performed apparent overestimation for 2019 summer. Nevertheless, biases in other summers  
438 were acceptable, considering the relative sporadic converges of cruise data.



439

440 **Figure 8. Modeled summer bottom DO concentration (colored patches) and NOAA's summer shelf-wide hypoxia observations (black**  
 441 **dots and open circles). The black dots and the open circles are indicators of observed bottom hypoxia and normoxia, respectively.**  
 442 **The solid grey lines indicate bathymetry of 10, 20, 50, and 100 m.**





443

444 Figure 9. Comparison of the hypoxic area (in km<sup>2</sup>) between model simulations and shelf-wide cruise observations from 2007  
 445 to 2020 (except 2016). The grey patches denote the cruises periods while the solid black lines represent the measured hypoxic  
 446 area.

447

448

449

450

451 **Table 2. The overall (2007–2020) and 10-year running correlation coefficients (CCs) of summer hypoxic area between model**  
452 **simulations and shelf-wide measurements. Note that the comparison in 2016 is excluded due to the lack of measurement. Superscripts**  
453 **\* and \*\* indicate the corresponding CCs are above the 95% and 99% significant levels, respectively.**

Year ranges	CC
2007–2020 (overall)	0.69**
2007–2017	0.66*
2008–2018	0.76**
2009–2019	0.71*
2010–2020	0.76**

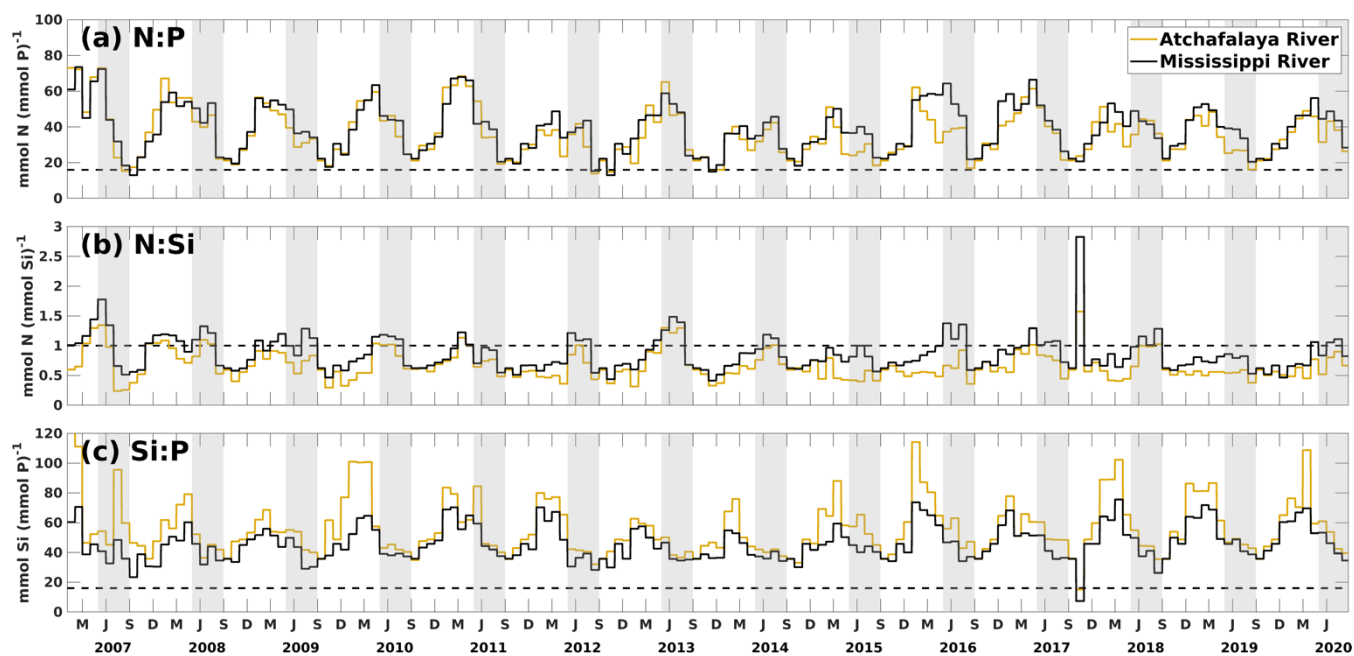
454

## 455 **4 Results and Discussion**

### 456 **4.1 Nutrient limitation**

457 In this study, the riverine nutrient loads from the Mississippi and Atchafalaya Rivers were calculated based on measurements  
458 from the USGS NWIS. During the investigated period (2007–2020), the riverine N:P ratio was higher than 16:1 during spring  
459 and reached its minimum in mid-summer to early fall (Fig. 10a). It indicated that P limitation in the shelf could be more severe  
460 in spring than in mid-summer and early fall (also seeing Fig. 5). Most riverine N:Si ratios fluctuated between 0.5 and 1 and  
461 were slightly higher in late spring and summer than in other seasons (Fig. 10b). The riverine N and Si loads were at a similar  
462 level when compared to the Redfield ratio of N:Si=1:1. However, recent studies have pointed out that marine diatoms require  
463 a lower N:P:Si ratio (16:1:20, Billen and Garnier, 2007; Royer, 2020), indicating that N may be more excessive over Si than  
464 previous thought. Riverine Si:P ratios were much higher than 16:1 and 20:1, suggesting that the major river systems transported  
465 excessive Si over P to the LaTex shelf. From the perspective of riverine supply, the plume's extent appeared to be more  
466 constrained by P availability (see Figs. 4–5) than by N and Si. The limitation effects of N and Si might be relatively similar,  
467 given that the N:Si ratio was around 16:20. However, the nutrient limitation is also related to the phytoplankton assimilation  
468 efficiency on nutrients (half-saturation coefficients for nutrient uptakes) and the water exchanges between the shelf and the  
469 adjacent waters.

470



471  
 472 **Figure 10.** Daily time series of ratios of nutrient loads from the Mississippi and Atchafalaya Rivers. The black dashed lines denote  
 473 the nutrient ratios of 16:1, 1:1, and 16:1 in (a), (b), and (c), respectively. The gray patches indicate the late spring and summer (May–  
 474 August) each year. The capitalized letters M, J, S, and D in the x-axis denote the first day of March, June, September, and December,  
 475 respectively.

476  
 477 The half-saturation coefficient for phytoplankton nutrient uptake is a critical factor associated with nutrient limitation. In our  
 478 model, PL was parameterized to be more competitive than PS in nutritious waters with a higher half-saturation coefficient.  
 479 The half-saturation coefficients for  $\text{NO}_3$  and  $\text{NH}_4$  used in this model study (Table B4) followed the parameterization in  
 480 Shropshire et al. (2020). The half-saturation coefficients for  $\text{PO}_4$  were designed as  $0.03125 \text{ mmol P m}^{-3}$  for the PS and  $0.1875$   
 481  $\text{mmol P m}^{-3}$  for the PL, according to the Redfield stoichiometry of  $\text{N:P}=16:1$ . This parametrization method was also applied in  
 482 Laurent et al. (2012) for discussion of P limitation effects in the LaTex shelf. The half-saturation coefficient for  $\text{Si(OH)}_4$   
 483 ( $K_{\text{SiOH}_4}$ ) was designed to be  $6.0 \text{ mmol Si m}^{-3}$ , mirroring the choice in Shropshire et al. (2020), although there was no discussion  
 484 on how this parameter was determined. Uptake kinetic studies for different marine diatom species have suggested a wide range  
 485 of  $K_{\text{SiOH}_4}$  from 0.8 to  $17.4 \text{ mmol Si m}^{-3}$  (Table 6). The average, median, first, and third quartile of the measured coefficients  
 486 in Table 6 were 5.9, 4.5, 2.3, and  $7.0 \text{ mmol Si m}^{-3}$ , respectively. We opted for the average over the median coefficient in our  
 487 model, considering the PL group as a representative marine diatom assemblage. However, the  $K_{\text{SiOH}_4}$  for a diatom assemblage  
 488 may shift given changing ambient silicate concentration. For example, as pointed out by Nelson and Dortch (1996),  $K_{\text{SiOH}_4}$  for  
 489 the sampled phytoplankton assemblage (dominated by diatom species) remained low from 0.48 to  $1.71 \text{ mmol Si m}^{-3}$  when the  
 490 ambient silicate concentration was low between 0.13 to  $0.41 \text{ mmol Si m}^{-3}$ , but increased to  $5.29 \text{ mmol Si m}^{-3}$  as ambient silicate  
 491 concentration was  $4.72 \text{ mmol Si m}^{-3}$ . Along Mississippi and Atchafalaya River plumes, which deliver silicate-rich waters to

492 the shelf (average concentrations are  $118 \pm 23 \text{ mmol m}^{-3}$  and  $116 \pm 21 \text{ mmol m}^{-3}$ , respectively), the silicate concentration  
 493 remains high, suggesting a high half-saturation coefficient. We acknowledged that a constant half-saturation coefficient cannot  
 494 fully capture the dynamics of silicate and diatom outside the plumes, as indicated by Nelson and Dortch (1996). Further  
 495 investigations and improvements in model parameterization for the dependency of  $K_{SiOH_4}$  on silicate concentration are needed  
 496 in future studies.

497

498 **Table 6. Half-saturation coefficient (unit:  $\text{mmol Si m}^{-3}$ ) for silicate uptake by different diatom species according to multiple uptake**  
 499 **kinetic studies.**

Diatom species	$K_{SiOH_4}$	Reference
<i>Cylindrotheca fusiformis</i>	0.85	Del Amo and Brzezinski (1999)
<i>Nitzschia alba</i>	6.8	Azam (1974)
<i>Nitzschia alba</i>	4.5	Azam et al. (1974)
<i>Phaeodactylum tricorutum</i>	4.0, 9.2, 6.3	Del Amo and Brzezinski (1999)
<i>Thalassiosira nordenskiöldii</i>	2.8	Kristiansen and Hoell, (2002)
<i>Thalassiosira pseudonana</i>	7.04	Thamatrakoln and Hildebrand (2008)
<i>Thalassiosira pseudonana</i>	1.4	Del Amo and Brzezinski (1999)
<i>Thalassiosira pseudonana</i>	0.8, 2.3	Nelson et al. (1976)
<i>Thalassiosira weissflogii</i>	15.2, 17.4	Milligan et al. (2004)
<i>Thalassiosira weissflogii</i>	4.5	Del Amo and Brzezinski (1999)
Average	5.9	
Diatom functional group (PL)	6.0	This study

500

501 The changing coastal wind and current systems during summer can lead to significant changes in nutrient distribution,  
 502 alternating the growth of phytoplankton and summer hypoxia development. Here, we show three snapshots in August 2019  
 503 (Fig. 11) when seasonal hypoxia reached its maximum (Fig. 9) to demonstrate the highly varying shelf hydrodynamics and the  
 504 resultant nutrient dispersion patterns. During spring, the westward alongshore current system dominated the LaTex shelf, while  
 505 in summer, currents shifted eastward and southward, forming a clockwise circulation in the middle and western shelf (Fig.  
 506 11a). This shift not only pushed the river plume eastward but allowed water intrusion from the west and deep gulf. Waters  
 507 from the outer shelf were typically high in salinity and low in nutrient content with higher N:Si and lower Si:P ratios than local  
 508 waters (Fig. 11c–11e). Although silicate concentration remained high and was usually excessive in the plume area, the intrusion  
 509 of deep gulf waters led to an enlarging Si limitation domain in the west LaTex shelf (Fig. 11f–11g). The PL concentration and  
 510 primary production (PS+PL) (Fig. 11h–11j) in the western shelf decreased pronouncedly after the intrusion of Si-limited  
 511 waters. Pronounced declines in  $\text{PON}_{\text{sed}}$  concentration (Fig. 11k) in the shallow western shelf were also detected five days after

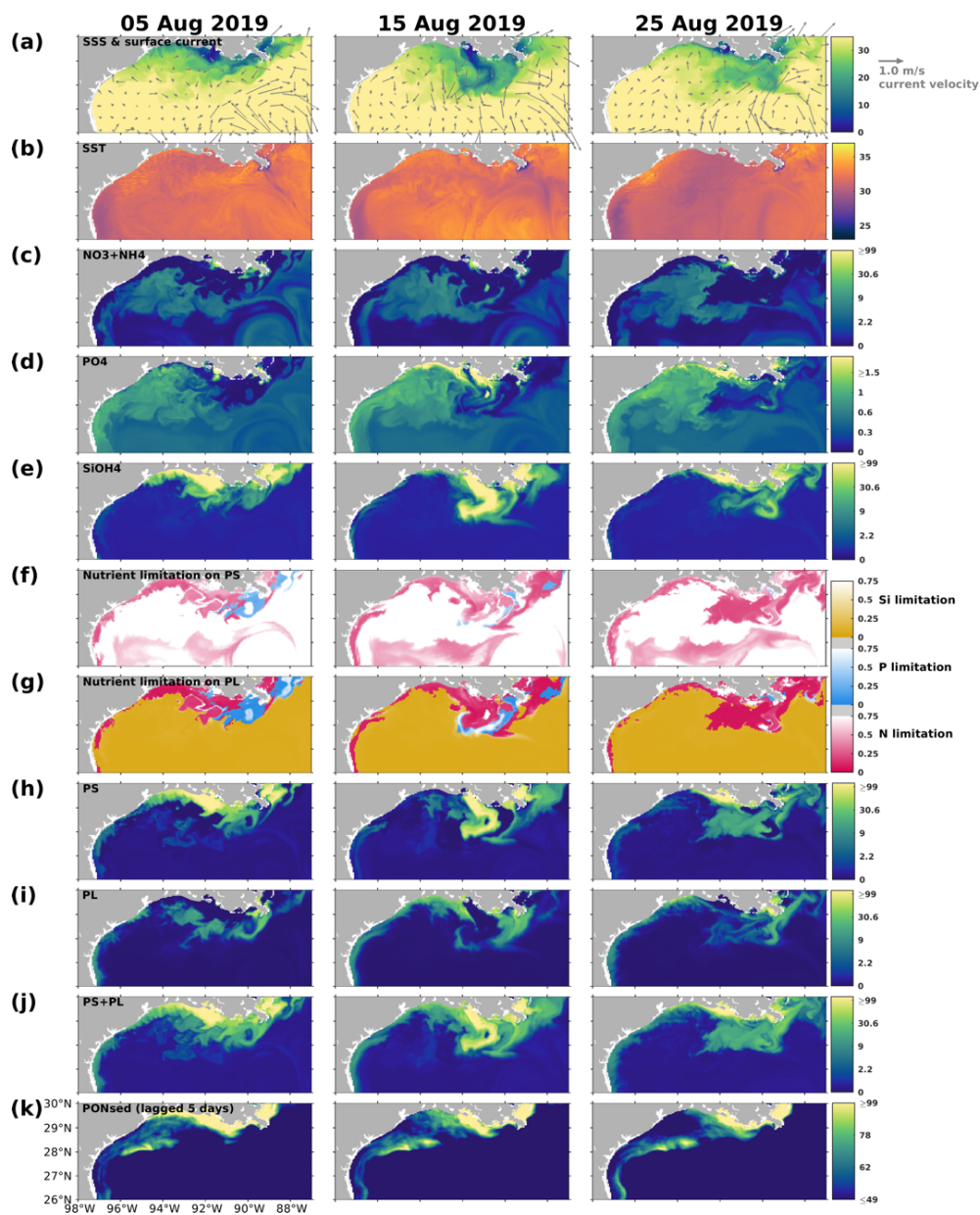
512 the primary production decreased. The SOC was expected to decrease, which could relieve the summer bottom hypoxia in the  
513 shallow western shelf.

514

515 We also noted that the upwelling system along the nearshore far western shelf ( $> 95^{\circ}\text{W}$ ) and the direct transport of PON from  
516 the west could affect the evolution of bottom hypoxia on the LaTex shelf. In the northern hemisphere, the clockwise circulation  
517 system was favorable for the development of coastal upwelling systems, which induced cooling at the surface along the coast  
518 (Fig. 11b), and led to elevated concentrations of surface inorganic nitrogen, phosphate, and silicate along the nearshore western  
519 shelf. Total surface primary production remained high roughly along the 20 m isobath, where the water column PON  
520 concentration was also elevated. The clockwise circulation system carried the PON offshore and northeastward to the LaTex  
521 shelf, inducing an increase in the  $\text{PON}_{\text{sed}}$  pool (around  $28^{\circ}\text{N}$ ; Fig. 11k) and SOC. The high alongshore production was limited  
522 by N rather than Si or P. However, the N limitation band narrowed around the coastal upwelling zones. Such patterns—  
523 including low-Si water intrusion, eastward transport of PON, and a narrow N limitation band in the upwelling zone—were  
524 also found in other summer snapshots when the current system changed (e.g., Fig. C3).

525

526 Previous bioassay studies suggested the potential Si limitation on the LaTex shelf (Quigg et al., 2011; Nelson and Dortch,  
527 1996; Smith and Hitchcock, 1994; Lohrenz et al., 1999). However, N and P limitations were reported more frequently than Si  
528 limitations along the shelf. Part of the reason was that samples collected in previous studies were mainly from the eastern shelf,  
529 where N and P typically appeared to be limited. Our understanding of potential nutrient limitations, particularly in the western  
530 shelf during the recent decade, still needs to be completed. Nevertheless, this lack of *in situ* data should not hinder model  
531 developments, as indirect evidence supports the potential Si limitation in the western shelf, especially during the summer. For  
532 instance, a recent study using *in situ* incubations and laboratory experiments showed that the oligotrophic open gulf, generally  
533 low in N, could also be Si-limited, as indicated by lower maximum growth rates of diatoms compared to other culture and  
534 field measurements (Yingling et al., 2022). Additionally, earlier concentration measurements (Dortch and Whitley, 1992)  
535 showed that Si limitation sometimes overwhelmed the N limitation in the deep gulf waters (depth  $> 50$  m). Water exchanges  
536 between the LaTex shelf and adjacent deep waters become more pronounced in summer with changes in wind and current  
537 systems. The intrusion of low-Si waters can promote the development and expansion of Si limitation, which in turn affects the  
538 phytoplankton community and oxygen dynamics. Therefore, the accuracy of the boundary conditions along the LaTex shelf is  
539 crucial in biogeochemical modeling. Indeed, earlier numerical studies (e.g., Fennel et al. 2013) emphasized the significance of  
540 the correct physical boundary conditions for hypoxia modeling. Our results further illustrate that biogeochemical boundary  
541 conditions, such as nutrient concentrations, are as critical as river forcings in influencing the shelf's nutrient distribution,  
542 plankton, and oxygen dynamics. These effects have yet to be addressed in previous numerical studies of the LaTex shelf.



543

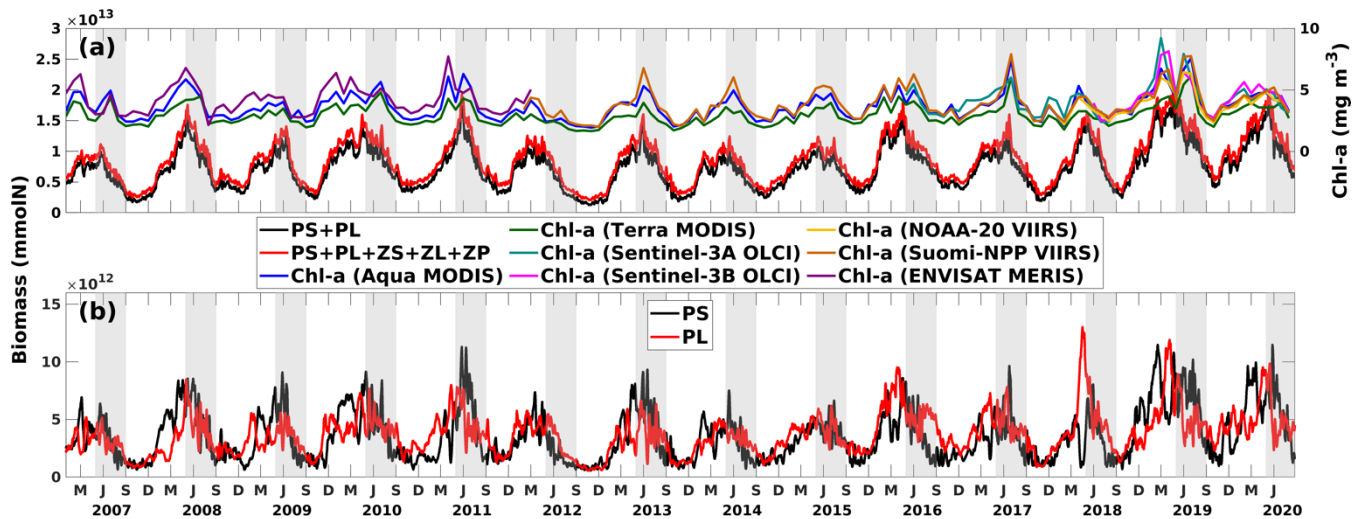
544 Figure 11. Summer snapshots of (a) sea surface salinity (overlaid with surface current velocity), (b) surface temperature (°C), (c)  
 545 surface total inorganic nitrogen concentration ( $\text{mmol N m}^{-3}$ ), (d) surface phosphate concentration ( $\text{mmol P m}^{-3}$ ), (e) surface silicate  
 546 concentration ( $\text{mmol Si m}^{-3}$ ), (f–g) surface nutrient limitation coefficients, (h–i) surface phytoplankton concentration ( $\text{mmol N m}^{-3}$ ),  
 547 and (k)  $\text{PON}_{\text{sed}}$  concentration ( $\text{mmol N m}^{-3}$ ) with a 5-day lag in the nGoM. The nutrient, phytoplankton, and  $\text{PON}_{\text{sed}}$  concentrations  
 548 are displayed in the log<sub>10</sub> scale.

549

## 550 4.2 Plankton community interactions

551 On the LaTex shelf (Fig. 2b colored area), total production, primarily supported by the primary production (Fig. 12a), exhibited  
 552 a bi-peak pattern in spring and summer (e.g., 2007, 2009, 2010, 2014, 2015, 2016, 2017, 2019, and 2020) with both peaks  
 553 being of similar magnitude. This pattern was hardly captured by numerical models featuring a less complex plankton  
 554 community (e.g., Fennel et al., 2011) and was seldom reported or discussed even in model simulations where this pattern  
 555 appeared (see comparisons of modeled and satellite-derived chlorophyll *a* concentration in Gomez et al., 2018). Satellite-  
 556 derived chlorophyll *a* concentration from multiple products, averaged over the LaTex shelf, also showed a bi-peak pattern  
 557 from March to August (Fig. 12a), closely resembling the pattern observed in our hindcast primary production. A cruise study  
 558 conducted in March, May, and July 2004 similarly depicted a higher chlorophyll *a* peak in May and a lower one in July (Quigg  
 559 et al., 2011). The bi-peak pattern shown was attributed to the negative correlation between PS and PL time series, where a  
 560 decrease in PS typically coincided with an increase in PL, and vice versa (Fig. 12b). For example, the peaks in primary  
 561 production and chlorophyll *a*, observed from March to May 2019, coincided with the transition from a PS peak to a PL peak.  
 562 The secondary peak, observed from June to July 2019, was attributed to sustained high PS biomass.

563



564

565 **Figure 12.** Daily time series of (a) PS+PL and PS+PL+ZS+ZL+ZP biomass (represented by mmol N) and (b) PS, PL separated,  
 566 integrated over the LaTex shelf (Fig. 2b colored area) and (a) monthly time series of regionally averaged (over the LaTex shelf)  
 567 chlorophyll *a* concentration (in  $\text{mg m}^{-3}$ ) derived from multiple satellite products. The gray patches indicate the late spring and  
 568 summer (May–August) period of each year. The capitalized letters M, J, S, and D in the x-axis denote the first day of March,  
 569 September, and December, respectively.

570

571 Competition for nutrients between PS and PL (bottom-up) and grazing pressure from zooplankton (top-down) jointly  
 572 contribute to the differing fluctuation patterns of PS and PL and the bi-peak total primary production pattern. However, their  
 573 effects are mostly non-linear and are not straightforward to explain. We sampled six snapshots around the primary production

574 peaks in the spring (early April) and summer (mid-June) of 2019 to illustrate the responses of both phytoplankton groups to  
575 the changing nutrient environments and grazing pressure. Analysis was based on depth averages within the surface 1 m (Figs.  
576 13–14).

577

578 In April 2019, a consistent westward current system dominated in the LaTex shelf, corresponding to an east-west elongated  
579 river plume region, as indicated by the low sea surface salinity band (Fig. 13a). The spatial pattern of total primary production  
580 (PS+PL) followed the plume, within which the PS concentration increased, and PL concentration decreased westward (Fig.  
581 13e–13g). These patterns were associated with the nutrient distribution on the shelf (Fig. 13b–13d). Inorganic nutrients were  
582 abundant around the riverine outlets and diluted and consumed westward following the currents. PL, having a greater half-  
583 saturation constant for nutrients than PS, typically achieved higher growth efficiency or reached the maximum growth rate  
584 more easily than PS when background nutrients were abundant. By contrast, PS could outcompete the PL when nutrient  
585 supplies were low. In addition, a downwelling system was established along the shallow coast in the mid and western shelf,  
586 leading to decreased nutrient concentrations and allowing PS to outcompete PL. The grazing pressure from the zooplankton  
587 group appeared to be minor and did not significantly affect the distribution of PS and PL during these days (Fig. 13h–13j).

588

589 Pronounced bottom-up and top-down effects on the primary production were found around the biomass peak in June 2019,  
590 coinciding with a shift in the coastal current system to a northward direction (Fig. 14a). The northward currents not only  
591 constrained the river plume but also introduced oligotrophic deep water, as evidenced by the high surface salinity, to the inner  
592 shelf. Note that the discharges of the Mississippi and Atchafalaya Rivers remained high from May to July 2019 (Fig. C1). A  
593 distinct difference in the patterns of PS and PL was observed between 89 and 93°W and between 93 and 97°W (Fig. 14f–14g).  
594 In the former region, where constrained river plumes and oligotrophic water intrusions were detected, PS exhibited a higher  
595 nutrient uptake efficiency than PL. In contrast, PL concentration was slightly higher than PS concentration in the latter regions,  
596 where the plume was pushed offshore. However, two areas of low PS concentration and corresponding high PL concentration  
597 were identified between 93 and 96°W, nearshore stretching from southwest to northeast, and between 91 and 92°W, stretching  
598 from nearshore to offshore. In these regions, the concentration of ZS, which grazes on PS only (Fig. 14h), was high, exerting  
599 strong grazing pressure on PS but inversely allowing PL to bloom (Fig. 14h).

600

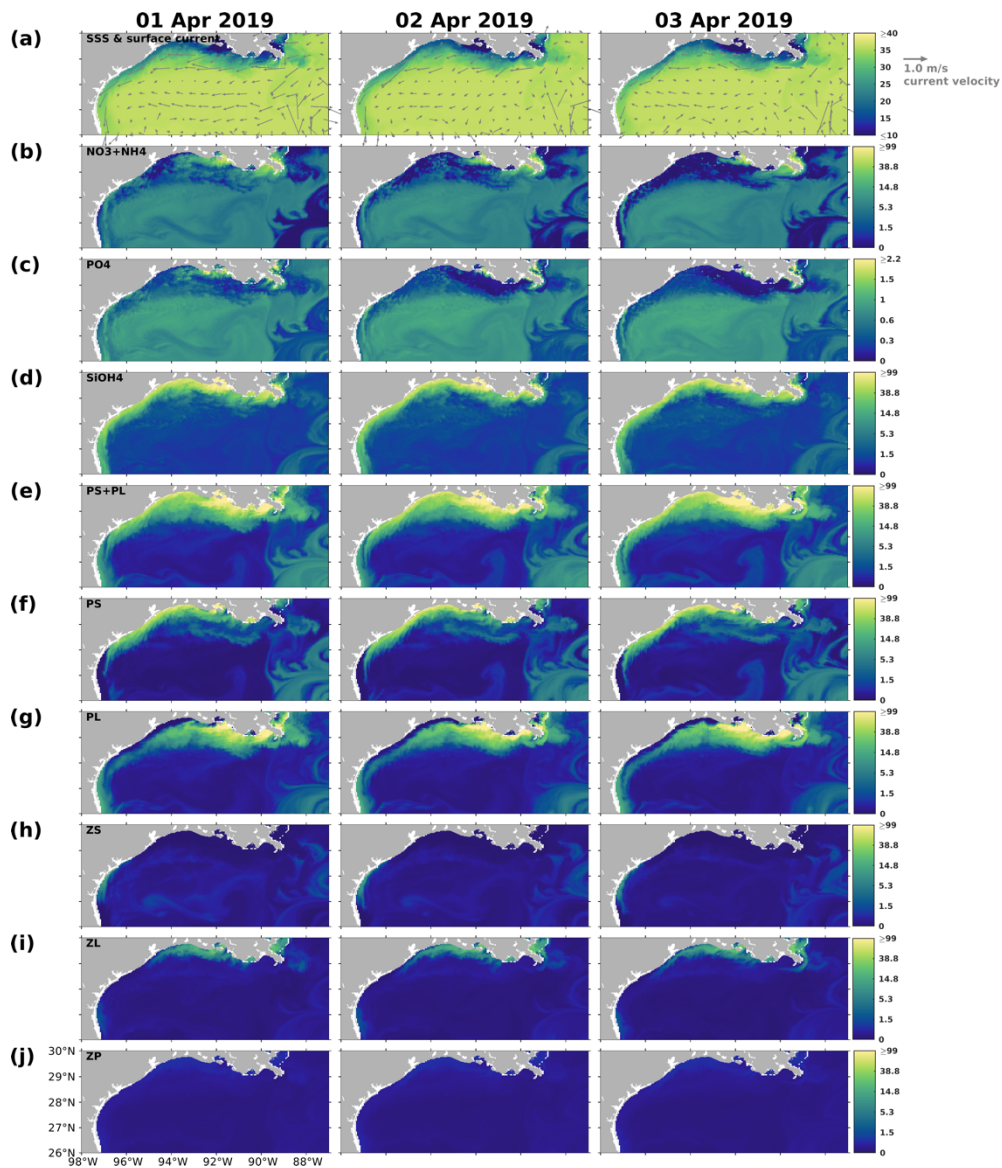
601 The results indicated that the responses in PS, PL, and PS+PL to the riverine nutrient loads were nonlinear due to the mixing  
602 among the waters on the shelf, from the river, and intruding from the deep ocean. The riverine nutrient supplies were much  
603 greater in June 2019 than in March–April 2019 (Fig. C1). A higher primary production and PL concentration in June would  
604 have been expected if a nutrient-based linear relationship had been applied. However, as shown in the model and the satellite  
605 products, primary production was higher in April than in June. This indicated that variations of phytoplankton concentration  
606 are not only affected by riverine nutrient inputs but also the current system, which limits the expansion of river plumes,  
607 pronounced upwelling or downwelling, and water exchanges with the oligotrophic open ocean. In the April and June 2019



608 snapshots, mesoscale eddies were found south of the Mississippi River outlets. The intensity and impact area of the June eddy  
609 was greater than that of the April eddy, causing a more pronounced northward flow and more constrained river plumes along  
610 the shelf in June. These eddy systems are known as Loop Current Eddy (LCE) systems, which can prorogate eastward and  
611 interact with the LaTex shelf waters after the detachment from the GoM Loop Current (LC). A recent study indicated that LCE  
612 has distinct bio-optical properties (e.g., temperature, salinity, density, DO concentration, and chlorophyll *a* concentration) from  
613 the surrounding waters, highlighting the importance of open ocean dynamics to the shelf biogeochemical processes (Zhang et  
614 al., 2023). Another recent study analyzing water samples from the LaTex shelf emphasized the significant impact of mesoscale  
615 circulation features on the summer planktonic community composition (Anglès et al., 2019). This study revealed that between  
616 20 and 25 June 2013, diatoms proliferated on the western shelf, where upwelling was detected, whereas the flagellate group  
617 dominated within the river plumes. From 18 to 23 June 2014, diatom and flagellate bloomed in proximity to the Mississippi  
618 River and Atchafalaya River outlets, respectively. In contrast, blooms on the western shelf were characterized by a mixture of  
619 the two phytoplankton groups. Similar patterns were observed in our model results, as depicted in Fig. C4–C5.

620

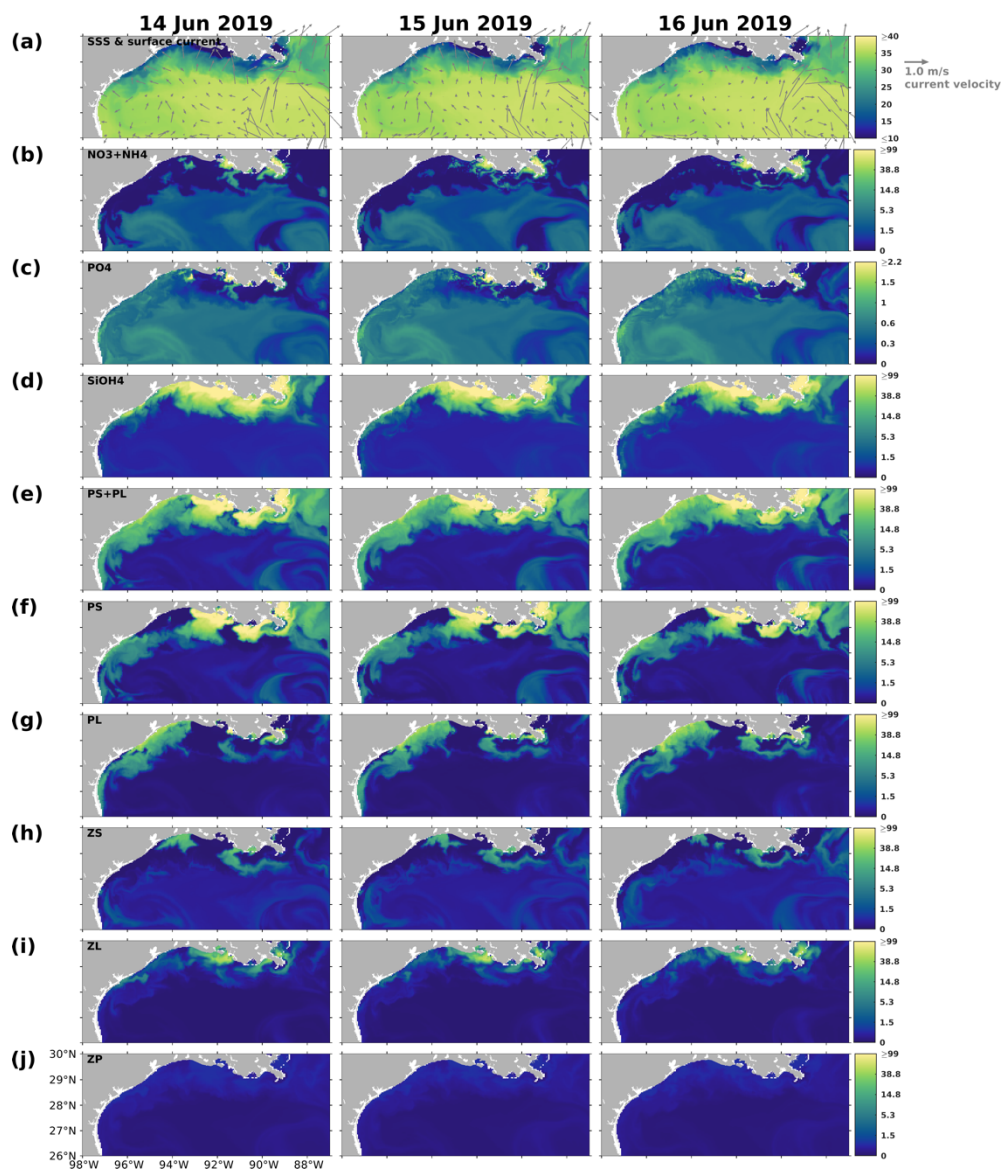
621 In addition to the impacts of upwelling and LCE systems, direct advection of river outflow waters by coastal currents was also  
622 found to be significant for phytoplankton community composition, carbon export, and the associated bottom DO conditions  
623 based on other field studies in the nGoM (Chakraborty and Lohrenz, 2015) and northeastern GoM (Qian et al., 2003). Our  
624 results suggested that the grazing pressure exerted by zooplankton groups can be variable, manifesting as significant in some  
625 instances while remaining minimal in others. Laboratory experiments on surface water samples collected around the  
626 Mississippi River outlets in May 1993 suggested significant grazing pressures by microzooplankton on the phytoplankton  
627 growth (Strom and Strom, 1996). However, no salient grazer impact was found on phytoplankton growth according to bioassay  
628 studies on the water samples collected around the plumes in April and August 2012 (Zhao and Quigg, 2014). Besides, other  
629 unmodeled factors can also affect shelf primary production. For example, a reduction of chlorophyll *a* between 2011 and 2014  
630 detected in the nGoM was attributed to the Deepwater Horizon oil spill disaster in 2010 (Li et al., 2019). Incorporating a  
631 complex community into the model to address the nonlinear interactions among different plankton groups enhances our  
632 understanding of the primary production variability and associated DO dynamics on the LaTex shelf (e.g., the bi-peak patterns  
633 that were seldom discussed before).



634

635 Figure 13. Snapshots of (a) sea surface salinity (overlayed with surface current velocity), (b) surface total inorganic nitrogen  
 636 concentration ( $\text{mmol N m}^{-3}$ ), (c) surface phosphate concentration ( $\text{mmol P m}^{-3}$ ), (d) surface silicate concentration ( $\text{mmol Si m}^{-3}$ ), (e–  
 637 g) surface phytoplankton concentration ( $\text{mmol N m}^{-3}$ ), and (h–j) surface zooplankton concentration ( $\text{mmol N m}^{-3}$ ). The nutrient and  
 638 plankton concentrations are displayed in the log<sub>10</sub> scale.

639



640  
641 Figure 14. Same as Fig. 13, but for snapshots from 14 June 2019 to 16 June 2019.

### 642 4.3 A re-examination of LaTex shelf DO dynamics

643 In this section, we specified the bottom waters as the layers within 2 meters above the sea floor, while the upper waters  
644 represented all layers above this 2-meter bottom layer. The purpose is to understand the contributions of different processes,  
645 including water column biochemistry, air-sea flux (in upper layers), SOC (in bottom layers), and water transports  
646 (advection+diffusion) to the daily variations of DO in the LaTex shelf during summers (May–August) of 2007–2020.

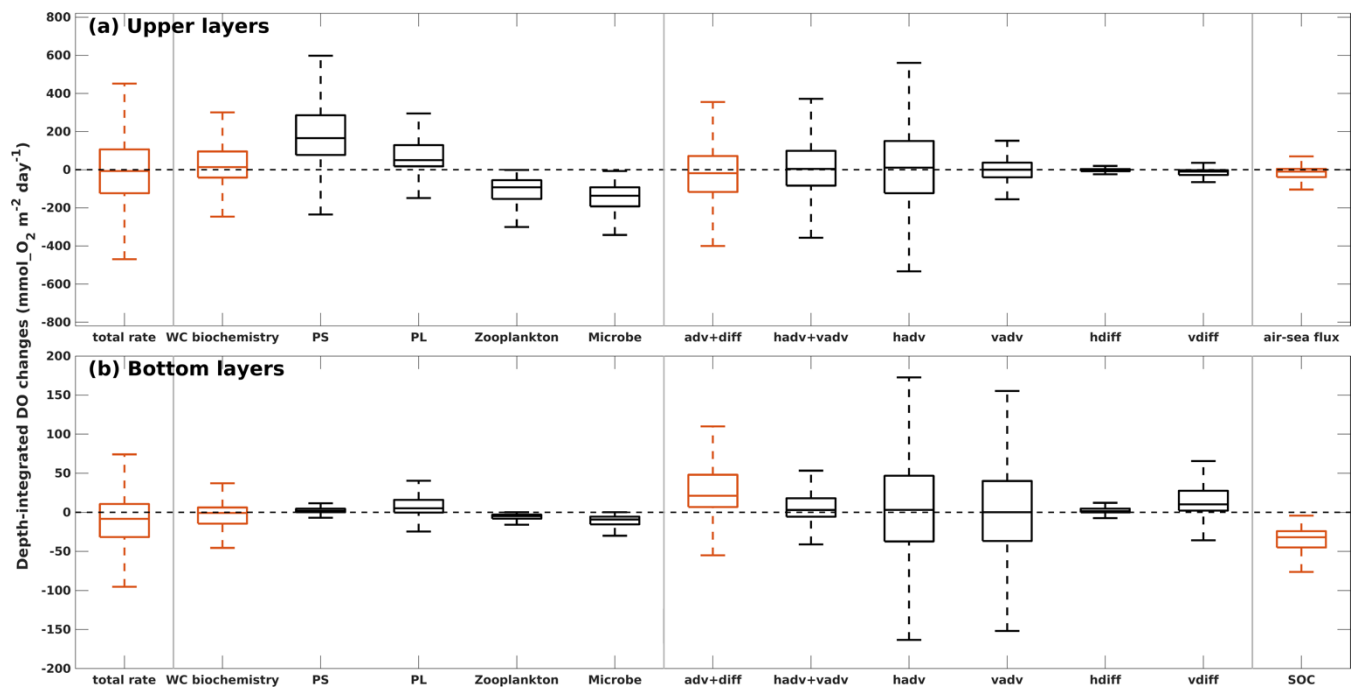
647

648 In the upper LaTex shelf, daily DO changes were primarily driven by shelf physics and local water column biochemistry (Fig.  
649 15a), as reflected by their significant contributions to the variability and magnitude. The advection and diffusion terms together  
650 explained the greatest spatiotemporal variability of total DO changes. The ranges of the first and the third quartiles were closely  
651 shown in the total rate of changes ( $-124$  to  $107$   $\text{mmol O}_2 \text{ m}^{-2} \text{ day}^{-1}$ ) and changes by water transports ( $-117$  to  $72$   $\text{mmol O}_2 \text{ m}^{-2}$   
652  $\text{day}^{-1}$ ). Detailed separation of the water transport terms indicated that horizontal advection of DO contributed the most to the  
653 variability of the physical terms. The water column biochemistry contributed the second largest to total DO variability, with a  
654 wide range of first and third quartiles ( $-41$  to  $96$   $\text{mmol O}_2 \text{ m}^{-2} \text{ day}^{-1}$ ). The phytoplankton groups contributed positively to the  
655 upper DO pool, with the majority contribution from the PS group. PS biomass was usually higher than PL biomass in summer  
656 when the allocation of nutrients was more favorable for the growth of PS. The net DO changes by water column biochemistry  
657 could be negative, indicating net metabolism, which was also reported by previous field studies demonstrating consistent net  
658 water column heterotrophy across the Louisiana shelf (e.g., Murrell et al., 2013). The air-sea interactions contributed negatively  
659 to the total DO changes and accounted for the least contribution. This indicated that the upper LaTex shelf was mostly a source  
660 of oxygen to the atmosphere during summer.

661

662 In the bottom layers, the DO variability was controlled by SOC and water transports (Fig. 15b). The SOC was steady (narrow  
663 range of quartiles), but major DO loss term (median=  $-32$   $\text{mmolO}_2 \text{ m}^{-2} \text{ day}^{-1}$ , first quartile=  $-45$   $\text{mmolO}_2 \text{ m}^{-2} \text{ day}^{-1}$ , and third  
664 quartile=  $-24$   $\text{mmolO}_2 \text{ m}^{-2} \text{ day}^{-1}$ ), driving the total rate of changes of DO to be negative at most shelf grids during summer  
665 (median=  $-8$   $\text{mmolO}_2 \text{ m}^{-2} \text{ day}^{-1}$  and first quartile=  $-32$   $\text{mmolO}_2 \text{ m}^{-2} \text{ day}^{-1}$ , and third quartile=  $11$   $\text{mmolO}_2 \text{ m}^{-2} \text{ day}^{-1}$ ). The  
666 advection and diffusion terms together acted as a major source of DO in the bottom layers (median= $21$   $\text{mmolO}_2 \text{ m}^{-2} \text{ day}^{-1}$ , first  
667 quartile= $7$   $\text{mmolO}_2 \text{ m}^{-2} \text{ day}^{-1}$ , and third quartile=  $48$   $\text{mmolO}_2 \text{ m}^{-2} \text{ day}^{-1}$ ). However, they hardly offset the DO loss due to SOC.  
668 Such a positive contribution to DO by physical transports was mainly a result of steady and strong net DO supplies through  
669 vertical diffusion, as the variability and magnitude of DO changes due to total advection were less pronounced than those due  
670 to vertical diffusion. The vertical diffusion of DO is influenced by both water stratification and vertical DO concentration  
671 gradient. Water stratification results from multiple processes, including river plume dynamics, tidal dynamics, wind patterns,  
672 surface heating and cooling, etc. has been identified as an important indicator of bottom DO supply (Hetland and DiMarco,  
673 2008; Bianchi et al., 2010; Fennel et al., 2011, 2013, 2016; Justić and Wang, 2014; Wang and Justić, 2009; Feng et al., 2014;  
674 Yu et al., 2015; Laurent et al., 2018). The variation of the vertical gradient was more related to the DO dynamics in the upper  
675 layers than in the bottom, as the DO variability is more pronounced in the upper layers (wider range in total rate of changes).  
676 Thus, while SOC and water stratification play crucial roles in DO changes in the bottom layers, DO changes in the upper shelf  
677 can affect the bottom DO through vertical diffusion.

678



679

680 **Figure 15. Depth-integrated rate of changes in DO due to different modeled processes in (a) the upper layers and (b) the bottom**  
 681 **layers. The total rate of changes is the summation of DO sources/sinks by three groups of contributors (water column biochemistry,**  
 682 **DO transports, and air-sea flux in upper layers or SOC in bottom layers) separated by vertical gray lines. In each group, DO changes**  
 683 **by specific processes are illustrated by black boxes. Boxes represent the first and third quartiles, with lower and upper whiskers**  
 684 **extending to the lowest and highest values within 1.5 interquartile range of the first and third quartiles, respectively. The median is**  
 685 **indicated by a black line in the middle of the boxes. Statistics are summarized from the summers (May–August) records of 2007–**  
 686 **2020 at all grid cells in the LaTex shelf.**

687

688 The interactions within the plankton community (e.g., competition for nutrients and grazing pressure), which led to biomass  
 689 differences, also resulted in different DO patterns at the bottom layer. Such impacts became more apparent when the DO  
 690 contribution by water biochemistry outweighed that from transport processes in the upper ocean. For illustration, three summer  
 691 snapshots of 14–16 June 2019 (Fig. 16 and 17) were sampled when widespread bottom hypoxia was detected. The water  
 692 column biochemical processes contributed more than 50 % of total DO changes in most computational cells in the upper layers  
 693 (Fig. 16a). First of all, the DO contribution by phytoplankton, zooplankton, and microbe exhibited distinct spatiotemporal  
 694 patterns, complicating the net DO changes in the upper layers. Generally, the PS and PL groups enhanced DO levels, whereas  
 695 zooplankton and microbes tended to deplete DO. During 14 June 2019, the DO losses by biochemical processes (Fig. 16b) in  
 696 the shallow western shelf were mostly attributed to high ZS metabolism (Fig. 16e); the net DO gains between 91.5 and 92.5  
 697 °W reflected high PL concentrations (Fig. 14g) and the associated high DO supplies (Fig. 16d); the scattered DO losses over  
 698 the shelf were primarily due to the homogeneously high DO consumptions by microbes (Fig. 16h). During 15 and 16 June 2019,  
 699 when DO supplies by PS and PL (Fig. 16c–16d) increased, net DO gains predominated in the shelf (Fig. 16b). However, the

700 net DO gains in the west ( $> 92.5^{\circ}\text{W}$ ) and east ( $< 91.5^{\circ}\text{W}$ ) shelf were mainly contributed by PS, while those in the middle  
701 shelf by PL.

702

703 At the same time, changes in upper DO could affect the bottom DO through vertical diffusion, of which spatial patterns (mostly  
704 positive; Fig. 17b) and daily variability aligned with biochemical DO alterations in the upper layers (Fig. 16b). However, water  
705 column stratification, as indicated by the potential energy anomaly (PEA; Fig. 17a), resulted in noticeable spatial disparities  
706 in the vertical diffusion of DO. On 15 June 2019, for example, the effects of vertical diffusion were weakened in areas that  
707 featured strong stratification, as evidenced by high PEA values. In contrast, in regions of weak stratification, such as the  
708 shallow waters between  $90.5$  and  $92.5^{\circ}\text{W}$ , vertical diffusion was markedly stronger. During the sampled period, among various  
709 factors (i.e., total advection, horizontal diffusion, water-column biochemistry, and SOC), the vertical diffusion term  
710 contributed the most to the total rate of changes in bottom DO, especially over the middle shallow shelf. As the rates of changes  
711 were daily averaged and the bottom DO concentration was sampled at UTC 00:00 on each sampled day (Fig. 17i), the elevated  
712 bottom DO level and relief of bottom hypoxia in the shallow middle shelf on 16 June 2019 were mainly due to the significant  
713 vertical diffusion on the preceding day, driven by high PL-supported DO sources and weak water stratification. Thus, through  
714 the interactions within the community in the upper ocean and DO diffusion processes between the upper and bottom layers,  
715 the influence of planktonic community complexity on the bottom DO dynamics and the hypoxia evolution is evident.

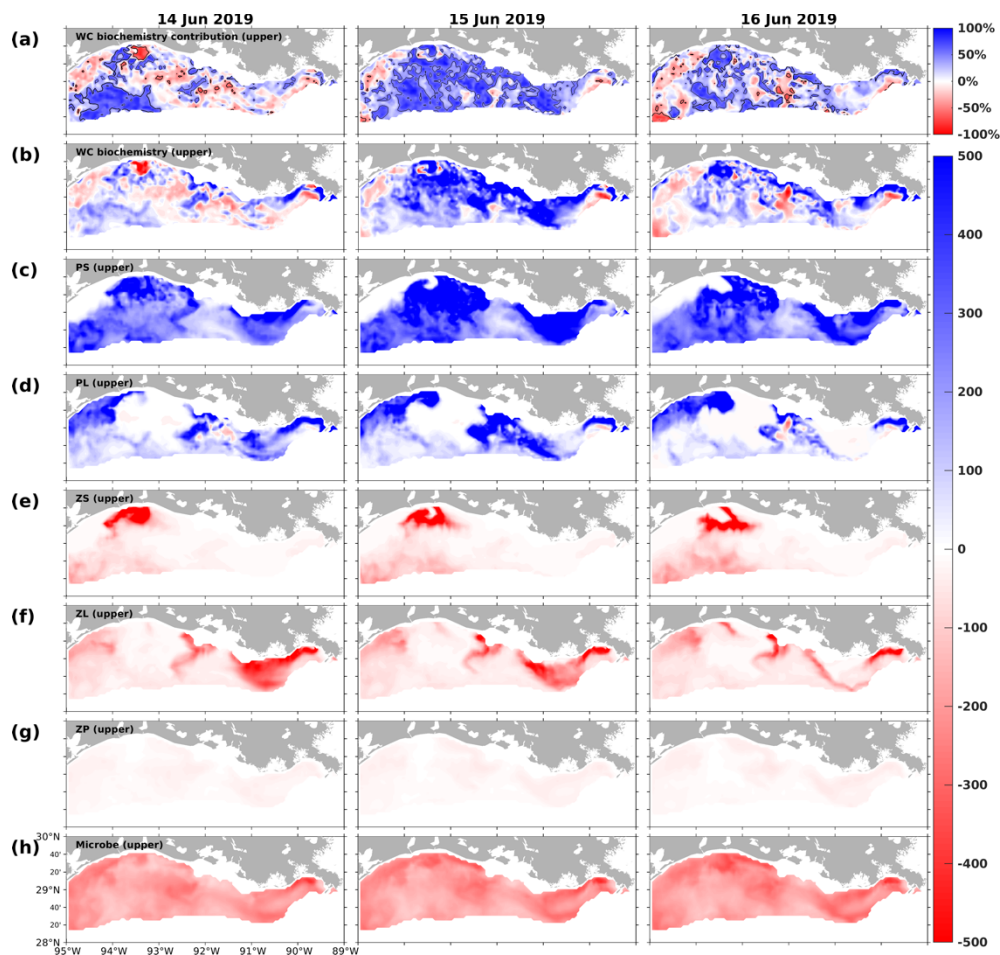
716

717 The influence of SOC and water stratification on bottom hypoxia in the LaTex shelf has been well-documented. Yet, the role  
718 of planktonic community complexity has received scant attention in prior numerical and observational studies. This study  
719 devoted considerable effort to validating various factors, from nutrient dynamics (concentration and limitation types) to  
720 phytoplankton composition (diatom ratio and temporal variations in total primary production) and oxygen variables (SOC, DO  
721 profiles, and hypoxia patterns). Our findings illustrated how both bottom-up mechanisms (phytoplankton competition for  
722 nutrients) and top-down effects (zooplankton grazing on phytoplankton) shape plankton composition, thereby influencing DO  
723 levels in the upper water column and affecting subsequent changes in bottom DO and hypoxia patterns through physical  
724 transports (e.g., vertical diffusion). The insights obtained suggest that the impacts of planktonic community complexity on  
725 bottom DO and hypoxia patterns could be of high importance.

726

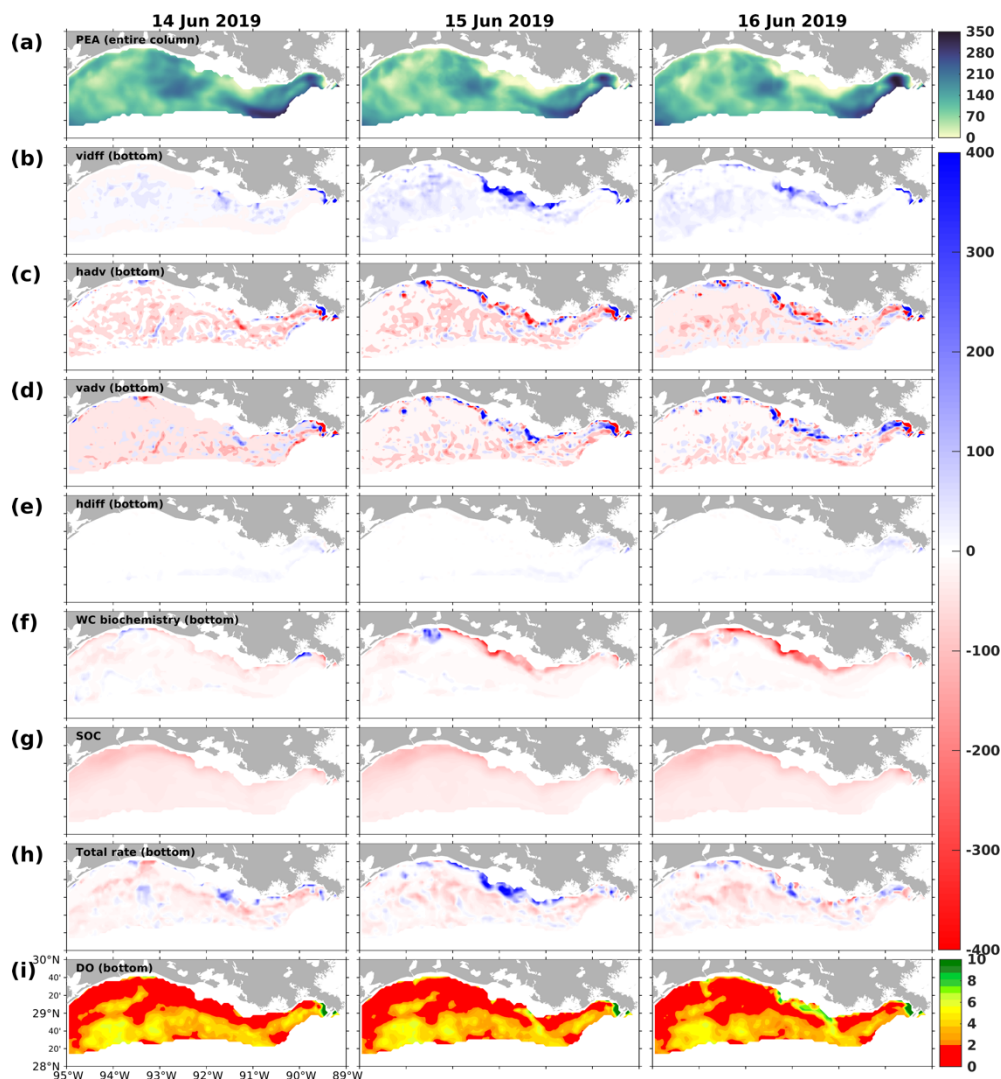
727 Nonetheless, incorporating a more complex plankton community in the model requires reasonable parameterizations for  
728 different groups to represent their interactions. The large number of parameters can sometimes hamper the reliability of a  
729 biogeochemical model due to the lack of support from in-situ observations or laboratory experiments. This is also a critical  
730 reason why prevailing lower-trophic biogeochemical models are often “over-simplified”. Even in complex models, the number  
731 of plankton functional groups considered needs to be constrained to avoid over-parameterization. For example, there are two  
732 phytoplankton and two zooplankton functional groups in PISCES (Aumont and Bopp, 2006) and CoSiNE models (Chai et al.,

733 2002), three phytoplankton and two zooplankton functional groups in PlankTOM5 model (Buitenhuis et al., 2010), and three  
 734 phytoplankton and one zooplankton functional groups in CCSM-BEC model (Moore et al., 2004).  
 735



736  
 737 **Figure 16.** Snapshots of DO contribution by the (a) water column biochemical processes (percentages) in the upper layers, DO  
 738 gain/loss rates ( $\text{mmol m}^{-2} \text{day}^{-1}$ ) due to (b) water column biochemical processes, (c) PS, (d) PL, (e) ZS, (f) ZL, (g) ZP, and (h) microbe  
 739 in the upper layers. The percentage contribution is related to the sum of absolute DO changes due to water column biochemical  
 740 processes, water transports (advectons and diffusions), and air-sea fluxes in the upper layers. The solid black lines in (a) indicate  
 741 the -50% and 50% contour lines.





742

743 **Figure 17. Snapshots of (a) potential energy anomaly (PEA;  $\text{J m}^{-3}$ ), DO gain/loss rates ( $\text{mmol m}^{-2} \text{day}^{-1}$ ) due to (b) vertical diffusion**  
 744 **(vdiff), (c) horizontal advection (hadv), (d) vertical advection (vadv), (e) horizontal diffusion (hdiff), (f) water column biochemical**  
 745 **processes in the bottom layers, and (g) SOC, (h) total bottom DO gain/loss rates ( $\text{mmol m}^{-2} \text{day}^{-1}$ ), and (i) bottom DO concentration**  
 746 **( $\text{mg L}^{-1}$ ). Rate snapshots are daily averages, while snapshots of state variables (i.e., PEA and bottom DO concentration) are extracted**  
 747 **at UTC 00:00 on each sampled day.**

## 748 5 Conclusions

749 In this study, we modified a three-dimensional coupled hydrodynamic–biogeochemical model (NEMURO) and adapted it to  
 750 the GoM to investigate the mechanisms of bottom DO variability in the LaTex Shelf from 2007 to 2020. In addition to N and  
 751 Si, a P flow was embedded into the NEMURO model to account for the impacts of P limitation on phytoplankton growth rates.  
 752 Drawing upon the SOC scheme of the instantaneous remineralization developed by Fennel et al. (2006), a pool of sedimentary  
 753 PON was added to capture temporal delays in SOC relative to the peak of plankton blooms. The model well reproduced the



754 surface inorganic nutrient concentration (i.e., nitrate, phosphate, and silicate), nutrient limitation patterns, the ratio of diatom  
755 to total phytoplankton, and the magnitude of SOC. The model's robustness in DO simulation was affirmed via comparison of  
756 the DO profiles against cruise observations from two different databases, comparison of spatial distributions of bottom DO,  
757 and time series of the hypoxic area against the shelf-wide cruise observations.

758

759 Model results revealed that the changing dominated current system in summer can significantly alter the distribution of shelf  
760 nutrients and types of nutrient limitations. While N and P limitation dominate the Mississippi and Atchafalaya River plume  
761 area, Si limitation becomes pronounced as the coastal current system shifts from westward to eastward or northward,  
762 facilitating the intrusion of low-Si waters from the west and the deep gulf. This effect, particularly evident on the western shelf,  
763 has rarely been addressed in previous studies on nutrient limitation. Model results also indicated that under a westward  
764 background current system, upwellings can enhance nearshore surface nutrient content, with the two modeled phytoplankton  
765 functional groups, PS and PL, exhibiting distinct responses to the redistribution of surface nutrients.

766

767 Our findings underscore the importance of incorporating complex community dynamics and sophisticated nonlinear  
768 interactions into biogeochemical models to capture the variability in primary production on the LaTex Shelf. The model  
769 identified a bi-peak production pattern in spring and early summer, aligning with satellite-derived chlorophyll *a* variations – a  
770 pattern not commonly reported in earlier research. We linked this bi-peak pattern to plankton community interactions,  
771 including both bottom-up and top-down effects, as demonstrated in the sampled spring and summer snapshots. Changes in  
772 nutrient distribution arising from interactions between the LaTex shelf and its adjacent waters, the passages of LCE, the  
773 formation of upwelling or downwelling systems, and variations in river plume patterns are crucial in influencing plankton  
774 interactions, highlighting the important role of open ocean dynamics and boundary conditions along the LaTex shelf in LaTex  
775 biogeochemical modeling.

776

777 While the effects of SOC and water stratification on bottom hypoxia are well-recognized, our study illuminates how plankton  
778 composition, influenced by bottom-up and top-down effects, can affect DO levels in the upper water column and lead to  
779 changes in bottom DO and hypoxia patterns through physical transport processes, such as vertical diffusion. These insights  
780 suggest the potential impacts of planktonic community complexity on bottom DO and hypoxia patterns, emphasizing the need  
781 for future *in situ* and modeling efforts.

782

783 **Code/Data availability:** Model data is available at the LSU mass storage system and details are on the webpage of the  
784 Coupled Ocean Modeling Group at LSU (<https://faculty.lsu.edu/zxue/>). Data requests can be sent to the corresponding  
785 author via this webpage.

786

787 **Author contribution:** Z. George Xue designed the experiments and Yanda Ou carried them out. Yanda Ou developed the  
788 model code and performed the simulations. Yanda Ou and Z. George Xue prepared the manuscript.

789  
790 **Competing interests:** The authors declare that they have no conflict of interest.

791  
792 **Acknowledgment:** Research support was provided through the Bureau of Ocean Energy Management (M17AC00019,  
793 M20AC10001). We thank Dr. Jerome Fiechter at UC Santa Cruz for sharing his NEMURO model codes and Dr. Katja Fennel  
794 at Dalhousie University for discussing model parameterization. The computational resource was provided by the High-  
795 Performance Computing Facility (clusters SuperMIC and QueenBee3) at Louisiana State University.

796  
797

798 **Appendix A: Expressions of processes terms modified in this study**

799 Detailed descriptions of related terms and parameters are listed in Appendix B.

800 **A1 Update gross primary production of PS and PL due to the additional phosphate limitation**

801  $GppPSn = GppNPS + GppAPS,$  (A1)

802  $GppPLn = GppNPL + GppAPL,$  (A2)

803 where,

804  $GppNPS = PSn V_{maxS} \exp(K_{GppS} TMP) \left[1 - \exp\left(-\frac{\alpha_{PS}}{V_{maxS}} I_{PS}\right)\right] \exp\left(-\frac{\beta_{PS}}{V_{maxS}} I_{PS}\right) NutlimPS RnewS,$  (A3)

805  $GppAPS = PSn V_{maxS} \exp(K_{GppS} TMP) \left[1 - \exp\left(-\frac{\alpha_{PS}}{V_{maxS}} I_{PS}\right)\right] \exp\left(-\frac{\beta_{PS}}{V_{maxS}} I_{PS}\right) NutlimPS (1 - RnewS),$  (A4)

806  $GppNPL = PLn V_{maxL} \exp(K_{GppL} TMP) \left[1 - \exp\left(-\frac{\alpha_{PL}}{V_{maxL}} I_{PL}\right)\right] \exp\left(-\frac{\beta_{PL}}{V_{maxL}} I_{PL}\right) NutlimPL RnewL,$  (A5)

807  $GppAPL = PLn V_{maxL} \exp(K_{GppL} TMP) \left[1 - \exp\left(-\frac{\alpha_{PL}}{V_{maxL}} I_{PL}\right)\right] \exp\left(-\frac{\beta_{PL}}{V_{maxL}} I_{PL}\right) NutlimPL (1 - RnewL),$  (A6)

808

809  $RnewS = \frac{NO_3}{(NO_3 + K_{NO_3S}) \left(1 + \frac{NH_4}{K_{NH_4S}}\right)} \frac{1}{\frac{NO_3}{(NO_3 + K_{NO_3S}) \left(1 + \frac{NH_4}{K_{NH_4S}}\right)} + \frac{NH_4}{NH_4 + K_{NH_4S}}},$  (A7)

810  $RnewL = \frac{NO_3}{(NO_3 + K_{NO_3L}) \left(1 + \frac{NH_4}{K_{NH_4L}}\right)} \frac{1}{\frac{NO_3}{(NO_3 + K_{NO_3L}) \left(1 + \frac{NH_4}{K_{NH_4L}}\right)} + \frac{NH_4}{NH_4 + K_{NH_4L}}},$  (A8)

811  $NutlimPS = \min\left(\frac{NO_3}{(NO_3 + K_{NO_3S}) \left(1 + \frac{NH_4}{K_{NH_4S}}\right)} + \frac{NH_4}{NH_4 + K_{NH_4S}}, \frac{PO_4}{PO_4 + K_{PO_4S}}\right),$  (A9)

812  $NutlimPL = \min\left(\frac{NO_3}{(NO_3 + K_{NO_3L}) \left(1 + \frac{NH_4}{K_{NH_4L}}\right)} + \frac{NH_4}{NH_4 + K_{NH_4L}}, \frac{PO_4}{PO_4 + K_{PO_4L}}, \frac{SiOH_4}{SiOH_4 + K_{SiOH_4L}}\right),$  (A10)

813  $I_{PS} = PAR \text{ frac} \exp\left\{z \text{ AttSW} + \text{AttPS} \int_z^0 [PSn(\zeta) + PLn(\zeta)] d\zeta\right\},$  (A11)

814  $I_{PL} = PAR \text{ frac} \exp\left\{z \text{ AttSW} + \text{AttPL} \int_z^0 [PSn(\zeta) + PLn(\zeta)] d\zeta\right\},$  (A12)

815 **A2 Update aerobic decomposition from PON to NH<sub>4</sub> and from DON to NH<sub>4</sub> due to the introduction of oxygen dependency**  
816

817  $DecP2N = PON VP2N_0 \exp(K_{P2N} TMP) \hat{r},$  (A13)

818  $DecD2N = PON VD2N_0 \exp(K_{D2N} TMP) \hat{r},$  (A14)

819 where,

820  $\hat{r} = \max\left[\frac{\max(0, Oxyg - Oxyg_{th})}{K_{Oxyg} + Oxyg - Oxyg_{th}}, 0\right],$  (A15)

821 **A3 Update water column nitrification due to the introduction of oxygen dependency and light limitation**

822  $Nit = Nit_0 \exp(K_{Nit} TMP) LgtlimN \hat{r}$ , (A16)

823 where,

824  $LgtlimN = 1 - \max\left(0, \frac{I_N - I_0}{I_N - I_0 + k_I}\right)$ , (A17)

825  $I_N = PAR \text{ frac} \exp\left\{z \text{ AttSW} + \max(\text{AttPS}, \text{AttPL}) \int_z^0 [PSn(\zeta) + PLn(\zeta)] d\zeta\right\}$ , (A18)

826 **A4 Additional SOC term:**

827  $SOC = 8.3865 PON_{sed} VP2N_0 \exp(K_{P2N} TMP)$ , (A19)

828 **Appendix B: Descriptions of terms and parameters**

829 **Table B1. Descriptions of state variables**

Terms	Description	Unit
$NH_4$	Ammonium concentration	mmolN m <sup>-3</sup>
$NO_3$	Nitrate concentration	mmolN m <sup>-3</sup>
$PO_4$	Phosphate concentration	mmolP m <sup>-3</sup>
$DOP$	Dissolved organic phosphorus concentration	mmolP m <sup>-3</sup>
$POP$	Particulate organic phosphorus concentration	mmolP m <sup>-3</sup>
$SiOH_4$	Silicate concentration	mmolSi m <sup>-3</sup>
$PSn$	Small phytoplankton biomass concentration measured in nitrogen	mmolN m <sup>-3</sup>
$PLn$	Large phytoplankton biomass concentration measured in nitrogen	mmolN m <sup>-3</sup>
$Oxyg$	Dissolved oxygen concentration	mmolO <sub>2</sub> m <sup>-3</sup>

830

831 **Table B2 Descriptions of related terms involved in the phosphorus cycle and nutrient limitation. Superscripts “\*” and “+” denote**  
832 **that the mathematic expressions of corresponding terms are the same as those in Kishi et al. (2007) and Shropshire et al. (2020),**  
833 **respectively. Expressions of terms with no superscript are updated and reported in Appendix A.**

Terms	Description	Unit
$DecP2N$	Decomposition rate from PON to NH <sub>4</sub>	mmolN m <sup>-3</sup> day <sup>-1</sup>
$DecD2N$	Decomposition rate from DON to NH <sub>4</sub>	mmolN m <sup>-3</sup> day <sup>-1</sup>
$DecP2D^{*+}$	Decomposition rate from PON to DON	mmolN m <sup>-3</sup> day <sup>-1</sup>
$EgeZLn^+$	Large zooplankton egestion rate measured in nitrogen	mmolN m <sup>-3</sup> day <sup>-1</sup>
$EgeZPn^{*+}$	Predatory zooplankton egestion rate measured in nitrogen	mmolN m <sup>-3</sup> day <sup>-1</sup>

<i>EgeZSn</i> <sup>*+</sup>	Small zooplankton egestion rate measured in nitrogen	mmolN m <sup>-3</sup> day <sup>-1</sup>
<i>ExcPSn</i> <sup>*+</sup>	Small phytoplankton extracellular excretion rate to DON and is measured in nitrogen	mmolN m <sup>-3</sup> day <sup>-1</sup>
<i>ExcPLn</i> <sup>*+</sup>	Large phytoplankton extracellular excretion rate to DON and is measured in nitrogen	mmolN m <sup>-3</sup> day <sup>-1</sup>
<i>ExcZSn</i> <sup>*+</sup>	Small zooplankton excretion rate to NH <sub>4</sub> and is measured in nitrogen	mmolN m <sup>-3</sup> day <sup>-1</sup>
<i>ExcZLn</i> <sup>+</sup>	Large zooplankton excretion rate to NH <sub>4</sub> and is measured in nitrogen	mmolN m <sup>-3</sup> day <sup>-1</sup>
<i>ExcZPn</i> <sup>*+</sup>	Predatory zooplankton excretion rate to NH <sub>4</sub> and is measured in nitrogen	mmolN m <sup>-3</sup> day <sup>-1</sup>
<i>GppNPS</i>	Small phytoplankton nitrate-induced gross primary production rate measured in nitrogen	mmolN m <sup>-3</sup> day <sup>-1</sup>
<i>GppAPS</i>	Small phytoplankton ammonium-induced gross primary production rate measured in nitrogen	mmolN m <sup>-3</sup> day <sup>-1</sup>
<i>GppPSn</i>	Small phytoplankton gross primary production rate measured in nitrogen	mmolN m <sup>-3</sup> day <sup>-1</sup>
<i>GppNPL</i>	Large phytoplankton nitrate-induced gross primary production rate measured in nitrogen	mmolN m <sup>-3</sup> day <sup>-1</sup>
<i>GppAPL</i>	Large phytoplankton ammonium-induced gross primary production rate measured in nitrogen	mmolN m <sup>-3</sup> day <sup>-1</sup>
<i>GppPLn</i>	Large phytoplankton gross primary production rate measured in nitrogen	mmolN m <sup>-3</sup> day <sup>-1</sup>
<i>MorPSn</i> <sup>+</sup>	Small phytoplankton mortality rate measured in nitrogen	mmolN m <sup>-3</sup> day <sup>-1</sup>
<i>MorPLn</i> <sup>+</sup>	Large phytoplankton mortality rate measured in nitrogen	mmolN m <sup>-3</sup> day <sup>-1</sup>
<i>MorZSn</i> <sup>+</sup>	Small zooplankton mortality rate measured in nitrogen	mmolN m <sup>-3</sup> day <sup>-1</sup>
<i>MorZLn</i> <sup>+</sup>	Large zooplankton mortality rate measured in nitrogen	mmolN m <sup>-3</sup> day <sup>-1</sup>
<i>MorZPn</i> <sup>*+</sup>	Predatory zooplankton mortality rate measured in nitrogen	mmolN m <sup>-3</sup> day <sup>-1</sup>
<i>Nit</i>	Nitrification rate	mmolN m <sup>-3</sup> day <sup>-1</sup>
<i>ResPSn</i> <sup>*+</sup>	Small phytoplankton respiration rate measured in nitrogen	mmolN m <sup>-3</sup> day <sup>-1</sup>
<i>ResPLn</i> <sup>*+</sup>	Large phytoplankton respiration rate measured in nitrogen	mmolN m <sup>-3</sup> day <sup>-1</sup>
<i>SOC</i>	Sediment oxygen consumption rate	mmolO <sub>2</sub> m <sup>-2</sup> day <sup>-1</sup>

834

835 **Table B3 Descriptions of other variables**

Terms	Description	Unit
$I_{PS}$	Photosynthetically available radiation for small phytoplankton	$W m^{-2}$
$I_{PL}$	Photosynthetically available radiation for large phytoplankton	$W m^{-2}$
$I_N$	Maximum photosynthetically available radiation	$W m^{-2}$
$LgtlimN$	Light inhibition on nitrification rate	no dimension
$NutlimPS$	Nutrient limitation term for small phytoplankton	no dimension
$NutlimPL$	Nutrient limitation term for large phytoplankton	no dimension
$PAR$	Net short-wave radiation on water surface	$W m^{-2}$
$\hat{f}$	Oxygen inhibition on nitrification and aerobic decomposition rates	no dimension
$RnewS$	The f-ratio of small phytoplankton which is defined by the ratio of nitrate uptake to total uptake of nitrate and ammonium	no dimension
$RnewL$	The f-ratio of large phytoplankton which is defined by the ratio of nitrate uptake to total uptake of nitrate and ammonium	no dimension
$Thickness_{bot}$	Thickness of the bottom water layer	m
$TMP$	Water temperature	$^{\circ}C$
$z, \zeta$	Vertical coordinate which is negative below sea surface	m

836

837 **Table B4. Descriptions and values of all model parameters. Superscripts “S”, “L”, “F06”, and “F13” denote that the corresponding**  
838 **parameters follow Shropshire et al. (2020), Laurent et al. (2012), Fennel et al. (2006), and Fennel et al. (2013), respectively.**  
839 **Superscript “\*” indicates the corresponding parameters are from this study.**

Parameter	Description	Units	Values
Small phytoplankton			
$V_{maxS}$	Small phytoplankton maximum photosynthetic rate at 0 $^{\circ}C$	$day^{-1}$	0.4 <sup>S</sup>
$K_{NO_3S}$	Small Phytoplankton half saturation constant for nitrate	$mmolN m^{-3}$	0.5 <sup>S</sup>
$K_{NH_4S}$	Small Phytoplankton half saturation constant for ammonium	$mmolN m^{-3}$	0.1 <sup>S</sup>
$K_{PO_4S}$	Small Phytoplankton half saturation constant for phosphate	$mmolP m^{-3}$	0.03125
$\alpha_{PS}$	Small phytoplankton photochemical reaction coefficient, initial slope of P-I curve	$m^2 W^{-1} day^{-1}$	0.1 <sup>S</sup>

$\beta_{PS}$	Small phytoplankton photoinhibition coefficient	$m^2 W^{-1} day^{-1}$	0.00045 <sup>S</sup>
$Res_{PS0}$	Small phytoplankton respiration rate at 0 °C	$day^{-1}$	0.03 <sup>S</sup>
$Mor_{PS0}$	Small phytoplankton mortality rate at 0 °C	$m^3 mmolN^{-1} day^{-1}$	0.002 <sup>S</sup>
$\gamma_S$	Ratio of extracellular excretion to photosynthesis for small phytoplankton	no dimension	0.135 <sup>S</sup>
$K_{GPPS}$	Small phytoplankton temperature coefficient for photosynthetic rate	$^{\circ}C^{-1}$	0.0693 <sup>S</sup>
$K_{ResPS}$	Small phytoplankton temperature coefficient for respiration	$^{\circ}C^{-1}$	0.0519 <sup>S</sup>
$K_{MorPS}$	Small phytoplankton temperature coefficient for mortality	$^{\circ}C^{-1}$	0.0693 <sup>S</sup>
Large phytoplankton			
$V_{maxL}$	Large phytoplankton maximum photosynthetic rate at 0 °C	$day^{-1}$	0.8 <sup>S</sup>
$K_{NO_3L}$	Large Phytoplankton half saturation constant for nitrate	$mmolN m^{-3}$	3.0 <sup>S</sup>
$K_{NH_4L}$	Large Phytoplankton half saturation constant for ammonium	$mmolN m^{-3}$	0.3 <sup>S</sup>
$K_{PO_4L}$	Large Phytoplankton half saturation constant for phosphate	$mmolP m^{-3}$	0.1875
$K_{SiOH_4L}$	Large Phytoplankton half saturation constant for silicate	$mmolSi m^{-3}$	6.0 <sup>S</sup>
$\alpha_{PL}$	Large phytoplankton photochemical reaction coefficient, initial slope of P-I curve	$m^2 W^{-1} day^{-1}$	0.1 <sup>S</sup>
$\beta_{PL}$	Large phytoplankton photoinhibition coefficient	$m^2 W^{-1} day^{-1}$	0.00045 <sup>S</sup>
$Res_{PL0}$	Large phytoplankton respiration rate at 0 °C	$day^{-1}$	0.03 <sup>S</sup>
$Mor_{PL0}$	Large phytoplankton mortality rate at 0 °C	$m^3 mmolN^{-1} day^{-1}$	0.001 <sup>S</sup>

$\gamma_L$	Ratio of extracellular excretion to photosynthesis for large phytoplankton	no dimension	0.135 <sup>S</sup>
$K_{GppL}$	Large phytoplankton temperature coefficient for photosynthetic rate	$^{\circ}\text{C}^{-1}$	0.0693 <sup>S</sup>
$K_{MorPL}$	Large phytoplankton temperature coefficient for mortality	$^{\circ}\text{C}^{-1}$	0.0693 <sup>S</sup>
$K_{ResPL}$	Large phytoplankton temperature coefficient for respiration	$^{\circ}\text{C}^{-1}$	0.0693 <sup>S</sup>
Small zooplankton			
$GR_{maxSps}$	Small zooplankton maximum grazing rate on small phytoplankton at 0 $^{\circ}\text{C}$	$\text{day}^{-1}$	0.6 <sup>S</sup>
$\lambda_S$	Ivlev constant of small zooplankton	$\text{m}^3 \text{mmolN}^{-1}$	1.4 <sup>S</sup>
$PS2ZS$	Small zooplankton threshold value for grazing on small phytoplankton	$\text{mmolN m}^{-3}$	0.043 <sup>S</sup>
$\alpha_{ZS}$	Assimilation efficiency of small zooplankton	no dimension	0.7 <sup>S</sup>
$\beta_{ZS}$	Growth efficiency of small zooplankton	no dimension	0.3 <sup>S</sup>
$Mor_{ZS0}$	Small zooplankton mortality rate at 0 $^{\circ}\text{C}$	$\text{m}^3 \text{mmolN}^{-1} \text{day}^{-1}$	0.022 <sup>S</sup>
$K_{Gras}$	Small zooplankton temperature coefficient for grazing	$^{\circ}\text{C}^{-1}$	0.0693 <sup>S</sup>
$K_{MorZS}$	Small zooplankton temperature coefficient for mortality	$^{\circ}\text{C}^{-1}$	0.0693 <sup>S</sup>
Large zooplankton			
$GR_{maxLps}$	Large zooplankton maximum grazing rate on small phytoplankton at 0 $^{\circ}\text{C}$	$\text{day}^{-1}$	0 <sup>S</sup>
$GR_{maxLpl}$	Large zooplankton maximum grazing rate on large phytoplankton at 0 $^{\circ}\text{C}$	$\text{day}^{-1}$	0.3 <sup>S</sup>
$GR_{maxLzs}$	Large zooplankton maximum grazing rate on small zooplankton at 0 $^{\circ}\text{C}$	$\text{day}^{-1}$	0.3 <sup>S</sup>
$\lambda_L$	Ivlev constant of large zooplankton	$\text{m}^3 \text{mmolN}^{-1}$	1.4 <sup>S</sup>
$PL2ZL$	Large zooplankton threshold value for grazing on large phytoplankton	$\text{mmolN m}^{-3}$	0.040 <sup>S</sup>

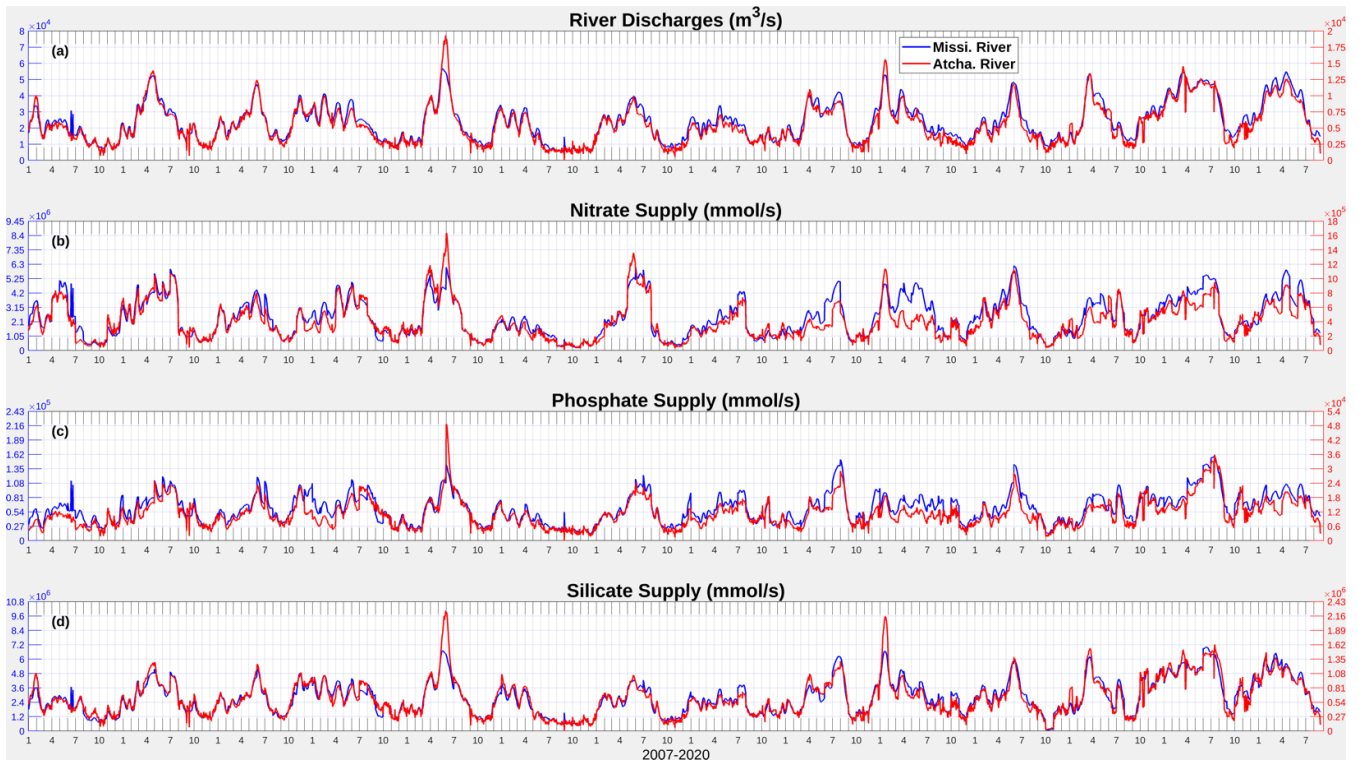


<i>ZS2ZL</i>	Large zooplankton threshold value for grazing on small zooplankton	$\text{mmolN m}^{-3}$	0.040 <sup>S</sup>
$\alpha_{ZL}$	Assimilation efficiency of large zooplankton	no dimension	0.7 <sup>S</sup>
$\beta_{ZL}$	Growth efficiency of large zooplankton	no dimension	0.3 <sup>S</sup>
$Mor_{ZL0}$	Large zooplankton mortality rate at 0 °C	$\text{m}^3 \text{mmolN}^{-1} \text{day}^{-1}$	0.022 <sup>S</sup>
$K_{GraL}$	Large zooplankton temperature coefficient for grazing	$^{\circ}\text{C}^{-1}$	0.0693 <sup>S</sup>
$K_{MorZL}$	Large zooplankton temperature coefficient for mortality	$^{\circ}\text{C}^{-1}$	0.0693 <sup>S</sup>
Predatory zooplankton			
$GR_{maxPpl}$	Predatory zooplankton maximum grazing rate on large phytoplankton at 0 °C	$\text{day}^{-1}$	0.1 <sup>S</sup>
$GR_{maxPzs}$	Predatory zooplankton maximum grazing rate on small zooplankton at 0 °C	$\text{day}^{-1}$	0.1 <sup>S</sup>
$GR_{maxPzl}$	Predatory zooplankton maximum grazing rate on large zooplankton at 0 °C	$\text{day}^{-1}$	0.3 <sup>S</sup>
$\lambda_p$	Ivlev constant of predatory zooplankton	$\text{m}^3 \text{mmolN}^{-1}$	1.4 <sup>S</sup>
<i>PL2ZP</i>	Predatory zooplankton threshold value for grazing on large phytoplankton	$\text{mmolN m}^{-3}$	0.040 <sup>S</sup>
<i>ZS2ZP</i>	Predatory zooplankton threshold value for grazing on small zooplankton	$\text{mmolN m}^{-3}$	0.040 <sup>S</sup>
<i>ZL2ZP</i>	Predatory zooplankton threshold value for grazing on large zooplankton	$\text{mmolN m}^{-3}$	0.040 <sup>S</sup>
$\alpha_{ZP}$	Assimilation efficiency of predatory zooplankton	no dimension	0.7 <sup>S</sup>
$\beta_{ZP}$	Growth efficiency of predatory zooplankton	no dimension	0.3 <sup>S</sup>
$Mor_{ZP0}$	Predatory zooplankton mortality rate at 0 °C	$\text{m}^3 \text{mmolN}^{-1} \text{day}^{-1}$	0.12 <sup>S</sup>
$K_{GraP}$	Predatory zooplankton temperature coefficient for grazing	$^{\circ}\text{C}^{-1}$	0.0693 <sup>S</sup>

$K_{MorZP}$	Predatory zooplankton temperature coefficient for mortality	$^{\circ}\text{C}^{-1}$	0.0693 <sup>S</sup>
$\psi_{PL}$	Grazing inhibition coefficient of predatory zooplankton grazing on large phytoplankton	$\text{m}^3 \text{mmolN}^{-1}$	4.605 <sup>S</sup>
$\psi_{ZS}$	Grazing inhibition coefficient of predatory zooplankton grazing on small zooplankton	$\text{m}^3 \text{mmolN}^{-1}$	3.01 <sup>S</sup>
Light			
$AttSW$	Light attenuation due to seawater	$\text{m}^{-1}$	0.03 <sup>S</sup>
$AttPS$	Light attenuation due to small phytoplankton, self-shading coefficient	$\text{m}^2 \text{mmolN}^{-1}$	0.03 <sup>S</sup>
$AttPL$	Light attenuation due to large phytoplankton, self-shading coefficient	$\text{m}^2 \text{mmolN}^{-1}$	0.03 <sup>S</sup>
$frac$	Fraction of shortwave radiation that is photosynthetically active	no dimension	0.43 <sup>S</sup>
$I_0$	Threshold of light inhibition of nitrification	$\text{W m}^{-2}$	0.0095 <sup>F06</sup>
$k_I$	Light intensity at which light inhibition of nitrification is half-saturated	$\text{W m}^{-2}$	0.1 <sup>F06</sup>
Water column nitrification and aerobic decomposition			
$Nit_0$	Nitrification rate at 0 $^{\circ}\text{C}$	$\text{day}^{-1}$	0.003 <sup>S</sup>
$VP2N_0$	Decomposition rate at 0 $^{\circ}\text{C}$ (PON $\rightarrow$ NH <sub>4</sub> )	$\text{day}^{-1}$	0.01 <sup>S</sup>
$VP2D_0$	Decomposition rate at 0 $^{\circ}\text{C}$ (PON $\rightarrow$ DON)	$\text{day}^{-1}$	0.05 <sup>S</sup>
$VD2N_0$	Decomposition rate at 0 $^{\circ}\text{C}$ (DON $\rightarrow$ NH <sub>4</sub> )	$\text{day}^{-1}$	0.02 <sup>S</sup>
$VO2S_0$	Decomposition rate at 0 $^{\circ}\text{C}$ (Opal $\rightarrow$ Si(OH) <sub>4</sub> )	$\text{day}^{-1}$	0.01 <sup>S</sup>
$K_{Nit}$	Temperature coefficient for nitrification	$^{\circ}\text{C}^{-1}$	0.0693 <sup>S</sup>
$K_{P2D}$	Temperature coefficient for decomposition (PON $\rightarrow$ DON)	$^{\circ}\text{C}^{-1}$	0.0693 <sup>S</sup>
$K_{P2N}$	Temperature coefficient for decomposition (PON $\rightarrow$ NH <sub>4</sub> )	$^{\circ}\text{C}^{-1}$	0.0693 <sup>S</sup>
$K_{D2N}$	Temperature coefficient for decomposition (DON $\rightarrow$ NH <sub>4</sub> )	$^{\circ}\text{C}^{-1}$	0.0693 <sup>S</sup>

$K_{O_2S}$	Temperature coefficient for decomposition (Opal→Si(OH) <sub>4</sub> )	°C <sup>-1</sup>	0.0693 <sup>S</sup>
Other parameters			
$K_{Oxyg}$	Oxygen concentration at which inhibition of nitrification and aerobic respiration are half-saturated	mmolO <sub>2</sub> m <sup>-3</sup>	3.0 <sup>F13</sup>
$Oxyg_{th}$	Oxygen concentration threshold below which no aerobic respiration or nitrification occurs	mmolO <sub>2</sub> m <sup>-3</sup>	6.0 <sup>F13</sup>
$RPO4N$	P: N ratio	mmolP mmolN <sup>-1</sup>	1/16 <sup>L</sup>
$RSiN$	Si: N ratio	mmolSi mmolN <sup>-1</sup>	1 <sup>S</sup>
$rOxNO_3$	Stoichiometric ratios corresponding to the oxygen produced per mol of nitrate assimilated during photosynthesis	mmolO <sub>2</sub> mmolNO <sub>3</sub> <sup>-1</sup>	138/16 <sup>F13</sup>
$rOxNH_4$	Stoichiometric ratios corresponding to the oxygen produced per mol of ammonium assimilated during photosynthesis	mmolO <sub>2</sub> mmolNH <sub>4</sub> <sup>-1</sup>	106/16 <sup>F13</sup>
$setVPON$	Sinking velocity of PON	m day <sup>-1</sup>	-5*
$setVOpal$	Sinking velocity of Opal	m day <sup>-1</sup>	-5*

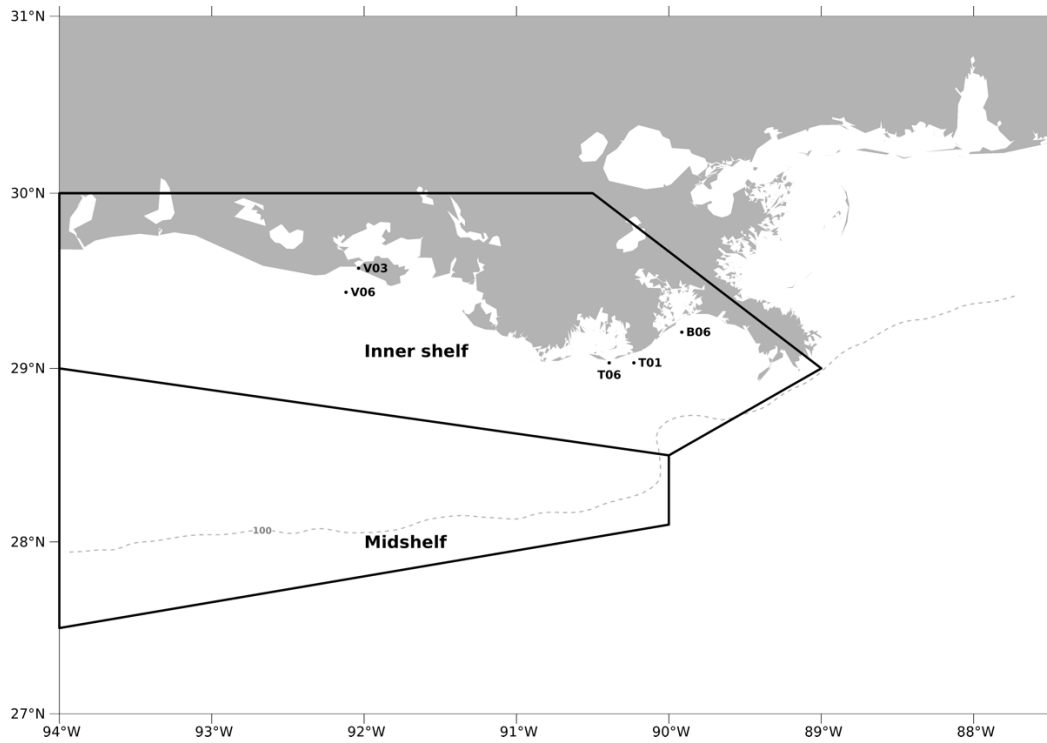
840



842

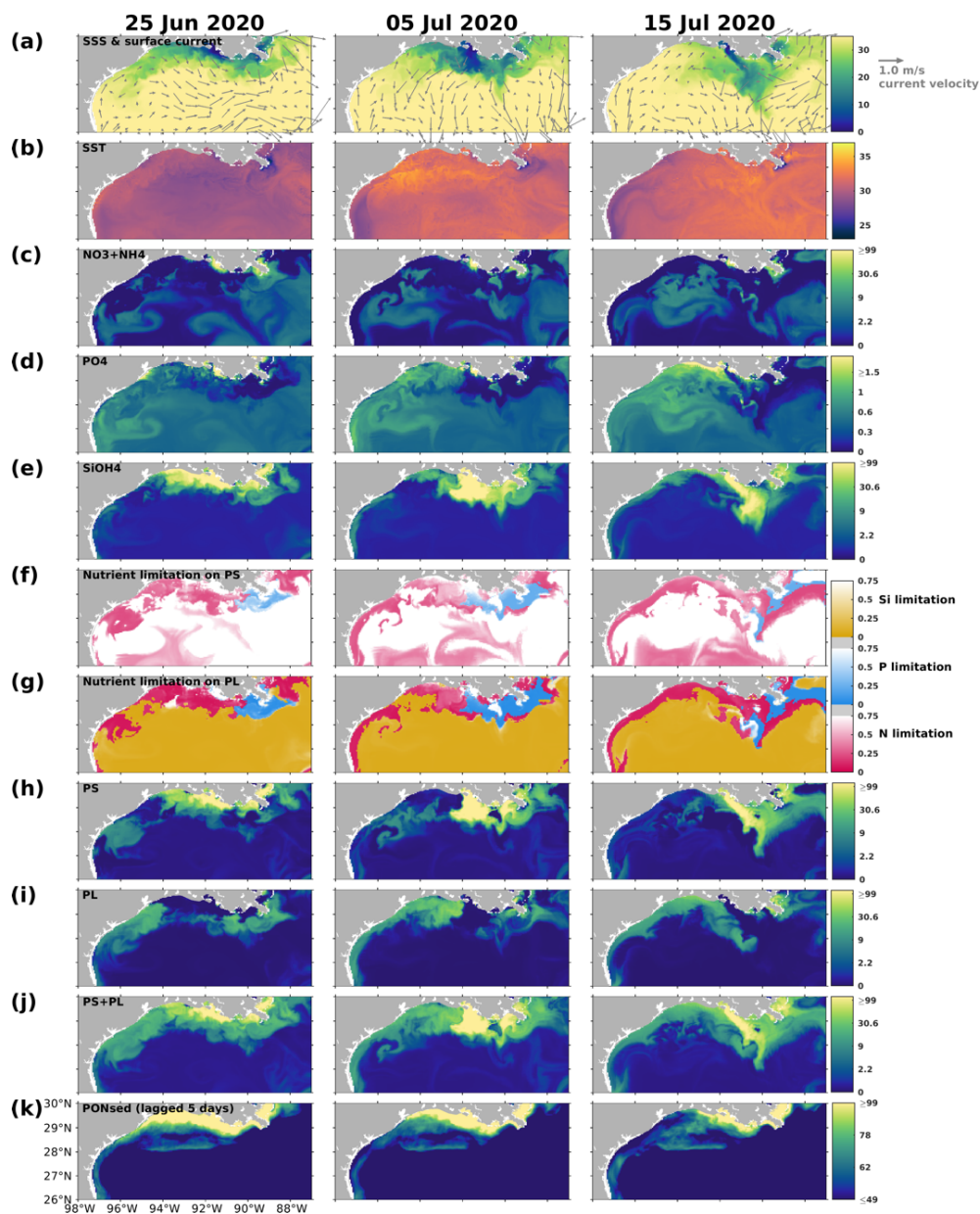
843 **Figure C1. Daily time series (2007–2020) of river discharges of freshwater, nitrate, phosphate, and silicate from the Mississippi and**  
844 **Atchafalaya Rivers.**

845



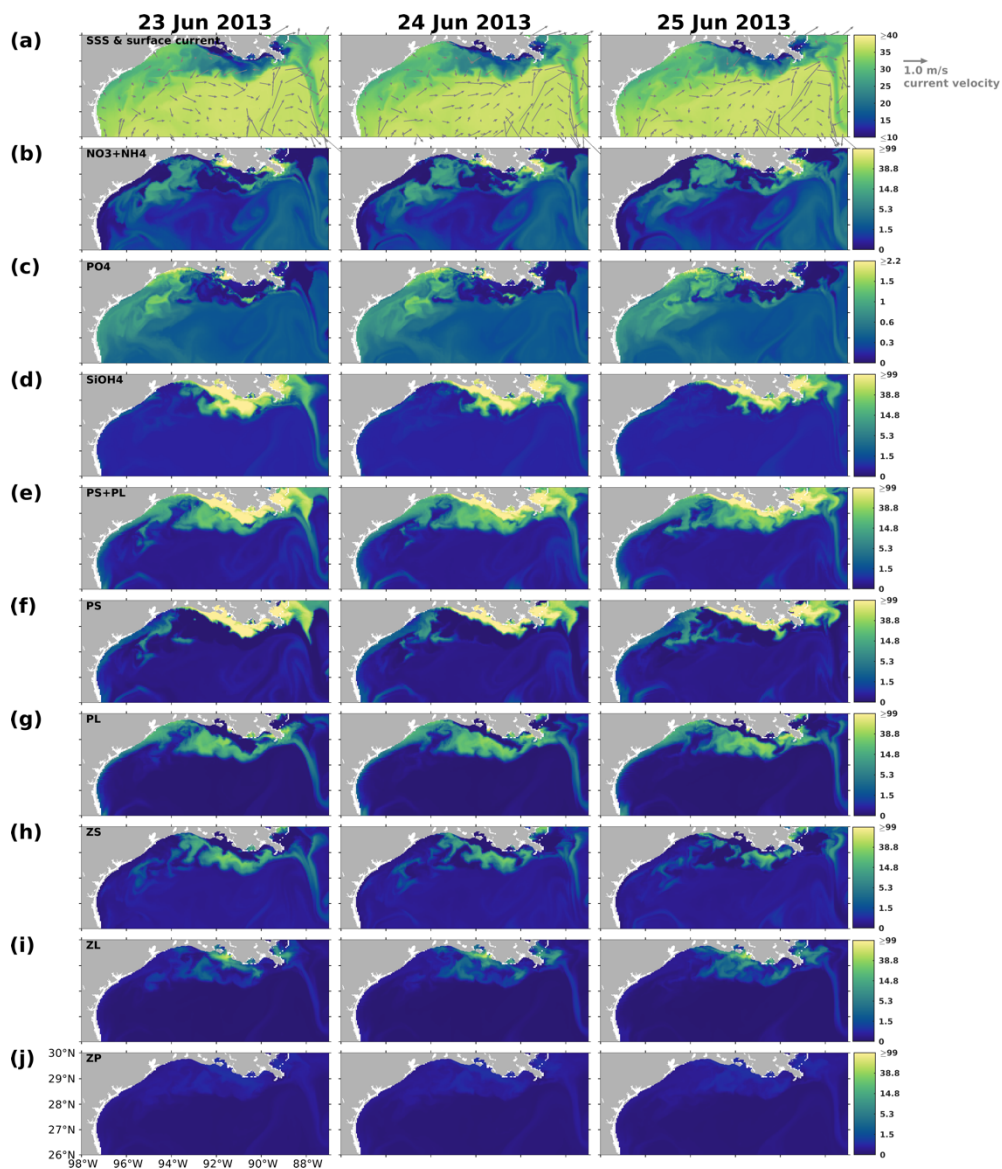
846

847 **Figure C2. The model computational meshes over which the regionally averaged diatom ratios are conducted for validation**  
 848 **purposes. Black dots indicate the sampling locations in Schaeffer et al. (2012), while the regions restricted by two black polygons are**  
 849 **two regions (i.e., inner shelf and mid-shelf) where samples were collected in Chakraborty and Lohrenz's (2015) study.**



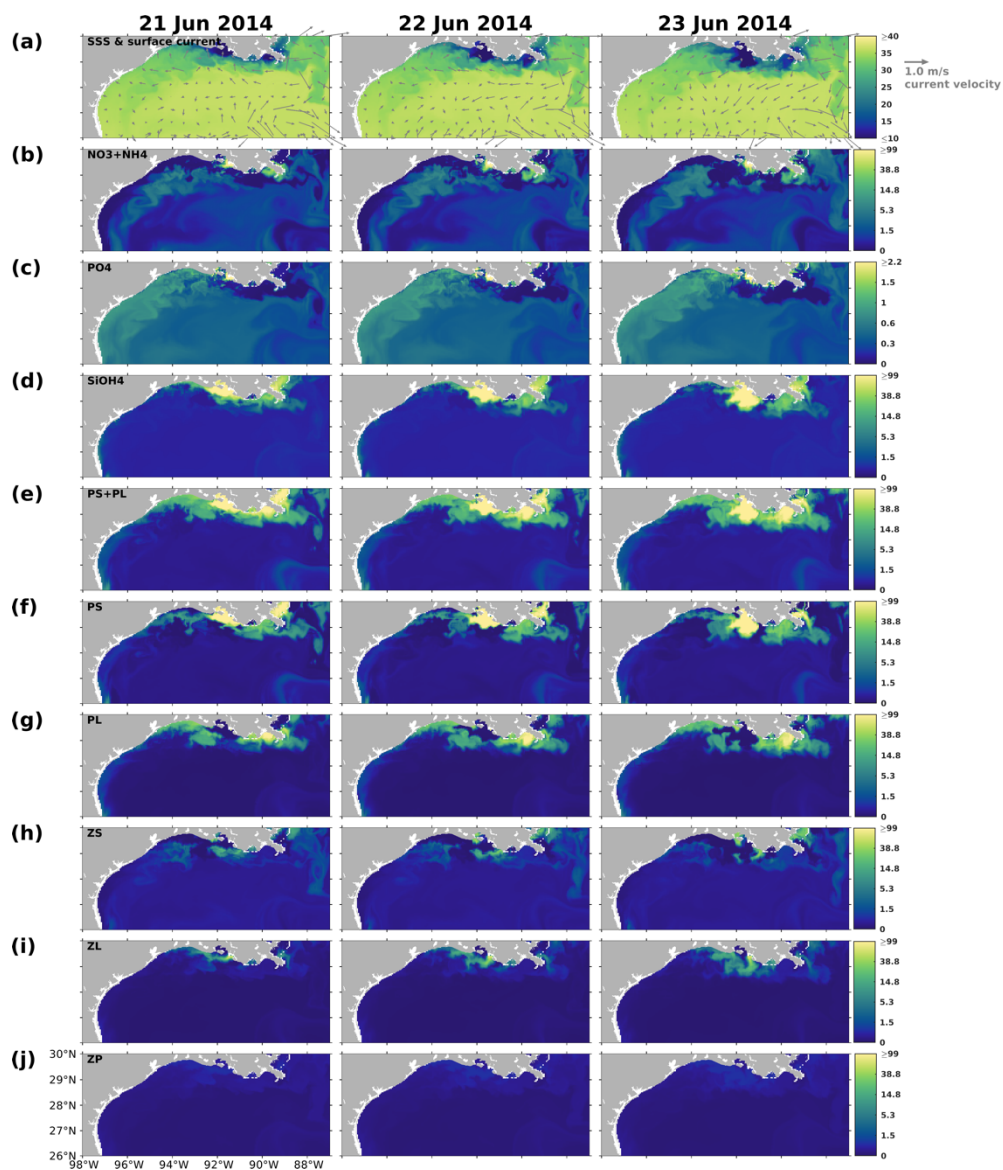
850

851 **Figure C3.** Summer snapshots of (a) sea surface salinity (overlayed with surface current velocity), (b) surface temperature (°C), (c)  
 852 surface total inorganic nitrogen concentration (mmol N m<sup>-3</sup>), (d) surface phosphate concentration (mmol P m<sup>-3</sup>), (e) surface silicate  
 853 concentration (mmol Si m<sup>-3</sup>), (f–g) surface nutrient limitation coefficients, (h–i) surface phytoplankton concentration (mmol N m<sup>-3</sup>),  
 854 and (k) PON<sub>sed</sub> concentration (mmol N m<sup>-3</sup>) with a 5-day lag in the nGoM. The nutrient, phytoplankton, and PON<sub>sed</sub> concentrations  
 855 are displayed in the log<sub>10</sub> scale.



856

857 Figure C4. Snapshots of (a) sea surface salinity (overlaid with surface current velocity),  
 858 surface total inorganic nitrogen concentration ( $\text{mmol N m}^{-3}$ ), (c) surface phosphate concentration ( $\text{mmol P m}^{-3}$ ), (d)–  
 859 surface phytoplankton concentration ( $\text{mmol N m}^{-3}$ ), and (h–j) surface zooplankton concentration ( $\text{mmol N m}^{-3}$ ). The nutrient and  
 860 plankton concentrations are displayed in the log<sub>10</sub> scale.



861  
862 **Figure C5.** Same as Fig. C4, but for snapshots from 21 June 2014 to 23 June 2014.

863

## 864 **References**

- 865 Del Amo, Y. and Brzezinski, M. A.: The chemical form of dissolved Si taken up by marine diatoms, *J. Phycol.*, 35, 1162–1170,  
866 <https://doi.org/10.1046/j.1529-8817.1999.3561162.x>, 1999.
- 867 Anglès, S., Jordi, A., Henrichs, D. W., and Campbell, L.: Influence of coastal upwelling and river discharge on the phytoplankton community  
868 composition in the northwestern Gulf of Mexico, *Prog. Oceanogr.*, 173, 26–36, <https://doi.org/10.1016/j.pocan.2019.02.001>, 2019.



- 869 Aumont, O. and Bopp, L.: Globalizing results from ocean in situ iron fertilization studies, *Global Biogeochem. Cycles*, 20,  
870 <https://doi.org/10.1029/2005GB002591>, 2006.
- 871 Azam, F.: Silicic-acid uptake in diatoms studied with [68Ge]germanic acid as tracer, *Planta*, 121, 205–212,  
872 <https://doi.org/10.1007/BF00389321>, 1974.
- 873 Azam, F., Hemmingsen, B. B., and Volcani, B. E.: Role of silicon in diatom metabolism - V. silicic acid transport and metabolism in the  
874 heterotrophic diatom *Nitzschia alba*, *Arch. Microbiol.*, 97, 103–114, <https://doi.org/10.1007/BF00403050>, 1974.
- 875 Bianchi, T. S., DiMarco, S. F., Cowan, J. H., Hetland, R. D., Chapman, P., Day, J. W., and Allison, M. A.: The science of hypoxia in the  
876 northern Gulf of Mexico: A review, *Sci. Total Environ.*, 408, 1471–1484, <https://doi.org/10.1016/j.scitotenv.2009.11.047>, 2010.
- 877 Billen, G. and Garnier, J.: River basin nutrient delivery to the coastal sea: Assessing its potential to sustain new production of non-siliceous  
878 algae, *Mar. Chem.*, 106, 148–160, <https://doi.org/10.1016/j.marchem.2006.12.017>, 2007.
- 879 Bleck, R.: An oceanic general circulation model framed in hybrid isopycnic-Cartesian coordinates, *Ocean Model.*, 4, 55–88,  
880 [https://doi.org/10.1016/S1463-5003\(01\)00012-9](https://doi.org/10.1016/S1463-5003(01)00012-9), 2002.
- 881 Bleck, R. and Boudra, D. B.: Initial testing of a numerical ocean circulation model using a hybrid (quasi-isopycnic) vertical coordinate, *J.*  
882 *Phys. Oceanogr.*, 11, 755–770, [https://doi.org/https://doi.org/10.1175/1520-0485\(1981\)011<0755:ITOANO>2.0.CO;2](https://doi.org/https://doi.org/10.1175/1520-0485(1981)011<0755:ITOANO>2.0.CO;2), 1981.
- 883 Boyer, T. P., Baranova, O. K., Coleman, C., Garcia, H. E., Grodsky, A., Locarnini, R. A., Mishonov, A. V, Paver, C. R., Reagan, J. R.,  
884 Seidov, D., Smolyar, I. V, Weathers, K. W., and Zweng, M. M.: *World Ocean Database 2018*, Technical., edited by: Mishonov, A. V.,  
885 NOAA Atlas NESDIS 87, 2018.
- 886 Buitenhuis, E. T., Rivkin, R. B., Séailley, S., and Le Quéré, C.: Biogeochemical fluxes through microzooplankton, *Global Biogeochem.*  
887 *Cycles*, 24, <https://doi.org/10.1029/2009GB003601>, 2010.
- 888 Chai, F., Dugdale, R. C., Peng, T., Wilkerson, F. P., and Barber, R. T.: One-dimensional ecosystem model of the equatorial Pacific upwelling  
889 system. Part I: model development and silicon and nitrogen cycle, *Deep Sea Res. Part II Top. Stud. Oceanogr.*, 49, 2713–2745, 2002.
- 890 Chakraborty, S. and Lohrenz, S. E.: Phytoplankton community structure in the river-influenced continental margin of the northern Gulf of  
891 Mexico, *Mar. Ecol. Prog. Ser.*, 521, 31–47, <https://doi.org/10.3354/meps11107>, 2015.
- 892 Chakraborty, S., Lohrenz, S. E., and Gundersen, K.: Photophysiological and light absorption properties of phytoplankton communities in  
893 the river-dominated margin of the northern Gulf of Mexico, *J. Geophys. Res. Ocean.*, 122, 4922–4938,  
894 <https://doi.org/10.1002/2016JC012092>, 2017.
- 895 Chapman, D. C.: Numerical treatment of cross-shelf open boundaries in a barotropic coastal ocean model., [https://doi.org/10.1175/1520-0485\(1985\)015<1060:ntocso>2.0.co;2](https://doi.org/10.1175/1520-0485(1985)015<1060:ntocso>2.0.co;2), 1985.
- 897 Cummings, J. A.: Operational multivariate ocean data assimilation, *Q. J. R. Meteorol. Soc.*, 131, 3583–3604,  
898 <https://doi.org/10.1256/qj.05.105>, 2005.
- 899 Cummings, J. A. and Smedstad, O. M.: Variational Data Assimilation for the Global Ocean, in: *Data Assimilation for Atmospheric, Oceanic*  
900 *and Hydrologic Applications*, vol. II, edited by: Park, S. K. and Xu, L., Springer Berlin Heidelberg, 303–343, [https://doi.org/10.1007/978-3-642-35088-7\\_13](https://doi.org/10.1007/978-3-642-35088-7_13), 2013.
- 902 Dortch, Q. and Whitedge, T. E.: Does nitrogen or silicon limit phytoplankton production in the Mississippi River plume and nearby regions?,  
903 *Cont. Shelf Res.*, 12, 1293–1309, [https://doi.org/10.1016/0278-4343\(92\)90065-R](https://doi.org/10.1016/0278-4343(92)90065-R), 1992.
- 904 Feng, Y., Fennel, K., Jackson, G. A., DiMarco, S. F., and Hetland, R. D.: A model study of the response of hypoxia to upwelling-favorable  
905 wind on the northern Gulf of Mexico shelf, *J. Mar. Syst.*, 131, 63–73, <https://doi.org/10.1016/j.jmarsys.2013.11.009>, 2014.
- 906 Fennel, K. and Laurent, A.: N and P as ultimate and proximate limiting nutrients in the northern Gulf of Mexico: Implications for hypoxia  
907 reduction strategies, 15, 3121–3131, <https://doi.org/10.5194/bg-15-3121-2018>, 2018.

- 908 Fennel, K. and Testa, J. M.: Biogeochemical Controls on Coastal Hypoxia, *Ann. Rev. Mar. Sci.*, 11, 105–130,  
909 <https://doi.org/10.1146/annurev-marine-010318-095138>, 2019.
- 910 Fennel, K., Wilkin, J., Levin, J., Moisan, J., O'Reilly, J., and Haidvogel, D.: Nitrogen cycling in the Middle Atlantic Bight: Results from a  
911 three-dimensional model and implications for the North Atlantic nitrogen budget, *Global Biogeochem. Cycles*, 20, 1–14,  
912 <https://doi.org/10.1029/2005GB002456>, 2006.
- 913 Fennel, K., Hetland, R., Feng, Y., and Dimarco, S.: A coupled physical-biological model of the Northern Gulf of Mexico shelf: Model  
914 description, validation and analysis of phytoplankton variability, 8, 1881–1899, <https://doi.org/10.5194/bg-8-1881-2011>, 2011.
- 915 Fennel, K., Hu, J., Laurent, A., Marta-Almeida, M., and Hetland, R.: Sensitivity of hypoxia predictions for the northern Gulf of Mexico to  
916 sediment oxygen consumption and model nesting, *J. Geophys. Res. Ocean.*, 118, 990–1002, <https://doi.org/10.1002/jgrc.20077>, 2013.
- 917 Fennel, K., Laurent, A., Hetland, R., Justic, D., Ko, D. S., Lehrter, J., Murrell, M., Wang, L., Yu, L., and Zhang, W.: Effects of model physics  
918 on hypoxia simulations for the northern Gulf of Mexico: A model intercomparison, *J. Geophys. Res. Ocean.*, 121, 5731–5750,  
919 <https://doi.org/10.1002/2015JC011516>, 2016.
- 920 Fiechter, J. and Moore, A. M.: Interannual spring bloom variability and Ekman pumping in the coastal Gulf of Alaska, *J. Geophys. Res.*  
921 *Ocean.*, 114, 1–19, <https://doi.org/10.1029/2008JC005140>, 2009.
- 922 Flather, R. A.: A tidal model of the northwest European continental shelf, *Mem. la Soc. R. Sci. Liege*, 10, 141–164, 1976.
- 923 Fox, D. N., Teague, W. J., Barron, C. N., Carnes, M. R., and Lee, C. M.: The Modular Ocean Data Assimilation System (MODAS), *J.*  
924 *Atmos. Ocean. Technol.*, 19, 240–252, [https://doi.org/10.1175/1520-0426\(2002\)019<0240:TMODAS>2.0.CO;2](https://doi.org/10.1175/1520-0426(2002)019<0240:TMODAS>2.0.CO;2), 2002.
- 925 Garcia, H. E., Weathers, K., Paver, C. R., Smolyar, I., Boyer, T. P., Locarnini, R. A., Zweng, M. M., Mishonov, A. V., Baranova, O. K.,  
926 Seidov, D., and Reagan, J. R.: World Ocean Atlas 2018, Volume 3: Dissolved Oxygen, Apparent Oxygen Utilization, and Oxygen Saturation,  
927 Technical., edited by: Mishonov, A. V., NOAA Atlas NESDIS 83, 38 pp., 2018.
- 928 Gomez, F. A., Lee, S. K., Liu, Y., Hernandez, F. J., Muller-Karger, F. E., and Lamkin, J. T.: Seasonal patterns in phytoplankton biomass  
929 across the northern and deep Gulf of Mexico: A numerical model study, 15, 3561–3576, <https://doi.org/10.5194/bg-15-3561-2018>, 2018.
- 930 Große, F., Fennel, K., and Laurent, A.: Quantifying the Relative Importance of Riverine and Open-Ocean Nitrogen Sources for Hypoxia  
931 Formation in the Northern Gulf of Mexico, *J. Geophys. Res. Ocean.*, 5451–5467, <https://doi.org/10.1029/2019jc015230>, 2019.
- 932 Haidvogel, D. B., Arango, H. G., Hedstrom, K., Beckmann, A., Malanotte-Rizzoli, P., and Shchepetkin, A. F.: Model evaluation experiments  
933 in the North Atlantic Basin: Simulations in nonlinear terrain-following coordinates, *Dyn. Atmos. Ocean.*, 32, 239–281,  
934 [https://doi.org/10.1016/S0377-0265\(00\)00049-X](https://doi.org/10.1016/S0377-0265(00)00049-X), 2000.
- 935 Helber, R. W., Townsend, T. L., Barron, C. N., Dastugue, J. M., and Carnes, M. R.: Validation Test Report for the Improved Synthetic  
936 Ocean Profile (ISOP) System, Part I: Synthetic Profile Methods and Algorithm, 2013.
- 937 Hetland, R. D. and DiMarco, S. F.: How does the character of oxygen demand control the structure of hypoxia on the Texas-Louisiana  
938 continental shelf?, *J. Mar. Syst.*, 70, 49–62, <https://doi.org/10.1016/j.jmarsys.2007.03.002>, 2008.
- 939 Justić, D. and Wang, L.: Assessing temporal and spatial variability of hypoxia over the inner Louisiana-upper Texas shelf: Application of  
940 an unstructured-grid three-dimensional coupled hydrodynamic-water quality model, *Cont. Shelf Res.*, 72, 163–179,  
941 <https://doi.org/10.1016/j.csr.2013.08.006>, 2014.
- 942 Justić, D., Rabalais, N. N., and Turner, R. E.: Simulated responses of the Gulf of Mexico hypoxia to variations in climate and anthropogenic  
943 nutrient loading, *J. Mar. Syst.*, 42, 115–126, [https://doi.org/10.1016/S0924-7963\(03\)00070-8](https://doi.org/10.1016/S0924-7963(03)00070-8), 2003.
- 944 Justić, D., Bierman, V. J. J., Scavia, D., and Hetland, R. D.: Forecasting Gulf's Hypoxia: The Next 50 Years?, 30, 791–801, 2007.
- 945 Kishi, M. J., Kashiwai, M., Ware, D. M., Megrey, B. A., Eslinger, D. L., Werner, F. E., Noguchi-Aita, M., Azumaya, T., Fujii, M.,  
946 Hashimoto, S., Huang, D., Iizumi, H., Ishida, Y., Kang, S., Kantakov, G. A., Kim, H. cheol, Komatsu, K., Navrotsky, V. V., Smith, S. L.,  
947 Tadokoro, K., Tsuda, A., Yamamura, O., Yamanaka, Y., Yokouchi, K., Yoshie, N., Zhang, J., Zuenko, Y. I., and Zvalinsky, V. I.: NEMURO-

- 948 a lower trophic level model for the North Pacific marine ecosystem, *Ecol. Modell.*, 202, 12–25,  
949 <https://doi.org/10.1016/j.ecolmodel.2006.08.021>, 2007.
- 950 Kristiansen, S. and Hoell, E. E.: The importance of silicon for marine production, *Hydrobiologia*, 484, 21–31,  
951 <https://doi.org/10.1023/A:1021392618824>, 2002.
- 952 Laurent, A. and Fennel, K.: Simulated reduction of hypoxia in the northern Gulf of Mexico due to phosphorus limitation, *Elem. Sci. Anthr.*,  
953 2, 1–12, <https://doi.org/10.12952/journal.elementa.000022>, 2014.
- 954 Laurent, A., Fennel, K., Hu, J., and Hetland, R.: Simulating the effects of phosphorus limitation in the Mississippi and Atchafalaya river  
955 plumes, 9, 4707–4723, <https://doi.org/10.5194/bg-9-4707-2012>, 2012.
- 956 Laurent, A., Fennel, K., Wilson, R., Lehrter, J., and Devereux, R.: Parameterization of biogeochemical sediment-water fluxes using in situ  
957 measurements and a diagenetic model, 13, 77–94, <https://doi.org/10.5194/bg-13-77-2016>, 2016.
- 958 Laurent, A., Fennel, K., Ko, D. S., and Lehrter, J.: Climate change projected to exacerbate impacts of coastal Eutrophication in the Northern  
959 Gulf of Mexico, *J. Geophys. Res. Ocean.*, 123, 3408–3426, <https://doi.org/10.1002/2017JC013583>, 2018.
- 960 Li, Q. P., Franks, P. J. S., Landry, M. R., Goericke, R., and Taylor, A. G.: Modeling phytoplankton growth rates and chlorophyll to carbon  
961 ratios in California coastal and pelagic ecosystems, *J. Geophys. Res. Biogeosciences*, 115, 1–12, <https://doi.org/10.1029/2009JG001111>,  
962 2010.
- 963 Li, Y., Hu, C., Quigg, A., and Gao, H.: Potential influence of the Deepwater Horizon oil spill on phytoplankton primary productivity in the  
964 northern Gulf of Mexico, *Environ. Res. Lett.*, 14, <https://doi.org/10.1088/1748-9326/ab3735>, 2019.
- 965 Lohrenz, S. E., Fahnenstiel, G. L., Redalje, D. G., Lang, G. A., Dagg, M. J., Whitledge, T. E., and Dortch, Q.: Nutrients, irradiance, and  
966 mixing as factors regulating primary production in coastal waters impacted by the Mississippi River plume, *Cont. Shelf Res.*, 19, 1113–  
967 1141, [https://doi.org/10.1016/S0278-4343\(99\)00012-6](https://doi.org/10.1016/S0278-4343(99)00012-6), 1999.
- 968 Marchesiello, P., McWilliams, J. C., and Shchepetkin, A.: Open boundary conditions for long-term integration of regional oceanic models,  
969 *Ocean Model.*, 3, 1–20, [https://doi.org/10.1016/S1463-5003\(00\)00013-5](https://doi.org/10.1016/S1463-5003(00)00013-5), 2001.
- 970 Mattern, J. P., Fennel, K., and Dowd, M.: Sensitivity and uncertainty analysis of model hypoxia estimates for the Texas-Louisiana shelf, *J.*  
971 *Geophys. Res. Ocean.*, 118, 1316–1332, <https://doi.org/10.1002/jgrc.20130>, 2013.
- 972 McCarthy, M. J., Carini, S. A., Liu, Z., Ostrom, N. E., and Gardner, W. S.: Oxygen consumption in the water column and sediments of the  
973 northern Gulf of Mexico hypoxic zone, *Estuar. Coast. Shelf Sci.*, 123, 46–53, <https://doi.org/10.1016/j.ecss.2013.02.019>, 2013.
- 974 Milligan, A. J., Varela, D. E., Brzezinski, M. A., and Morel, F. M. M.: Dynamics of silicon metabolism and silicon isotopic discrimination  
975 in a marine diatom as a function of pCO<sub>2</sub>, *Limnol. Oceanogr.*, 49, 322–329, <https://doi.org/10.4319/lo.2004.49.2.0322>, 2004.
- 976 Moore, J. K., Doney, S. C., and Lindsay, K.: Upper ocean ecosystem dynamics and iron cycling in a global three-dimensional model, *Global*  
977 *Biogeochem. Cycles*, 18, 1–21, <https://doi.org/10.1029/2004GB002220>, 2004.
- 978 Moriarty, J. M., Harris, C. K., Friedrichs, M. A. M., Fennel, K., and Xu, K.: Impact of Seabed Resuspension on Oxygen and Nitrogen  
979 Dynamics in the Northern Gulf of Mexico: A Numerical Modeling Study, *J. Geophys. Res. Ocean.*, 123, 7237–7263,  
980 <https://doi.org/10.1029/2018JC013950>, 2018.
- 981 Murrell, M. C. and Lehrter, J. C.: Sediment and Lower Water Column Oxygen Consumption in the Seasonally Hypoxic Region of the  
982 Louisiana Continental Shelf, 34, 912–924, <https://doi.org/10.1007/s12237-010-9351-9>, 2011.
- 983 Murrell, M. C., Stanley, R. S., Lehrter, J. C., and Hagy, J. D.: Plankton community respiration, net ecosystem metabolism, and oxygen  
984 dynamics on the Louisiana continental shelf: Implications for hypoxia, *Cont. Shelf Res.*, 52, 27–38,  
985 <https://doi.org/10.1016/j.csr.2012.10.010>, 2013.
- 986 Nelson, D. M. and Dortch, Q.: Silicic acid depletion and silicon limitation in the plume of the Mississippi River: Evidence from kinetic  
987 studies in spring and summer, *Mar. Ecol. Prog. Ser.*, 136, 163–178, <https://doi.org/10.3354/meps136163>, 1996.

- 988 Nelson, D. M., Goering, John J., Kilham, S. S., and Guillard., R. R. L.: Kinetics of silicic acid uptake and rates of silica dissolution in the  
989 marine diatom *Thalassiosira pseudonana*, *J. Phycol.*, 12, 246–252, <https://doi.org/https://doi.org/10.1111/j.1529-8817.1976.tb00510.x>, 1976.
- 990 Olson, R. J.: Differential photoinhibition of marine nitrifying bacteria: a possible mechanism for the formation of the primary nitrite  
991 maximum, *J. Mar. Res.*, 39, 227–238, 1981.
- 992 Parker, R. A.: Dynamic models for ammonium inhibition of nitrate uptake by phytoplankton, *Ecol. Modell.*, 66, 113–120,  
993 [https://doi.org/10.1016/0304-3800\(93\)90042-Q](https://doi.org/10.1016/0304-3800(93)90042-Q), 1993.
- 994 Platt, T., Gallegos, C. L., and Harrison, W. G.: Photoinhibition of photosynthesis in natural assemblages of marine phytoplankton, *J. Mar.*  
995 *Res.*, 38, 687–701, 1980.
- 996 Qian, Y., Jochens, A. E., Kennicutt, M. C., and Biggs, D. C.: Spatial and temporal variability of phytoplankton biomass and community  
997 structure over the continental margin of the northeast Gulf of Mexico based on pigment analysis, *Cont. Shelf Res.*, 23, 1–17,  
998 [https://doi.org/10.1016/S0278-4343\(02\)00173-5](https://doi.org/10.1016/S0278-4343(02)00173-5), 2003.
- 999 Quigg, A., Sylvan, J. B., Gustafson, A. B., Fisher, T. R., Oliver, R. L., Tozzi, S., and Ammerman, J. W.: Going West: Nutrient Limitation  
000 of Primary Production in the Northern Gulf of Mexico and the Importance of the Atchafalaya River, *Aquat. Geochemistry*, 17, 519–544,  
001 <https://doi.org/10.1007/s10498-011-9134-3>, 2011.
- 002 Rabalais, N. N. and Baustian, M. M.: Historical Shifts in Benthic Infaunal Diversity in the Northern Gulf of Mexico since the Appearance  
003 of Seasonally Severe Hypoxia, 12, <https://doi.org/10.3390/d12020049>, 2020.
- 004 Rabalais, N. N. and Turner, R. E.: Gulf of Mexico Hypoxia: Past, Present, and Future, *Limnol. Oceanogr. Bull.*, 28, 117–124,  
005 <https://doi.org/10.1002/lob.10351>, 2019.
- 006 Rabalais, N. N., Turner, R. E., Justic, D., Dortch, Q., and Wiseman, W. J.: Characterization of Hypoxia: Topic 1 Report for the Integrated  
007 Assessment on Hypoxia in the Gulf of Mexico, NOAA Coast. Ocean Progr. Decis. Anal. Ser. No. 15. NOAA Coast. Ocean Program, Silver  
008 Spring, MD. 167, 167 pp., 1999.
- 009 Rabalais, N. N., Turner, R. E., and Wiseman, W. J.: Gulf of Mexico hypoxia, a.k.a. “The dead zone,” *Annu. Rev. Ecol. Syst.*, 33, 235–263,  
010 <https://doi.org/10.1146/annurev.ecolsys.33.010802.150513>, 2002.
- 011 Rabalais, N. N., Turner, R. E., Sen Gupta, B. K., Boesch, D. F., Chapman, P., and Murrell, M. C.: Hypoxia in the northern Gulf of Mexico:  
012 Does the science support the plan to reduce, mitigate, and control hypoxia?, 30, 753–772, <https://doi.org/10.1007/BF02841332>, 2007a.
- 013 Rabalais, N. N., Turner, R. E., Gupta, B. K. S., Platon, E., and Parsons, M. L.: Sediments tell the history of eutrophication and hypoxia in  
014 the northern Gulf of Mexico, *Ecol. Appl.*, 17, 129–143, <https://doi.org/10.1890/06-0644.1>, 2007b.
- 015 Robertson, R. and Hartlipp, P.: Surface wind mixing in the Regional Ocean Modeling System (ROMS), *Geosci. Lett.*, 4,  
016 <https://doi.org/10.1186/s40562-017-0090-7>, 2017.
- 017 Rowe, G. T., Cruz Kaegi, M. E., Morse, J. W., Boland, G. S., and Escobar Briones, E. G.: Sediment community metabolism associated with  
018 continental shelf hypoxia, northern Gulf of Mexico, 25, 1097–1106, <https://doi.org/10.1007/BF02692207>, 2002.
- 019 Royer, T. V.: Stoichiometry of nitrogen, phosphorus, and silica loads in the Mississippi-Atchafalaya River basin reveals spatial and temporal  
020 patterns in risk for cyanobacterial blooms, *Limnol. Oceanogr.*, 65, 325–335, <https://doi.org/10.1002/lno.11300>, 2020.
- 021 Saha, S., Moorthi, S., Pan, H.-L., Wu, X., Wang, J., Nadiga, S., Tripp, P., Kistler, R., Woollen, J., Behringer, D., Liu, H., Stokes, D.,  
022 Grumbine, R., Gayno, G., Wang, J., Hou, Y.-T., Chuang, H.-Y., Juang, H.-M. H., Sela, J., Iredell, M., Treadon, R., Kleist, D., Van Delst,  
023 P., Keyser, D., Derber, J., Ek, M., Meng, J., Wei, H., Yang, R., Lord, S., van den Dool, H., Kumar, A., Wang, W., Long, C., Chelliah, M.,  
024 Xue, Y., Huang, B., Schemm, J.-K., Ebisuzaki, W., Lin, R., Xie, P., Chen, M., Zhou, S., Higgins, W., Zou, C.-Z., Liu, Q., Chen, Y., Han,  
025 Y., Cucurull, L., Reynolds, R. W., Rutledge, G., and Goldberg, M.: NCEP Climate Forecast System Reanalysis (CFSR) 6-hourly Products,  
026 January 1979 to December 2010, <https://doi.org/10.5065/D69K487J>, 2010.
- 027 Saha, S., Moorthi, S., Wu, X., Wang, J., Nadiga, S., Tripp, P., Behringer, D., Hou, Y.-T., Chuang, H., Iredell, M., Ek, M., Meng, J., Yang,  
028 R., Mendez, M. P., van den Dool, H., Zhang, Q., Wang, W., Chen, M., and Becker, E.: NCEP Climate Forecast System Version 2 (CFSv2)

- .029 6-hourly Products, <https://doi.org/10.5065/D61C1TXF>, 2011.
- .030 Schaeffer, B. A., Kurtz, J. C., and Hein, M. K.: Phytoplankton community composition in nearshore coastal waters of Louisiana, *Mar. Pollut.*  
.031 *Bull.*, 64, 1705–1712, <https://doi.org/10.1016/j.marpolbul.2012.03.017>, 2012.
- .032 Seitzinger, S. P. and Giblin, A. E.: Estimating denitrification in North Atlantic continental shelf sediments, in: *Nitrogen Cycling in the North*  
.033 *Atlantic Ocean and its Watersheds*, edited by: Howarth, R. W., Springer Dordrecht, 235–260, [https://doi.org/10.1007/978-94-009-1776-7\\_7](https://doi.org/10.1007/978-94-009-1776-7_7),  
.034 1996.
- .035 Shchepetkin, A. F. and McWilliams, J. C.: The regional oceanic modeling system (ROMS): A split-explicit, free-surface, topography-  
.036 following-coordinate oceanic model, *Ocean Model.*, 9, 347–404, <https://doi.org/10.1016/j.ocemod.2004.08.002>, 2005.
- .037 Shchepetkin, A. F. and McWilliams, J. C.: Correction and commentary for “Ocean forecasting in terrain-following coordinates: Formulation  
.038 and skill assessment of the regional ocean modeling system” by Haidvogel et al., *J. Comp. Phys.* 227, pp. 3595–3624, *J. Comput. Phys.*, 228,  
.039 8985–9000, <https://doi.org/10.1016/j.jcp.2009.09.002>, 2009.
- .040 Shropshire, T., Morey, S., Chassignet, E., Bozec, A., Coles, V., Landry, M., Swaethorp, R., Zapfe, G., and Stukel, M.: Quantifying  
.041 spatiotemporal variability in zooplankton dynamics in the Gulf of Mexico with a physical-biogeochemical model, 17, 3385–3407,  
.042 <https://doi.org/10.5194/bg-17-3385-2020>, 2020.
- .043 Smith, S. M. and Hitchcock, G. L.: Nutrient enrichments and phytoplankton growth in the surface waters of the Louisiana Bight, 17, 740–  
.044 753, <https://doi.org/10.2307/1352744>, 1994.
- .045 Strom, S. L. and Strom, M. W.: Microplankton growth, grazing, and community structure in the northern Gulf of Mexico, *Mar. Ecol. Prog.*  
.046 *Ser.*, 130, 229–240, <https://doi.org/10.3354/meps130229>, 1996.
- .047 Sylvan, J. B., Dortch, Q., Nelson, D. M., Brown, A. F. M., Morrison, W., and Ammerman, J. W.: Phosphorus limits phytoplankton growth  
.048 on the Louisiana shelf during the period of hypoxia formation, *Environ. Sci. Technol.*, 40, 7548–7553, <https://doi.org/10.1021/es061417t>,  
.049 2006.
- .050 Sylvan, J. B., Quigg, A., Tozzi, S., and Ammerman, J. W.: Eutrophication-induced phosphorus limitation in the Mississippi River plume:  
.051 Evidence from fast repetition rate fluorometry, *Limnol. Oceanogr.*, 52, 2679–2685, <https://doi.org/10.4319/lo.2007.52.6.2679>, 2007.
- .052 Testa, J. M. and Michael Kemp, W.: Hypoxia-induced shifts in nitrogen and phosphorus cycling in Chesapeake Bay, *Limnol. Oceanogr.*,  
.053 57, 835–850, <https://doi.org/10.4319/lo.2012.57.3.0835>, 2012.
- .054 Thamatrakoln, K. and Hildebrand, M.: Silicon uptake in diatoms revisited: A model for saturable and nonsaturable uptake kinetics and the  
.055 role of silicon transporters, *Plant Physiol.*, 146, 1397–1407, <https://doi.org/10.1104/pp.107.107094>, 2008.
- .056 Turner, R. and Rabalais, N.: Nitrogen and phosphorus phytoplankton growth limitation in the northern Gulf of Mexico, *Aquat. Microb.*  
.057 *Ecol.*, 68, 159–169, <https://doi.org/10.3354/ame01607>, 2013.
- .058 Wang, L. and Justić, D.: A modeling study of the physical processes affecting the development of seasonal hypoxia over the inner Louisiana-  
.059 Texas shelf: Circulation and stratification, *Cont. Shelf Res.*, 29, 1464–1476, <https://doi.org/10.1016/j.csr.2009.03.014>, 2009.
- .060 Wanninkhof, R.: Relationship Between Wind Speed and Gas Exchange Over the Ocean, *J. Geophys. Res.*, 97, 7373–7382,  
.061 <https://doi.org/10.1029/92JC00188>, 1992.
- .062 Warner, J. C., Geyer, W. R., and Lerczak, J. A.: Numerical modeling of an estuary: A comprehensive skill assessment, *J. Geophys. Res. C*  
.063 *Ocean.*, 110, 1–13, <https://doi.org/10.1029/2004JC002691>, 2005.
- .064 Warner, J. C., Armstrong, B., He, R., and Zambon, J. B.: Development of a Coupled Ocean-Atmosphere-Wave-Sediment Transport  
.065 (COAWST) Modeling System, *Ocean Model.*, 35, 230–244, <https://doi.org/10.1016/j.ocemod.2010.07.010>, 2010.
- .066 Warner, J. C., Defne, Z., Haas, K., and Arango, H. G.: A wetting and drying scheme for ROMS, *Comput. Geosci.*, 58, 54–61,  
.067 <https://doi.org/10.1016/j.cageo.2013.05.004>, 2013.

- .068 Wawrik, B. and Paul, J. H.: Phytoplankton community structure and productivity along the axis of the Mississippi River plume in  
.069 oligotrophic Gulf of Mexico waters, *Aquat. Microb. Ecol.*, 35, 185–196, <https://doi.org/10.3354/ame035185>, 2004.
- .070 Yingling, N., Kelly, T. B., Shropshire, T. A., Landry, M. R., Selph, K. E., Knapp, A. N., Kranz, S. A., Stukel, M. R., and Moisander, P.:  
.071 Taxon-specific phytoplankton growth, nutrient utilization and light limitation in the oligotrophic Gulf of Mexico, *J. Plankton Res.*, 44, 656–  
.072 676, <https://doi.org/10.1093/plankt/fbab028>, 2022.
- .073 Yu, L., Fennel, K., and Laurent, A.: A modeling study of physical controls on hypoxia generation in the northern Gulf of Mexico, *J. Geophys.*  
.074 *Res. Ocean.*, 120, 5019–5039, <https://doi.org/10.1002/2014JC010634>, 2015.
- .075 Zang, Z., Xue, Z. G., Bao, S., Chen, Q., Walker, N. D., Haag, A. S., Ge, Q., and Yao, Z.: Numerical study of sediment dynamics during  
.076 hurricane Gustav, *Ocean Model.*, 126, 29–42, <https://doi.org/10.1016/j.ocemod.2018.04.002>, 2018.
- .077 Zang, Z., Xue, Z. G., Xu, K., Bentley, S. J., Chen, Q., D'Sa, E. J., and Ge, Q.: A Two Decadal (1993–2012) Numerical Assessment of  
.078 Sediment Dynamics in the Northern Gulf of Mexico, 11, 938, <https://doi.org/10.3390/w11050938>, 2019.
- .079 Zang, Z., Xue, Z. G., Xu, K., Ozdemir, C. E., Chen, Q., Bentley, S. J., and Sahin, C.: A Numerical Investigation of Wave-Supported Gravity  
.080 Flow During Cold Fronts Over the Atchafalaya Shelf, *J. Geophys. Res. Ocean.*, 125, 1–24, <https://doi.org/10.1029/2019JC015269>, 2020.
- .081 Zhang, Y., Hu, C., Barnes, B. B., Liu, Y., Kourafalou, V. H., McGillicuddy, D. J., Cannizzaro, J. P., English, D. C., and Lembke, C.: Bio-  
.082 Optical, Physical, and Chemical Properties of a Loop Current Eddy in the Gulf of Mexico, *J. Geophys. Res. Ocean.*, 128,  
.083 <https://doi.org/10.1029/2022JC018726>, 2023.
- .084 Zhao, Y. and Quigg, A.: Nutrient limitation in Northern Gulf of Mexico (NGOM): Phytoplankton communities and photosynthesis respond  
.085 to nutrient pulse, *PLoS One*, 9, <https://doi.org/10.1371/journal.pone.0088732>, 2014.
- .086